Thermoelastic properties of iron- and aluminum-bearing bridgmanite at high pressures and temperatures

A THESIS

SUBMITTED TO THE FACULTY OF THE GRADUATE SCHOOL

OF THE UNIVERSITY OF MINNESOTA

BY

Gaurav Shukla

IN PARTIAL FULFILLMENT OF THE REQUIREMENTS

FOR THE DEGREE OF

Doctor of Philosophy

Renata M. Wentzcovitch

January, 2016

Acknowledgements

I would like to thank my adviser Prof. Renata M. Wentzcovitch for her constant support and guidance during my time in graduate school. I am thankful to Dr. Matteo Cococcioni and Dr. Burak Himmetoglu for teaching me DFT+U methods in first-principles calculations. I would like to thank Dr. Zhongqin Wu, Dr. Han Hsu, and Dr. Mehmet Topsakal for their collaboration. I am thankful to Dr. Andrea Floris for providing me efficient DFPT+U code and Dr. Pedro da Silveira for the help while performing heavy calculations at VLAB cyberinfrastructure.

I am grateful to my preliminary and final oral exam committee members: Prof. Oriol T. Valls, Prof. Allen Goldman, Prof. Robert Gehrz, and Prof. Yong-Zhong Qian for their help and suggestions.

I am also thankful to my colleagues: Dr. Mehmet Topsakal, Dr. Kanchan Sarkar, Dr. Joelson Cott-Garcia, Michel Lacerda Marcondes dos Santos, Juan Valencia-Cardona, and Tian Qin for fruitful discussion on research and various day-to-day topics.

Thank you my friends Saurabh Shirvastava, Susheel Sharma, Prashant Tripathi, Urvashi Singh, Atul Varshney, Aditya Narain Agnihotri, Amin Ahmad Nizami, Kiran Shankar Hazra, Prarit Agarwal, Vaishnavi Rajagopal, Vamshi Mohan Katukuri, Swapnil Tale, Abhijit Wagh, Ramjay Visweswaran, Bhagyashree Katare, Chien-Te Wu, Abdul Naseer Malmi Kakkada, Xiaowei Zhang for your constant support during my stay at U of M. My special thanks to Atul Srivastava and Kriti Srivastava for making me feel

home while away from the home.

I am thankful to my family friend and my first genuine math teacher (during my 10th standard in school), Harbansh Singh alias Guddu Chacha, who taught me how to study and enjoy mathematical subjects. I am very grateful to my school teachers, namely, Director Sir and Guru Ji and my heartfelt thanks to them for kindling the desire to always learn in the life.

I am ever indebted to my family for their constant support and encouragement at every stage of my life. I can never enough thank to my parents for the sacrifices they made for our better future. My brother Shivam deserves a special mention for his inseparable attachment. I am grateful to my wife Shraddha who is ever ready for encouragement and support in my life.

Finally, I would like to thank GOD for his unconditional mercy on a undeserving person like me.

This work was supported primarily by grants NSF/EAR 1319368 and NSF/CAREER 1151738. Computations were performed at the Minnesota Supercomputing Institute (MSI) and at the Blue Waters System at NCSA.

Dedication

To my beloved brother VIKAS who is unfortunately no more to see the light of this day.

Abstract

Thermoelastic properties of the Earth's forming minerals play an important role in deciphering the tomographic images of seismic observations. In spite of the considerable progress in the experimental measurements of the elastic properties of minerals at high pressures and temperatures, the available data is still quite limited to constrain the composition and thermal structure of the Earth's interior. The first-principles atomistic calculations have often complimented the experimental measurements in the study of minerals under high pressure and temperature conditions. In this work, we present the first-principles investigation of the effect of iron (Fe) and aluminum (Al) on the thermoelastic properties of $MgSiO_3$ perovksite (also known as bridgmanite), the most abundant mineral of the Earth's lower mantle. First, we investigate the pressure induced iron state changes in Fe-bearing $MgSiO_3$ and $MgGeO_3$ perovskite (a low-pressure analog of $MgSiO_3$) within the local density (LDA+U) and the generalized gradient approximation augmented by the Hubbard-type correction (GGA+U). We showed that the iron state transitions occur at particular average $\langle$Fe-O$\rangle$ bond-length irrespective of mineral composition ($MgSiO_3$ or $MgGeO_3$) or the exchange and correlation functional used in the calculations (LDA+U or GGA+U). We further study the effect of disorder, iron concentration, and temperature on the spin crossover in Fe^{3+}-bearing bridgmanite using LDA+U calculations. Thermal effects have been addressed within the quasiharmonic approximation using density functional perturbation theory (DFPT). Then, we calculate the aggregate elastic moduli (bulk and shear modulus) and acoustic velocities for the Fe- and Al-bearing bridgmanite to investigate the effect of iron state changes and its possible consequences to the lower mantle composition.

Contents

List of Tables

List of Figures

Chapter 1

Introduction

The primary source of information about the Earth's interior are the elastic waves generated by earthquakes or controlled explosions. The travel times of these elastic waves, which are also refracted and reflected within the Earth, are recorded using seismographs stationed all over the globe. After a considerable amount of data is collected, these travel times are inverted to obtain the acoustic velocities of these traveling waves in different regions of the Earth's interior. Thus, the tomographic images representing seismic velocity variations are constructed. The velocity of these waves varies with temperature, pressure, and the chemical composition of the materials through which they propagate.

In order to extract the information form the tomographic images to constrain the composition and thermal structure of the Earth's interior, one needs to know the thermodynamic and thermoelastic properties of the constituent minerals at the high pressure and high temperature conditions typical of the planet's interior. State-of-the-art condensed matter experimental techniques, such as laser-annealed diamond anvil-cells for sample preparation at high pressures, synchrotron X-ray diffraction, transmission electron microscopy, X-ray emission spectroscopy, synchrotron Mössbauer spectroscopy, ultrasonic spectroscopy, and Brillouin scattering spectroscopy have been very useful to

obtain thermal and elastic properties of the Earth's minerals. However, due to (i) extreme pressure and temperature conditions inside the Earth and (ii) intricacy associated with the compositional variations within the minerals (i.e., the presence of iron, aluminum, calcium, and water within the minerals), the available experimental data is far too limited to constrain a robust compositional model for the Earth's interior.

In recent years, quantum mechanical *first-principles* or *ab initio* atomistic simulations have advanced enough to reproduce the available high-pressure and high-temperature experimental measurements of thermodynamic and thermoelastic properties of minerals. Therefore, these first-principles methods enable us to make predictions with confidence even at the extreme temperature and pressure conditions (deep Earth's conditions) which, otherwise, are inaccessible to the laboratory experiments. In addition, they also help us understand the physics behind the experimental observations.

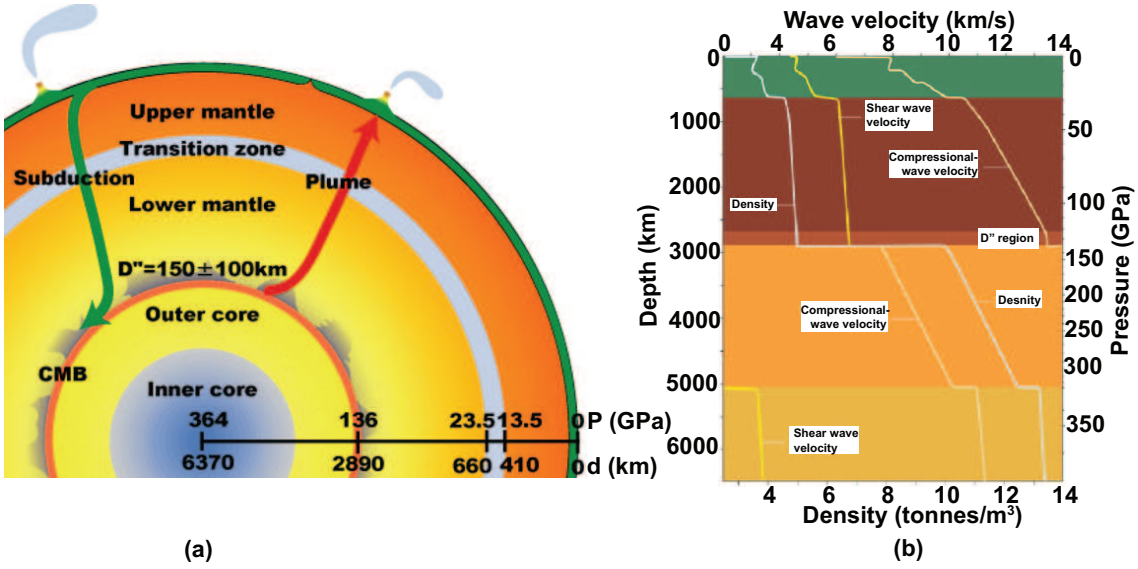

Figure 1.1: (a) Schematic Earth structure, and (b) seismic velocities and density profile based on the Preliminary Reference Earth model (PREM) [1]. CMB: core-mantle boundary.

According to seismological studies based on the Preliminary Reference Earth model (PREM) [1], the Earth is arranged in concentric nested shells separated by seismic discontinuities (Fig. 1.1a). These discontinuities cause separation in the crust, upper mantle, transition zone, lower mantle, outer, and inner core regions. Corresponding one-dimensional variation of the average acoustic velocities and density as function of depth is depicted in Fig. 1.1 b.

The crust, averages ∼7 km underneath the ocean and ∼35 km underneath the continent, mostly consists of silicates containing silicon (Si) and oxygen (O). The Si-O bond in silicates are usually stronger than that between oxygen and any other elements. As a result most silicates are dominated by SiO_4 tetrahedrons and provide a basis to classify silicate minerals in terms of SiO_4 tetrahedrons arrangement. Beneath the crust lies the upper mantle (up to ∼410 Km) and lower mantle (∼660 to 2890 Km) separated by the transition zone. The composition of upper mantle is determined by analyzing the rocks which are brought to the surface by magma during volcanic eruption. The dominant minerals of upper mantle are olivines [$(Mg,Fe)_2SiO_4$], garnets [$(Mg,Fe,Ca)_3Al_2Si_3O_{12}$], and pyroxene [$(Ca,Fe,Mg)SiO_3$ and $(Mg,Fe)SiO_3$] [2]. Based on the peridotitic model of Earth's mantle, the volume fractions of different constituent minerals are schematically shown in Fig. 1.2. High-pressure-high-temperature (High-PT) experiments and first-principles simulations suggest that the upper mantle's minerals transform to denser phases through structural transition at pressure and temperature conditions similar to that in the transition zone, thus explaining the seismic discontinuities demarcating the transition zone region.

The dominant minerals in the Earth's lower mantle based on the peridotitic model are believed to be iron- and aluminum-bearing $MgSiO_3$ perovskite, also known as bridgmanite, (∼75-80 vol%) and (Mg,Fe)O ferropericlase or magnesiowüstite (∼15-18 vol%) along with the small amount (∼5-7 vol%) of $CaSiO_3$ perovskite, SiO_2 stishovite,

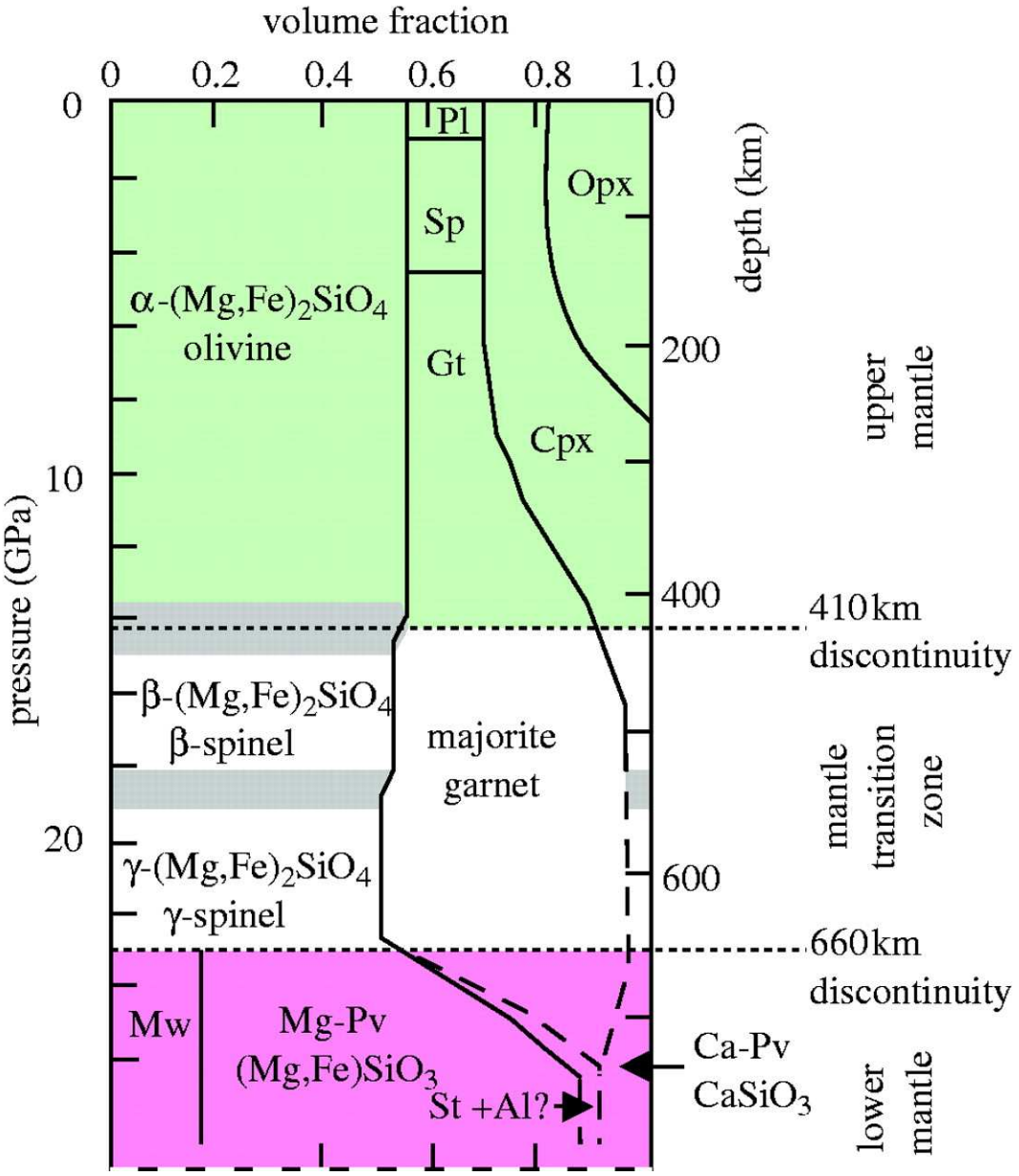

Figure 1.2: Schematic representation of the volume fraction of constituent minerals in the peridotitic model of Earth's mantle as a function of depth (taken from Bovolo; 2005 [2]). Peridotite are brought to the surface by magma form the upper mantle of the Earth. Pl: plagioclase [$CaAl_2Si_2O_8$]; Sp: spinel [$MgAl_2O_4$]; Gt: garnet [$(Mg,Fe,Ca)_3Al_2Si_3O_{12}$]; majorite garnet: $Mg3(Mg,Si)_2Si_3O_{12}$; Cpx: clinopyroxene [$(Ca,Fe,Mg)SiO_3$]; Opx: orthopyroxene [$(Mg,Fe)SiO_3$]; Mg-Pv: Mg-perovskite [$(Mg,Fe)SiO_3$, also known as bridgmanite]; olivine [$(Mg,Fe)_2SiO_4$]; Mw: magnesiowüstite [(Mg,Fe)O]; Ca-Pv: Ca-perovskite [$CaSiO_3$]; and St: stishovite [SiO_2].

and some watter components. $MgSiO_3$ perovskite further transforms to another high-pressure phase, called post-perovskite, in the pressure and temperature conditions that are likely to occur in the lowermost part of the lower mantle near core-mantle boundary (known as the D" region). It must be carefully noted that the exact proportions of these minerals in the lower mantle is still not known and highly debated.

The estimated pressure in the lower mantle ranges approximately from ∼23.5 GPa to 136 GPa. Temperature variation as a function of depth (known as geotherm) are usually estimated by anchoring the temperatures at seismic discontinuities and using appropriate model for heat transfer inside the Earth. Based on the whole mantle convection model, the temperature is estimated in the range ∼1876 to 2450 K [4], while based on layered convection model it is around ∼1980 to 3000 K [5] (Fig. A.1). It is extremely challenging to conduct laboratory experiments to measure thermal and elastic properties of the minerals under such a high pressure and temperature conditions. The complexity further increases in the bridgmanite samples due to varying valence states of iron (i.e., ferrous, Fe^{2+}, and ferric, Fe^{3+} iron) and iron spin states changes with the application of pressure. As shown in Fig. 1.3, the $3d$-orbitals in an octahedral surrounding of oxygen atoms split into e_g and t_{2g} states with an energy gap U_{CF} (called crystal-field splitting energy). The energy splitting between parallel and anti-parallel spin is given by U_X. The spin state changes of iron are primarily driven by the competition between U_{CF} and U_X. At ambient pressure, the value of U_X is usually larger than that of U_{CF} and the ground state of the system would be in the high-spin (HS) state. Crystal-field energy U_{CF} increases with increasing pressure and may overcome the exchange energy U_X at some pressure P_T (transition pressure) resulting in the change of spin-state of the system. In spite of the considerable effort to understand the pressure induced iron spin crossover and its consequences to the lower mantle composition, the issue is not yet resolved completely and is highly debated. The pressure induced spin crossover

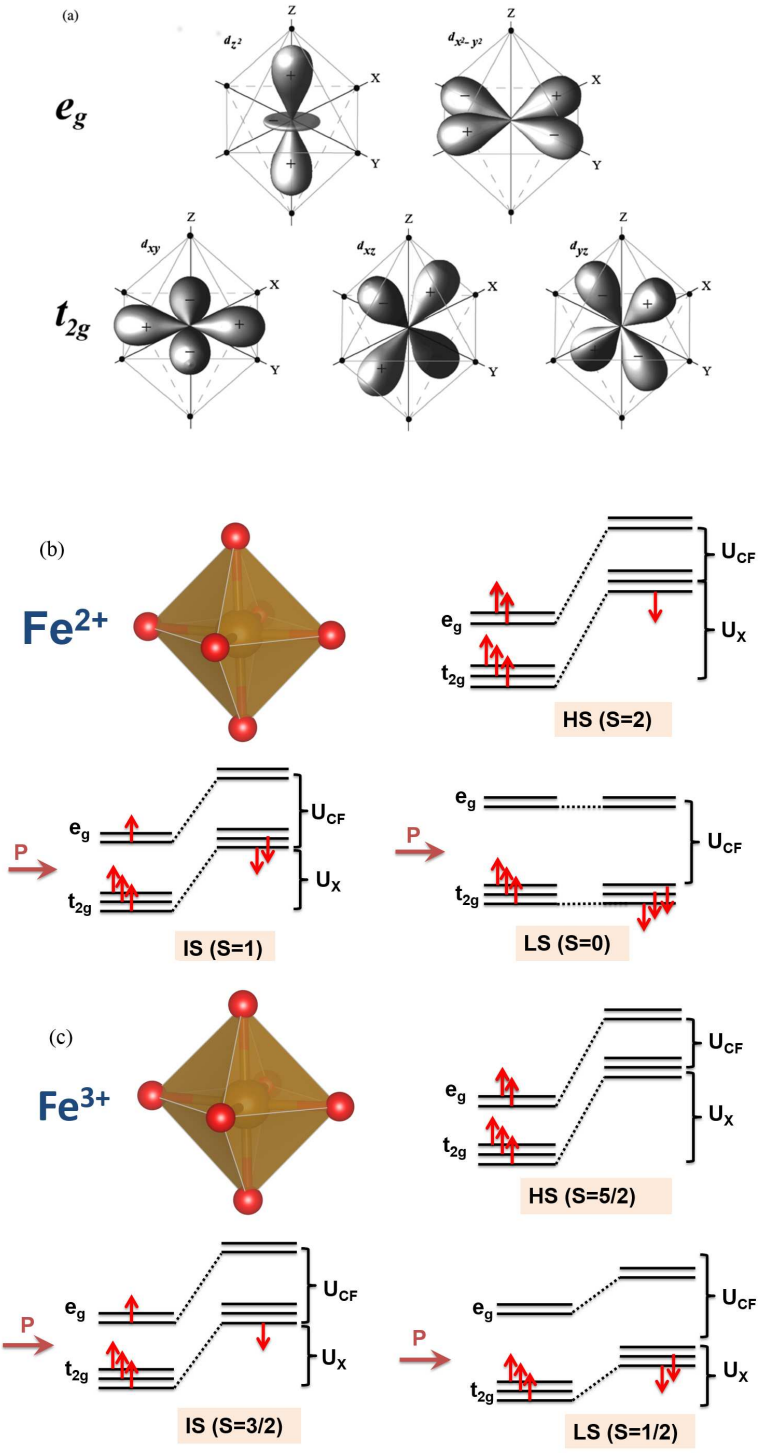

Figure 1.3: (a) $3d$ orbitals splitting into e_g and t_{2g} orbitals in an octahedral environment (Fig. 1.3a is taken from Lin *et al.*; 2013 [3]). Pressure induced spin state changes in (b) ferrous, Fe^{2+}, and (c) ferric, Fe^{3+}, iron. U_{CF} and U_X represent crystal-field splitting energy and spin-exchange energy, respectively. HS: high-spin, IS: intermediate spin, and LS: low-spin.

generally leads to volume collapse and may affect the elastic properties of the minerals substantially.

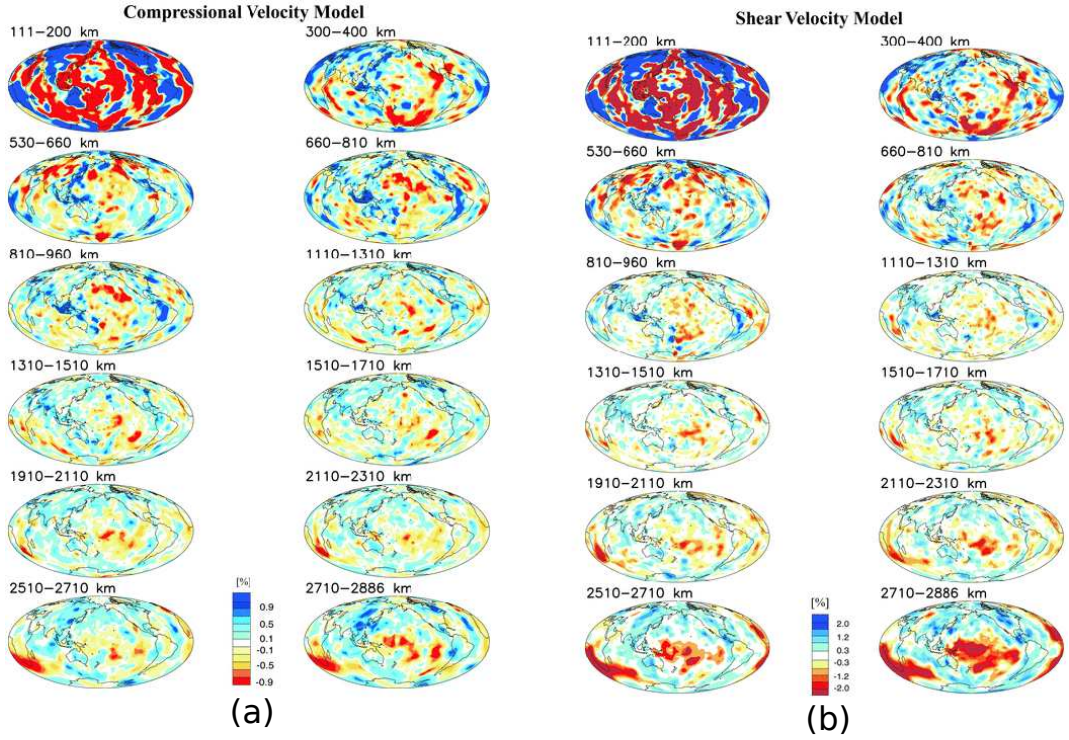

Figure 1.4: Lateral velocity variation model for (a) the compressional velocity, V_P, and (b) shear velocity, V_S. (Figure is taken from Houser *et al.*; 2008 [7]). Blue and red colors, respectively, represent the fastest and slowest region with respect to the average velocity (white region) as a function of depth.

In order to unravel the three-dimensional (3D) structure of the Earth's interior, recently there have been many seismic investigations (seismic tomography) revealing the lateral variations of seismic velocities in the Earth's mantle (Fig. 1.4). Deciphering these variations would require an accurate estimate of thermal and elastic properties of the constituent minerals. Owing to the uncertainties associated with the physical properties of the lower mantle minerals, there exists several compositional models in the literature, each having different and significant implications for the lower mantle

structure. However, none of these models reveal the whole picture about the lower mantle composition and thermal structure consistently.

In an effort to provide accurate thermal and elastic properties of the constituent minerals of the Earth's interior, we present in this thesis a first-principles investigation of Fe- and Al-bearing $MgSiO_3$ perovskite (bridgmanite), the most abundant mineral (75-80 vol%) of the Earth's lower mantle. The concentration of Fe and Al in the bridgmanite mineral is expected to be approximately ∼10 mol% and ∼5 mol%, respectively. The iron can be present as ferrous iron (Fe^{2+}), with six $3d$ electrons, and ferric iron (Fe^{3+}), with five $3d$ electrons. The electronic configurations of iron could be significantly altered due to lower mantle high pressure and temperatures, which consequently may lead to a spin state transition. Therefore, we first investigate the pressure induced iron state changes in bridgmanite and then study its consequences to high pressure and high temperature thermal and elastic properties. In order to treat the electronic localization of iron's $3d$-orbitals properly, we have used the *density functional theory* augmented by the Hubbard-type correction (DFT+U) as implemented in the quantum-ESPRESSO package [8]. The value of Hubbard parameter U has been calculated self-consistently using linear response approach by Cococcioni and coauthors [10, 11]. The equilibrium geometry of the crystal at various pressures have been obtained using the *variable cell-shape molecular dynamics* (VCS-MD) method developed by Wentzcovitch and coauthors [13, 14]. The *local density approximation* (LDA) and the *generalized gradient approximation* (GGA) for exchange-correlation potential of electrons have been used to study pressure induced iron state changes. It is well known that the LDA functional generally provide a better agreement with experimentally measured structural and elastic properties, so the calculations of thermoelastic properties have been performed within the LDA. Thermal effects have been addressed by taking into account the atomic vibrations within the *quasiharmonic approximation* (QHA) [120]. The QHA is expected to work quite well

below the Debye temperature. The melting temperature and the Debye temperature of the material increase with increasing pressure. Therefore, the temperature range over which the QHA description of atomic vibrations is supposed to work also increases. As a result, the high pressure and high temperature thermoelastic properties of the lower mantle minerals such as bridgmanite can be described very well within the QHA. The vibrational frequencies, needed for the free-energy calculation within QHA, have been computed using *density functional perturbation theory* (DFPT) [121, 123].

The thesis is organized as follows: In Chapter 2, we describe brief theoretical underpinnings for *first-principles* calculations presented in this study. In Chapter 3, the pressure induced iron state changes in Fe-bearing $MgSiO_3$ perovskite and post-perovskite structures are investigated. Results are compared with Fe-bearing $MgGeO_3$ (a low pressure analog of $MgSiO_3$). We find that in the entire lower mantle pressure range ($\sim$23.5 to 136 GPa), iron (both ferrous and ferric) replacing magnesium, $[Fe^{2+}]_{Mg}$ and $[Fe^{3+}]_{Mg}$, remains in the high spin state while the ferric iron replacing silicon, $[Fe^{3+}]_{Si}$, goes from high spin to the low spin state. We also study the effect of iron state changes on the post-perovskite transition. In Chapter 4, we further investigate the spin crossover of $[Fe^{3+}]_{Si}$ by incorporating the effects of disorder, iron concentration, and temperature. In Chapter 5, we present the calculations of thermoelastic properties for iron-free and $[Fe^{2+}]_{Mg}$-bearing bridgmanite. In Chapter 6, we investigate the effect of Fe^{3+} and Al^{3+} substitutions on the elasticity of bridgmanite. We particularly focus on the volume collapse due to high spin to low spin transition in $[Fe^{3+}]_{Si}$ and its consequences to the elastic properties. In the charge-coupled substitution of Fe^{3+}-Al^{3+}, Al^{3+} would energetically prefer to be in the Si site and the spin crossover in $[Fe^{3+}]_{Si}$ and its elastic consequences may disappear. Finally, in Chapter 7, we summarize our conclusions.

Chapter 2

Theoretical methods

The chapter briefly documents the important theoretical fundamentals used for *ab initio* or *first-principles* investigation of the Earth's lower mantle minerals. Starting from the quantum mechanical principles, we present the framework of density functional theory (DFT) and DFT + U, followed by the variable cell shape molecular dynamics (VCS-MD) [13, 14] used to obtain equilibrium structure at relevant pressures. We also discuss density functional perturbation theory (DFPT) that has been used to simulate thermal and elastic properties of the minerals within the quasi harmonic approximation (QHA).

2.1 Born Oppenheimer approximation

The quantum mechanical many-body Hamiltonian for a system of electrons and ions [17] is given by

$$\hat{H} = -\frac{\hbar^2}{2m_e}\sum_i \nabla_i^2 + \frac{1}{2}\sum_{i\neq j}\frac{e^2}{|\mathbf{r}_i - \mathbf{r}_j|} + \sum_{i,\alpha}\frac{Z_\alpha e^2}{|\mathbf{r}_i - \mathbf{R}_\alpha|} - \sum_\alpha \frac{\hbar^2}{2M_\alpha}\nabla_\alpha^2 + \frac{1}{2}\sum_{\alpha\neq\beta}\frac{Z_\alpha Z_\beta e^2}{|\mathbf{R}_\alpha - \mathbf{R}_\beta|}, \tag{2.1}$$

where index i,j and α,β represent electrons and ions, respectively. In equation 2.1, the first term represent the kinetic energy of the electrons ($\hat{T}_{\mathbf{r}}$), the second is the mutual interaction among the electrons ($\hat{V}_{ee}$), the third is the Coulomb potential acting on the electrons due to ions ($\hat{V}_{ext}$), the fourth is the kinetic energy of the ions ($\hat{T}_{\mathbf{R}}$), and the last term is the Coulomb interaction among the ions ($\hat{V}_{II}$). The quantum mechanical solution for the system described by this Hamiltonian is given by the Schrödinger equation

$$\hat{H}\Psi(\mathbf{r},\mathbf{R}) = E\Psi(\mathbf{r},\mathbf{R}), \tag{2.2}$$

where $\Psi(\mathbf{r},\mathbf{R})$ is complicated many-body wave function where electronic and ionic degrees of freedom are coupled together. The exact solution of eq. 2.2 is not possible for a real system. However, the electronic and ionic degrees of freedom can be decoupled within the Born-Oppenheimer (B-O) or adiabatic approximation. This approximation relies on the fact that mass of the electron is much smaller than that of ions and the kinetic energy of ions would be very small compare to that of electrons. Therefore, for a particular ionic arrangement, a relaxed electronic configuration can be considered to be in the ground state. Within the B-O approximation, the total quantum mechanical wave function for the system can be written as the product of ionic ($\Phi(\mathbf{R})$) and electronic wave function for a particular ionic configuration ($\psi_{\mathbf{R}}(\mathbf{r})$)

$$\Psi(\mathbf{r},\mathbf{R}) = \Phi(\mathbf{R})\psi_{\mathbf{R}}(\mathbf{r}), \tag{2.3}$$

where $\mathbf{r}$=$\{r_i\}$ and $\mathbf{R}$=$\{R_\alpha\}$ are the set electronic and ionic coordinates, respectively. Using eq. 2.3 and ignoring the term $\hat{T}_{\mathbf{R}}\psi_{\mathbf{R}}(\mathbf{r})$, the Schrödinger equation for the electrons under the external potential due to ions can be written as

$$\left(-\frac{\hbar^2}{2m_e}\sum_i \nabla_i^2 + \frac{1}{2}\sum_{i\neq j}\frac{e^2}{|\mathbf{r}_i-\mathbf{r}_j|} + \sum_{i,\alpha}\frac{Z_\alpha e^2}{|\mathbf{r}_i-\mathbf{R}_\alpha|} + \frac{1}{2}\sum_{\alpha\neq\beta}\frac{Z_\alpha Z_\beta e^2}{|\mathbf{R}_\alpha-\mathbf{R}_\beta|}\right)\psi^s_{\mathbf{R}}(\mathbf{r}) = \\ = E_s(\mathbf{R})\psi^s_{\mathbf{R}}(\mathbf{r}), \tag{2.4}$$

where the upper index s indicates the quantum number of electronic states. Similarly the Schrödinger equation describing the ions is

$$\left(-\sum_{\alpha}\frac{\hbar^2}{2M_\alpha}\nabla_\alpha^2 + E(\mathbf{R})\right)\Phi(\mathbf{R}) = \varepsilon\Phi(\mathbf{R}), \tag{2.5}$$

where E($\mathbf{R}$) is the ground state energy of the electrons for a fixed ionic configuration $\mathbf{R}$ (i.e. ground state solution of eq. 2.4) which is also known as *Born-Oppenheimer potential energy surface* for the ions due to electrons.

Although B-O approximation is very useful simplification of the problem, which allows us to treat ionic and electronic degrees of freedom separately, the Schrödinger equation describing electrons (eq. 2.4) is still much more complicated to be solved exactly due to mutual interaction among the electrons. Density functional theory provides a framework to perform practical calculations and find the solution for the real system.

2.2 Density functional theory

DFT provides a way to systematically describe the ground state properties of a system in terms of the ground state electronic charge density. Hohenberg and Kohn demonstrated that for any system of interacting particles in an external potential, there exists a one to one correspondence between the external potential and the ground state electron density of the system [15]. Due to this one to one correspondence, there also exists a universal functional for the energy E[n($\mathbf{r}$)] in terms of the density n($\mathbf{r}$). The global minimum of this functional provides the exact ground state energy for the system and the density which minimizes the functional is the exact ground state density $n_0(\mathbf{r})$. For a external potential $V_{ext}(\mathbf{r})$ acting on the system of electrons (i.e., Coulomb potential due to nuclei), the energy functional is given by

$$E[n(\mathbf{r})] = F[n(\mathbf{r})] + \int V_{ext}(\mathbf{r})n(\mathbf{r})d\mathbf{r} + E_{II} \tag{2.6}$$

where F[n(**r**)] contains the kinetic energy and mutual Coulomb interaction among the electrons. E_{II} is the energy due to mutual interaction among the ions. The minimization of the functional E[n(**r**)] with the constrain that total number of electrons is preserved, i.e.,

$$\int n(\mathbf{r})d\mathbf{r} = N, \tag{2.7}$$

gives the ground state energy and the ground state electron density of the system. In spite of these conceptually appealing developments, the practical use of the DFT formulation was still not possible due to lack of any appropriate formulation for the functional F[n(**r**)]. Kohn and Sham proposed a further development by mapping the complicated many-body interacting system into a fictitious non-interacting one [16] and made DFT powerful computational tool to study real system.

2.3 Kohn-Sham equations

Kohn and Sham proposed to replace the many-body interacting system obeying equation 2.4 with a different *auxiliary non-interacting system* which can be described with the single particle Schrödinger equations in an *effective local potential* [16]. The ground state electron density of the chosen auxiliary non-interacting system has been assumed to be equal to that of original interacting one. Since the chosen auxiliary system also obeys the Hohenberg and Kohn theorem, the functional F[n(**r**)] for this system corresponds to the kinetic energy of non-interacting electrons. Therefore, the functional F[n(**r**)] for the real interacting electron system can be written as

$$F[n(\mathbf{r})] = T_0[n(\mathbf{r})] + E_{Hartree}[n(\mathbf{r})] + E_{xc}[n(\mathbf{r})], \tag{2.8}$$

where $T_0[n(\mathbf{r})]$ is the kinetic energy for the non-interacting electrons with density $n(\mathbf{r})$. The $n(\mathbf{r})$ is given by

$$n(\mathbf{r}) = \sum_{i=1}^{N} |\psi_i(\mathbf{r})|^2. \tag{2.9}$$

The kinetic energy $T_0[n(\mathbf{r})]$ can be written as

$$T_0[n(\mathbf{r})] = -\frac{\hbar^2}{2m_e} \sum_{i=1}^{N} \langle \psi_i | \nabla_i^2 | \psi_i \rangle. \tag{2.10}$$

$E_{Hartree}[n(\mathbf{r})]$ is the classical Coulomb interaction energy of the electron density $n(\mathbf{r})$ interacting with itself

$$E_{Hartree}[n(\mathbf{r})] = \frac{e^2}{2} \int d\mathbf{r} d\mathbf{r}' \frac{n(\mathbf{r}) n(\mathbf{r}')}{|\mathbf{r} - \mathbf{r}'|}. \tag{2.11}$$

The exchange-correlation energy ($E_{xc}[n(\mathbf{r})]$), that contains all the many body effects of the interacting electrons, can be written as

$$\begin{aligned} E_{xc}[n(\mathbf{r})] &= F[n(\mathbf{r})] - (T_0[n(\mathbf{r})] + E_{Hartree}[n(\mathbf{r})]) \\ &= \left(\langle \hat{T}_{\mathbf{r}} \rangle - T_0[n(\mathbf{r})] \right) + \left(\langle \hat{V}_{ee} \rangle - E_{Hartree}[n(\mathbf{r})] \right). \end{aligned} \tag{2.12}$$

Equation 2.12 shows that E_{xc} is the difference of kinetic and electron-electron interaction energies of the original many-body system from those of the auxiliary non-interacting system with electron-electron interactions replaced by Hartree energy.

The total energy of the interacting electron system

$$E_{KS}[n(\mathbf{r})] = T_0[n(\mathbf{r})] + E_{Hartree}[n(\mathbf{r})] + E_{xc}[n(\mathbf{r})] + \int V_{ext}(\mathbf{r}) n(\mathbf{r}) d\mathbf{r} + E_{II} \tag{2.13}$$

and of the non-interacting auxiliary system

$$E^0_{KS}[n(\mathbf{r})] = T_0[n(\mathbf{r})] + \int V_{KS}(\mathbf{r}) n(\mathbf{r}) d\mathbf{r} + E_{II} \tag{2.14}$$

are to be minimized at the same electron density $n(\mathbf{r})$ with the constrain $\int n(\mathbf{r}) d\mathbf{r} = N$. Then the expression for the Kohn-Sham potential V_{KS} is

$$V_{KS}(\mathbf{r}) = V_{ext}(\mathbf{r}) + \left(e^2 \int d\mathbf{r}' \frac{n(\mathbf{r}')}{|\mathbf{r} - \mathbf{r}'|} \right) + \frac{\delta E_{xc}[n(\mathbf{r})]}{\delta n(\mathbf{r})}. \tag{2.15}$$

If the functional $E_{xc}[n(\mathbf{r})]$ is known, then the original many-body interacting system can be described as the non-interacting electron gas under an effective potential $V_{KS}(\mathbf{r})$.

Using equations 2.9 and 2.10, energy $E^0_{KS}[n(\mathbf{r})]$ can be expressed in terms of single particle wave function $\psi_i(\mathbf{r})$ and minimization of $E^0_{KS}[n(\mathbf{r})]$ with the constrain $\int n(\mathbf{r})d\mathbf{r} = N$ is equivalent to minimization with respect to wave function, i.e.,

$$\frac{\delta E^0_{KS}}{\delta \psi^*_i} = 0 \tag{2.16}$$

subject to orthonormality constrains

$$\int \psi^*_i(\mathbf{r})\psi_j(\mathbf{r})d\mathbf{r} = \delta_{i,j}. \tag{2.17}$$

This leads to the single particle Schrödinger-like equations

$$\hat{H}_{KS}\psi_i(\mathbf{r}) = \left(-\frac{\hbar^2}{2m_e}\nabla^2_i + V_{KS}\right)\psi_i(\mathbf{r}) = \epsilon_i\psi_i(\mathbf{r}), \tag{2.18}$$

where ϵ_i are the eigenvalues of the Kohn-Sham Hamiltonian. Equations 2.18 along with 2.9 and 2.15 are known as Kohn-Sham equations. It is worth to mention here that wave functions ψ_i appearing in Kohn-Sham equations have no direct physical meaning as these are the eigenfunctions of the auxiliary fictitious non-interacting system whose only the ground state electron density is equal to that of the real system.

Thus, the Kohn-Sham approach allows us to describe the complicated many-body interacting system in terms of the fictitious non-interacting system in an effective potential V_{KS}. However, these equations are highly non-linear since the potential V_{KS} entering in the Schrödinger-like equations 2.18 itself depends on the solution of these equations. Therefore, the solution of the Kohn-Sham equations must be found self-consistently.

In principle, the DFT framework described above provides a way to calculate ground state properties of the real system exactly, provided the functional $E_{xc}[n(\mathbf{r})]$ is known for that system. In practice, however, the exact formulation of $E_{xc}[n(\mathbf{r})]$ is unknown and one has to rely on a reasonable *approximate* description of this functional. The success

of DFT for a real system depends on how well the exchange-correlation contribution (E_{xc}) is described.

2.4 The local density and generalized gradient approximation for the functional $\mathbf{E}_{xc}$

In order to make DFT a practical tool for *ab-inito* or *first-principles* calculations, reasonable approximations are needed for the functional E_{xc}. In the Kohn-Sham formalism, the independent particle kinetic energy and long-range Hartree terms are explicitly separated from the exchange-correlation term, which could be reasonably approximated as a local or nearly local functional of the electron density [17]

$$E_{xc}[n(\mathbf{r})] = \int n(\mathbf{r})\epsilon_{xc}[n(\mathbf{r}), \mathbf{r}], \tag{2.19}$$

where $\epsilon_{xc}[n(\mathbf{r}), \mathbf{r}]$ is the exchange-correlation energy per electron (i.e., exchange-correlation energy density) at point $\mathbf{r}$ which depends on the density $n(\mathbf{r})$ in the neighborhood of point $\mathbf{r}$.

It was also pointed out by Kohn and Sham that solids can often be considered to close to the limit of homogeneous electrons gas and that the effects of exchange and correlations are local in nature. In that limit, exchange-correlation energy density $\epsilon_{xc}[n(\mathbf{r}), \mathbf{r}]$ for the real system can be considered to be equal to that of homogeneous electron gas with the same density n($\mathbf{r}$). This approximation is known as the *local density approximation* (LDA). The functional Exc within LDA is given by

$$E_{xc}^{LDA} = \int n(\mathbf{r})\epsilon_{xc}^{hom}[n(\mathbf{r})]d\mathbf{r}, \tag{2.20}$$

where $\epsilon_{xc}^{hom}[n(\mathbf{r})]$ is the exchange-correlation energy density for the homogeneous electron gas. The exchange part of $\epsilon_{xc}^{hom}[n(\mathbf{r})]$ can be expressed analytically while the correlation part is to be calculated based on quantum Monte Carlo simulations [18].

In spite of such a simple description of $\epsilon_{xc}^{hom}[n(\mathbf{r})]$, LDA has been very successful in *ab-inito* calculations, especially for the structural and vibrational properties of metals, semiconductor, and insulators. However, it often fails to estimate the correct band gaps for insulators and semiconductors, and predicts incorrect ground states for some the transition metals. In order to overcome these difficulties, the local density approximation was extended by incorporating the gradient of the density $|\nabla n(\mathbf{r})|$. This approximation is known as *generalized gradient approximation* (GGA) [19]. Within GGA, then functional E_{xc} is given by

$$E_{xc}^{GGA} = \int n(\mathbf{r})\epsilon_{xc}^{hom}\left[n(\mathbf{r}), |\nabla n(\mathbf{r})|\right] d\mathbf{r}. \tag{2.21}$$

The GGA improves the estimate of energy band gaps for the insulator and semiconductors but does not work well for the structural and elastic properties of the solids.

2.5 Periodic systems and Bloch's theorem

In a perfect crystal, atoms form an infinite periodic structure. Therefore, the external potential due to ions is also periodic

$$V_{ext}(\mathbf{r}) = V_{ext}(\mathbf{R} + \mathbf{r}), \tag{2.22}$$

where $\mathbf{R}$ is the *translational vector* which is an integer linear combination of three fundamental lattice vectors describing primitive unit cell of the crystal. For this translational invariance, Bloch's theorem allows us to express the single particle wave function as

$$\psi_{\mathbf{k},\nu}(\mathbf{r}) = \exp^{i\mathbf{k}.\mathbf{r}} u_{\mathbf{k},\nu}(\mathbf{r}) \tag{2.23}$$

where $\mathbf{k}$ is the electron wave vector in the crystal within the first Brillouin Zone (also called crystal momentum) and the ν is the band index for a given wave vector $\mathbf{k}$. The function $u_{\mathbf{k},\nu}(\mathbf{r})$ also has the periodicity of the crystal, i.e.,

$$u_{\mathbf{k},\nu}(\mathbf{r}) = u_{\mathbf{k},\nu}(\mathbf{R}+\mathbf{r}). \tag{2.24}$$

The periodicity of the function $u_{\mathbf{k},\nu}(\mathbf{r})$ allows us to expand the electronic wave function 2.23 in terms of plane waves

$$\psi_{\mathbf{k},\nu}(\mathbf{r}) = \frac{1}{\sqrt{N\Omega}} \sum_{\mathbf{G}} C_\nu(\mathbf{k}+\mathbf{G}) \exp^{i(\mathbf{k}+\mathbf{G}).\mathbf{r}} \tag{2.25}$$

and the wave vectors $\mathbf{G}$ are the reciprocal lattice vectors which are constrained by

$$\mathbf{G}.\mathbf{R} = 2\pi m, \tag{2.26}$$

where m is an integer. Ω is the volume of the primitive unit cell (i.e., the cell that contains one atom) and N are the total number of atoms in the crystal. Using plane wave expansion 2.25, integro-differential Kohn-Sham equations (2.18) can be transformed into a set of algebraic equations

$$\sum_{\mathbf{G}'} \left[\frac{\hbar^2}{2m_e} |\mathbf{k}+\mathbf{G}|^2 + V_{KS}(\mathbf{G}\text{-}\mathbf{G}') \right] C_\nu(\mathbf{k}+\mathbf{G}') = \epsilon_{\mathbf{k},\nu} C_\nu(\mathbf{k}+\mathbf{G}), \tag{2.27}$$

where $V_{KS}(\mathbf{G}\text{-}\mathbf{G}')$ is Fourier component of Kohn-Sham potential (2.15) at wave vector $\mathbf{G}\text{-}\mathbf{G}'$. The coefficients $C_\nu(\mathbf{k}+\mathbf{G})$ are normalized as

$$\sum_{\mathbf{G}} |C_\nu(\mathbf{k}+\mathbf{G})|^2 = 1. \tag{2.28}$$

Thus, the set of Kohn-Sham equations for infinite number of electrons (for fictitious particles to be more precise) in the crystal are being mapped into a set of algebraic equations at infinite number of wave vectors $\mathbf{k}$ within the first Brillouin Zone (BZ). The electron density n($\mathbf{r}$) and other physical properties require sum over the all electronic states which corresponds to the integration over first BZ and sum over the band index ν. In practice, the integration over the first BZ can be confined to smaller region of the BZ (known as irreducible wedge of the Brillouin Zone or IBZ) and the resulting integration can be converted to finite sum over special wave vectors $\mathbf{k}$ within the IBZ. In this work we have used Monkhorst-Pack technique [20] for $\mathbf{k}$-space integration. Since

DFT is used to calculate ground state properties of the system, only a finite number of lowest energy band-states (ν) at a given **k**-vector are required for the electronic charge density computation. In principle, the plane wave expansion (eq. 2.25) would need infinite number of reciprocal vectors **G** for exact calculations. However, in practice, only a finite number of wave vectors are chosen and this choice is constrained by the energy cut-off E_{cut} as

$$\frac{\hbar^2}{2m_e}|\mathbf{k}+\mathbf{G}|^2 \leq E_{cut}. \tag{2.29}$$

For practical calculation, one has to start with an appropriate choice of **k**-vector grid and E_{cut} value then the accuracy of the solution of Kohn-Sham equations is checked by increasing the density of **k**-vector grid and the value of E_{cut} until the convergence is achieved for the total energy, forces, stresses, and other desired physical properties of the system.

The plane wave expansion of the electronic wave function is very useful as it converts the Kohn-Sham equations into a set of algebraic equations and the solution involves the numerical diagonalization of the Kohn-Sham Hamiltonian. The size of this Hamiltonian matrix is determined by the choice of E_{cut}. The parameter E_{cut} controls the accuracy of the calculation as it estimates the distance $\sim 2\pi\hbar/\sqrt{2m_eE_{cut}}$ beyond which the variation of the electronic wave functions can be well described.

2.6 Pseudopotential method

Although the plane wave expansion of the electronic wave function (eq. 2.25) is helpful to numerically solve the Kohn-Sham equations for the real systems, but it would require a large number of plane waves (i.e., wave vectors **G**) to accurately describe the rapidly oscillating wave functions of the electrons in and around the ionic core (nuclei bonded by inert electrons) region. To circumvent this problem, pseudopotential (PP) method

[21, 22, 23, 24, 25] has been employed as it reduces the computational cost substantially.

The pseudopotential method is based on the assumption that the relevant physical and chemical properties of an atom in crystals are described by valence electrons, while the core electrons, which are inert and tightly bonded to the nuclei, do not respond substantially to the external environment and can be considered as frozen in their atomic environment. This means, the valence electrons move in an effective potential produced by ionic cores. Scattering properties of a localized spherical potential at any energy can be formulated quantum mechanically in terms of the phase shift. All the properties of the wave function outside the scattering region are invariant provided the phase shift changes only varies by integer multiple of 2π. The pseudopotential approximation replaces the strong potential of the ionic cores with an effective weak potential, which acts on the pseudo wave functions rather than the true wave function of the valence electrons and reproduces all relevant properties outside the core region.

The basic idea is that the full potential for an isolated atom is calculated using the all electron method (AE). The electronic states are divided into core and valence states. The core electrons are considered to be frozen in their ground states and pseudo wave functions for the valence electrons are built, in such a way, that they are smooth and nodeless in the core region and match the true wave functions in the valence region. Owing to the smoothness of the pseudo wave functions, solutions of the Kohn-Sham equations in the plane-wave basis sets (eq. 2.27) can be obtained with a reasonable number of wave vectors $\mathbf{G}$. Hence, the computational cost can be drastically reduced compared to the all electron calculations. However, the transferability of the pseudopotential to the different chemical environment depends on how well the scattering properties of the 'true' valence states are reproduced in the required energy range to describe the system. For this purpose, pseudopotential is usually divided into local and

non-local part (which depends on the angular momentum l):

$$V^{pseudo}(\mathbf{r},\mathbf{r}') = V^{local}(r)\delta(r-r') + \sum_{l} V_l(r)\delta(r-r')P_l(\mathbf{r}-\mathbf{r}'), \tag{2.30}$$

where the projector P_l acts on the l^{th} angular momentum subspace. The first term in the eq. 2.30 matches the real potential in the valence region and second one (non-local) vanishes outside the core and ensures that each angular momentum is treated differently in order maintain good transferability of the potential.

There are several methods available in the literature to generate the pseudopotentials, depending on the specific requirements to describe a particular feature of the system. In this work, the ultrasoft pseudopotentials have been used for aluminum (Al), oxygen (O), iron (Fe), and silicon (Si) atoms, while the norm-conserving one is used for the magnesium (Mg) atom. These norm-conserving and ultrasoft methods are briefly described here.

2.6.1 Norm-conserving pseudopotential method

The basic requirements for generating good norm-conserving pseudopotentials were proposed by Hamann and coauthors [26]:

- Real (all electron) and pseudo wave functions have the same eigenvalues for the valence states in a given configuration.
- Real and pseudo wave functions for a given angular momentum l should agree in the valence region (i.e., outside the l-dependent core radius $R_{c,l}$).
- The pseudo wave functions must be nodeless except at the origin.
- The charge enclosed within the core radius $R_{c,l}$ must be equal for real and pseudo wave function (norm-conserving condition):

$$\int_0^{R_{c,l}} |\psi_{n,l}^{real}(r)|^2(4\pi r^2)dr = \int_0^{R_{c,l}} |\psi_{n,l}^{pseudo}(r)|^2(4\pi r^2)dr. \tag{2.31}$$

- The logarithmic derivatives of the real and pseudo wave functions must agree at $R_{c,l}$.

- The first energy derivative of these logarithmic derivatives the real and pseudo wave functions i.e., $\frac{\partial}{\partial E}\left(\frac{\partial}{\partial r} ln[\psi_{n,l}^{pseudo}(r)]\right)$ must also agree at $R_{c,l}$.

The last requirement determines the transferability of the norm-conserving pseudopotentials in a desired energy range. The identity

$$-2\pi\left[[r\psi_{n,l}(r)]^2 \frac{\partial}{\partial E}\left(\frac{\partial}{\partial r} ln[\psi_{n,l}(r)]\right)\right]_{R_{c,l}} = \int_0^{R_{c,l}} |\psi_{n,l}(r)|^2 (4\pi r^2) dr \qquad (2.32)$$

along with the norm-conserving condition ensure that the logarithmic derivatives $\left(\frac{\partial}{\partial r} ln[\psi_{n,l}(r)]\right)$ at $R_{c,l}$ are correct to the linear order of the energy E. The recipe of Troullier and Martins [27] has been used to construct the norm-conserving pseudopotential.

2.6.2 Ultrasoft pseudopotential method

For the atoms with strongly oscillating pseudo wave functions, the pseudopotentials would be 'hard' since they require a large number of plane waves (wave vectors $\mathbf{G}$) to find the solution of Kohn-Sham equations and any attempt to make these pseudopotentials 'soft' just by simply increasing the core radius $R_{c,l}$ would result in poor transferability to different environment. Vanderbilt and coauthors [28, 29] found a way to increase the softness of potential drastically (the so called ultrasoft pseudopotentials) while maintaining the good transferability. They relaxed the norm-conserving condition, while maintaining the accuracy by introducing an extra auxiliary function along with the smoother pseudo wave functions for every angular momentum state l in the non-local part of the potential in equation 2.30.

2.7 DFT+U method

These standard approximations for E_{xc} described above (LDA and GGA) are mean-field like approximations, which usually work for the system with weakly correlated or delocalized electrons. However, for the system of strongly correlated or localized electrons such as those with d- and f-orbital electrons, these LDA and GGA functionals are not sufficient to capture the many-body effects. For this reason, Anisimov and coauthors [30, 31, 32] introduced the correction to these standard functionals in the spirit of Hubbard model [33, 34, 35, 36, 37, 38]. The electronic states space can be divided into subspace of correlated or localized states (i.e., d-states) and subspace of uncorrelated or delocalized states (i.e., s- and p-states). The delocalized states can be described with standard DFT functionals and the Coulomb interaction of localized d-states with 'on-site' interaction

$$E_{Hub} = \frac{1}{2}U \sum_{l \neq l'} n_l n_{l'}, \tag{2.33}$$

where n_l represents the electronic population of l^{th} d-orbital and the total number of electrons in d-orbitals will be $n_d = \sum_l n_l$. However, standard DFT functionals already describe the correlations of d-orbitals in a mean-field like approach and this contribution must be subtracted in order to avoid the *double counting* of the same interaction. Within the mean-field approximation, this double counting (dc) contribution can reasonably be approximated as

$$E_{dc} = \frac{1}{2}U n_d(n_d - 1). \tag{2.34}$$

The energy functional within DFT+U method is then given by

$$\begin{aligned} E_{DFT+U}[n(\mathbf{r})] &= E_{DFT}[n(\mathbf{r})] + E_U[n_{l,l'}] = E_{DFT}[n(\mathbf{r})] + E_{Hub}[n_{l,l'}] - E_{dc}[n_d] \\ &= E_{DFT}[n(\mathbf{r})] + \frac{1}{2}U \sum_{l \neq l'} n_l n_{l'} - \frac{1}{2}U n_d(n_d - 1), \end{aligned} \tag{2.35}$$

where $E_{DFT}[n(\mathbf{r})]$ is the standard DFT energy functional (i.e., LDA and GGA functionals). The inclusion of Hubbard type correction introduces the energy gap of width $\sim U$ between occupied and unoccupied orbitals, which can be seen explicitly in the following expression for the orbital energy

$$\epsilon_l^{DFT+U} = \frac{\partial E_{DFT+U}}{\partial n_l} = \epsilon_l^{DFT} + U\left(\frac{1}{2} - n_l\right). \tag{2.36}$$

Similarly, we can also find the orbital dependent correction to the Kohn-Sham potential ($V_l(\mathbf{r}) = \delta E/\delta n_l(\mathbf{r})$, where $n_l(\mathbf{r})$ is the electron density of l^{th} d-orbital) and this is given by

$$V_l^{DFT+U} = V_l^{DFT} + U\left(\frac{1}{2} - n_l\right). \tag{2.37}$$

The above expression clearly shows that the second term is repulsive for the occupation $n_l < 1/2$ and becomes attractive when $n_l > 1/2$. Thus, the Hubbard type correction introduces a discontinuity in the Kohn-Sham potential and orbital energies of the localized orbitals. This is one of the essential features of the exact DFT functional which was missing in standard DFT functionals such as LDA and GGA.

The expression for the DFT+U functional (2.35) can be generalized for the real solids having many d-orbitals atoms. In this work, we have used the simplified expression of rotationally invariant DFT+U functional introduced by Dudarev and coauthors [40]

$$E_{DFT+U}[n(\mathbf{r})] = E_{DFT}[n(\mathbf{r})] + \sum_I \frac{U^I}{2} Tr\left[\mathbf{n}^I(1 - \mathbf{n}^I)\right], \tag{2.38}$$

where $\mathbf{n}^I$ is generalized occupation matrix of d-orbitals, which is defined as the projection of Kohn-Sham states ψ_i on the localized orbitals ϕ_l (d- orbitals) of the atom at site I:

$$n_{l,l'}^I = \sum_i \langle \psi_i | \phi_l' \rangle \langle \phi_l | \psi_i \rangle. \tag{2.39}$$

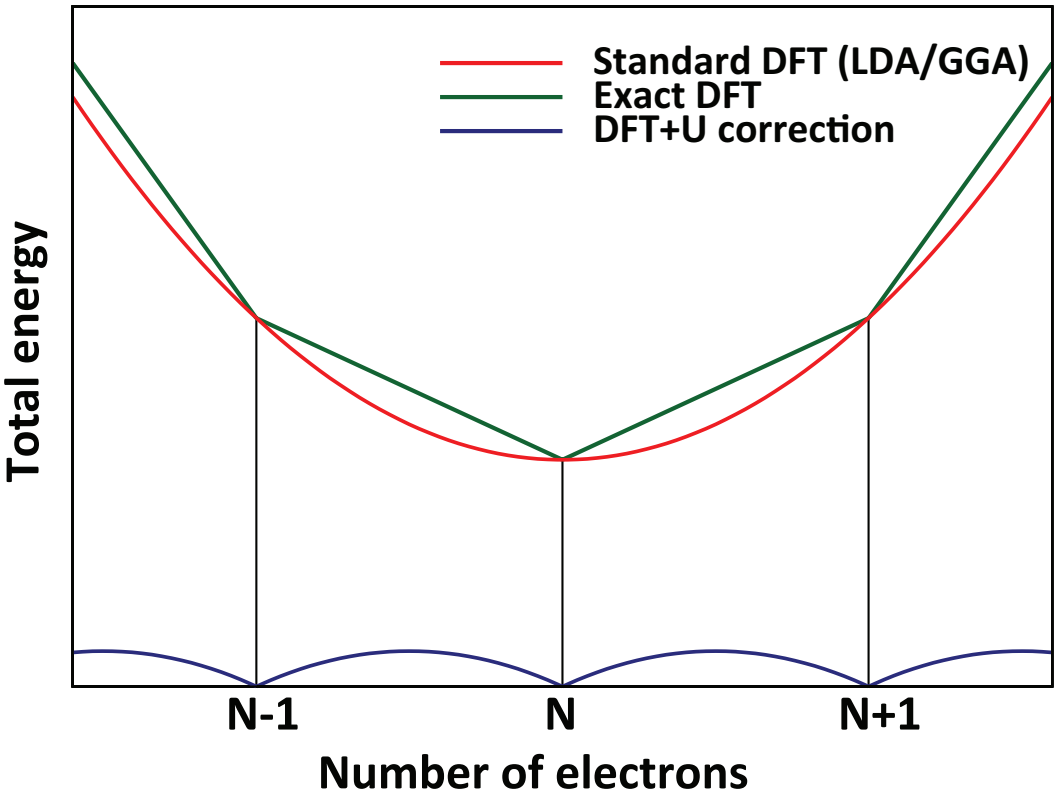

Figure 2.1: Schematic depiction of the total energy versus number of electrons in system. The red curve represents the calculation of total energy with the standard DFT (LDA or GGA) functional, the green line segments are for exact calculation based on the open quantum system description [39], and the blue curve is for the DFT+U correction to the standard DFT. The blue curve is the difference between exact and standard DFT calculation.

The parameter U^I represents the strength of electronic correlation of the localized states at site I. This parameter has been calculated self-consistently using the linear response approach developed by Cococcioni and coauthors [9, 10, 11]. In a representation of localized orbitals that diagonalizes the occupation matrices $\mathbf{n}^I$

$$n^I v_l^I = \lambda_l v_l^I, \tag{2.40}$$

where eigenvalue λ_l are considered by $0 \leq \lambda_l \leq 1$, the energy functional within DFT+U is

$$E_{DFT+U}[n(\mathbf{r})] = E_{DFT}[n(\mathbf{r})] + \sum_{I,l} \frac{U^I}{2} \lambda_l (1 - \lambda_l). \tag{2.41}$$

The Hubbard like correction term favors the fully occupied ($\lambda_l \sim 1$) or completely empty ($\lambda_l \sim 0$) localized orbitals and penalizes for the fractional occupation. Therefore, the Hubbard correction discourages the hybridization with neighboring atoms. The Hubbard type correction part of the energy functional is schematically shown by blue color curve in figure 2.1. In practical calculations for the real solids, the occupations of the localized orbitals evolve during the iterative process of self-consistent solution of Kohn-Sham equations, and eventually may lead to a state in which localized orbitals may not be completely empty or completely filled due to competition between kinetic energy and Hubbard type correction. This system can also be thought of as an open quantum system where an atom having localized states can exchange electrons with the reservoir (i.e., electrons from the surrounding atoms in the solid). In an open quantum system, however, only integer number of electrons can be exchanged from the pure quantum states. The exchange fractional number of electrons is described by the statistical or ensemble average of pure states with their respective probabilities. The system with $N + \omega$ electrons (where N is an integer and $0 \leq \omega \leq 1$) can be described with the pure state of N and $N + 1$ electrons [39] and its quantum state $|\Psi_{N+\omega}\rangle$ as

$$|\Psi_{N+\omega}\rangle = a|\Psi_N\rangle + b|\Psi_{N+1}\rangle. \tag{2.42}$$

Using normalization constrain $|a|^2 + |b|^2 = 1$ and $\langle \Psi_{N+\omega} | \hat{N}_{N+\omega} | \Psi_{N+\omega} \rangle = N + \omega$, it can be shown that probabilities for the states of N and $N+1$ electrons are $(1-\omega)$ and ω, respectively. Then, the total energy of this system is give by

$$E_{N+\omega} = (1-\omega)E_N + \omega E_{N+1}. \tag{2.43}$$

and total number of electrons are

$$N + \omega = (1-\omega)N + \omega(N+1). \tag{2.44}$$

Thus, the total energy curve for this system (eq. 2.43) consists of straight line segments, with the slopes $(E_{N+1} - E_N)$, joining at the integer occupations of the atomic orbitals. This energy curve itself is continuous but its derivative $\partial E_{N+\omega}/\partial N$ is discontinuous at integer values of N. The energy profile with standard DFT functionals (LDA or GGA), however, is an analytical function of occupations of the localized states N and misses the essential discontinuities at the integer values of N. The Schematic comparison of the energy curve form exact DFT (green color piecewise continuous function) and with standard DFT functionals (red color parabola type function) is shown in figure 2.1. The standard DFT calculations produces an unphysical curvature in the energy profile for fractional occupations.

The expression for the Hubbard type correction (i.e., blue curve in Fig. 2.1) needed to reproduce the exact calculation (green curve) can be obtained as the difference between exact (green curve) and standard DFT (curve red) calculation provided the unphysical curvature of the standard DFT calculation is equal to the magnitude of U. Essentially, this is what is being done in the expression 2.7, where the spurious curvature is removed by adding the term $\sum_{I,l} \frac{U^I}{2} \lambda_l (1 - \lambda_l)$.

Therefore, the computation of parameter U is reduced to proper estimation of the unphysical curvature of the energy profile from standard DFT functionals with respect

to the occupation of the localized states (i.e., calculation of $\partial^2 E_{DFT}/\partial {n^I}^2$). For practical calculation of the parameter U, the occupation of the localized states is varied by applying a small perturbation to the effective DFT potential (V^{DFT}) which only acts on the localized states of the atom at site I:

$$V^{pert} = V^{DFT} + \alpha^I \sum_l |\phi_l^I\rangle\langle\phi_l^I|, \tag{2.45}$$

where α^I is the amplitude of the perturbation and $|\phi_l^I\rangle$ represent the localized states. After applying a set of small enough perturbations, so that the linear response regime is maintained, Kohn-Sham equations are solved and α^I dependent ground state energy is obtained:

$$E[\alpha^I] = E^{DFT}(n_I) + \sum_I \alpha^I n^I. \tag{2.46}$$

Then, the second derivative of the energy is

$$\frac{\partial^2 E^{DFT}(n_I)}{\partial n_I^2} = -\frac{\partial \alpha^I}{\partial n^I}, \tag{2.47}$$

which can be directly calculated from the response matrix of the occupation with respect to perturbations

$$\chi_{IJ} = \frac{\partial n^I}{\partial \alpha^J}. \tag{2.48}$$

The energy curvature (i.e., second derivative) can be obtained from the inverse of the response matrix:

$$\frac{\partial^2 E^{DFT}(n_I)}{\partial n_I^2} = -[\chi^{-1}]_{II}. \tag{2.49}$$

However, this curvature also contains the contribution from orbitals re-hybridization when external perturbation is applied. The latter implies that there would also be a quadratic response to the energy, even if the perturbation is applied to a non-interacting

system, since the variation of occupation leads to re-hybridization of the localized orbitals with other degrees of freedom and changes the energy of the system. This contribution (i.e., due to re-hybridization) to the curvature is then subtracted from the second derivative of the total energy. The effective value of the parameter U is thus calculated from

$$U = [\chi_0^{-1} - \chi^{-1}]_{II}, \tag{2.50}$$

where χ_0 is the response function of 'non-interacting' system due to re-hybridization of the localized orbitals.

The response matrix χ and χ_0, in practice, are calculated using a supercell approach. For this purpose, a large enough supercell around the Hubbard atom is created so that it can completely accommodate the charge redistribution due to perturbation. Starting from the well relaxed structure, self-consistent solution of Kohn-sham equations for the unperturbed system (i.e., $\alpha = 0$) is obtained using standard DFT functionals. Then using these potentials and electronic wave functions, another set of self-consistent calculations are performed for the perturbed system where a set perturbing potentials α (the values of α should be small enough to maintain the linear response regime) are applied to every inequivalent Hubbard atoms. The response matrix χ_0 is obtained from the response to the occupations (i.e., $\partial n_I/\partial \alpha_J$) just after first iteration of the self-consistent cycle for each perturbations since the charge redistribution is not affected yet due to electron correlations. However, χ is calculated after the self-consistency is reached for the perturbed system.

2.8 Ionic forces and stress tensor for a periodic solid

Having briefly described the formalism for calculating the ground state properties of a system with fixed ionic positions, we now focus on the structural properties of the

system. Forces on the ions in a particular ionic configuration can be calculated as

$$F_I = -\frac{\partial E(\mathbf{R})}{\partial \mathbf{R}_I}, \tag{2.51}$$

where $E(\mathbf{R})$ is the ground state Kohn-Sham energy for this ionic configuration. Using Hellmann-Feynman theorem, which states that the derivative of total energy with respect to a parameter is equal to the expectation value of the derivative of Hamiltonian with respect to the same parameter, forces on the ions are simply computed as

$$F_I = -\sum_i \left\langle \psi_i \left| \frac{\partial \hat{H}(\mathbf{R})}{\partial \mathbf{R}_I} \right| \psi_i \right\rangle \tag{2.52}$$

Similarly to the Hellmann-Feynman theorem, Nielsen and Martin [41] proposed a theorem for calculating the stresses on a periodic solid. The stress tensor $\sigma_{ij} = \frac{\partial E(\mathbf{R})}{\partial \epsilon_{ij}}$, where ϵ_{ij} is the strain, has been computed using Nielsen and Martin's formulation [41].

2.9 Structure optimization

It was shown in section 2.1 that within the Born-Oppenheimer approximation, electronic and ionic degrees of freedom can be decoupled due to large mass difference. Hence, the dynamics of ions under the influence of Born-Oppenheimer potential energy surface $E(\mathbf{R})$ (i.e., ground state energy of the interacting electrons for a fixed ionic configuration) is described by Schrödinger equation 2.5. Due to the large mass difference ($m_e << M_I$), the kinetic energy for ions would be very small compared to that for electrons, and ionic motion can be studied within the classical formalism. The classical Lagrangian describing the ionic motion is given by

$$L = \sum_I \frac{1}{2} M_I \dot{R}_I^2 - E(\mathbf{R}), \tag{2.53}$$

where M_I is the ionic mass, and $E(\mathbf{R})$ is the Kohn-Sham (KS) ground state energy. The dynamics governed by this Lagrangian (eq. 2.53) is called *ab initio* molecular dynamics

(MD) since the KS energy $E(\mathbf{R})$ for every MD time step is obtained from the first-principles calculation.

In order to obtain the equilibrium structure at any arbitrary pressure, Parrinello and Rahman [42, 43] generalized the above Lagrangian (eq. 2.53) by including the lattice degrees of freedom:

$$L = \sum_I \frac{1}{2} M_I (\dot{S}_I^T g \dot{S}_I) - E(S_I) + \frac{1}{2} W [Tr(\dot{h}^T \dot{h})] - PV, \tag{2.54}$$

where h is the matrix formed by time dependent lattice vectors [**a**,**b**,**c**], S_I are the rescaled ionic coordinates defined as $R_I = hS_I$, g is given by $g = h^T h$, W is fictitious lattice weight, and V is the cell volume. However, this Lagrangian is not invariant for the choice of lattice vectors of the crystal. Wentzcovitch and coauthors [13, 14] introduced further developments by using the strains ϵ_{ij} as time dependent variables. Rescaling the ionic coordinates as $R_I = (1+\epsilon) q_I$, they proposed the following Lagrangian

$$L_W = \sum_I \frac{1}{2} M_I [\dot{q}_I^T g(\epsilon) \dot{q}_I] - E(q_I, \epsilon) + \frac{1}{2} W [Tr(\dot{\epsilon} \dot{\epsilon}^T)] - PV(\epsilon), \tag{2.55}$$

where g is now given by $g(\epsilon) = (1+\epsilon)^T (1+\epsilon)$. The relationship between matrix h and ϵ is $h = (1+\epsilon) h_0$, where the matrix h_0 corresponds to the initial state of lattice vectors. The fictitious mass W is chosen to optimize the dynamics of ions and lattice with similar frequencies. The equilibrium structure of the system (ions and lattice parameters) at pressure P is obtained by minimizing the enthalpy H along the trajectories generated by the equations of motion of Lagrangian (eq. 2.55).

2.10 Birch-Murnaghan equation of state

The thermodynamic state of matter is described by a mathematical relationship (usually called the equation of state or EoS) among the pressure P, temperature T, and volume

V or density ρ. The simplest form of the isothermal EOS for solids [44] is given by

$$K = -\frac{dP}{dlnV} = -\frac{dP}{dln\rho}, \tag{2.56}$$

where K is the bulk modulus of the system. This EoS is not correct at high pressures because it does not take into account the fact that the bulk modulus increases significantly with increasing pressure (i.e., larger the pressure, more difficult to compress the solid).

The most relevant equation of states for solids at high pressure (i.e., Earth's lower mantle minerals) are described in terms of finite strain. The Helmholtz free-energy of the solid in terms of finite strain f is expressed as

$$F(T,V) = a(T)f^2 + b(T)f^3 + c(T)f^4..... \tag{2.57}$$

where the 'compression' f is defined as

$$f = \frac{1}{2}\left[\left(\frac{V_0}{V}\right)^{2/3} - 1\right]. \tag{2.58}$$

- **Second order Birch-Murnaghan's equation of state**

  The free-energy F up to second-order is

  $$F(T,V) \approx a(T)f^2. \tag{2.59}$$

  Then the isothermal equation of state in terms of zero-pressure bulk modulus K_0 is given by

  $$P = 3K_0 f(1+2f)^{5/2} = \frac{3K_0}{2}\left[\left(\frac{V_0}{V}\right)^{7/3} - \left(\frac{V_0}{V}\right)^{5/3}\right]. \tag{2.60}$$

- **Third order Birch-Murnaghan's equation of state**

  Similarly to the previous case, now writing F as

  $$F(T,V) \approx a(T)f^2 + b(T)f^3, \tag{2.61}$$

the equation of state is

$$P = \frac{3K_0}{2}\left[\left(\frac{V_0}{V}\right)^{7/3} - \left(\frac{V_0}{V}\right)^{5/3}\right]\left\{1 + \frac{3}{4}(K_0^{'} - 4)\left[\left(\frac{V_0}{V}\right)^{2/3} - 1\right]\right\}, \quad (2.62)$$

where $K_0^{'}$ is pressure derivative of bulk modulus K_0.

2.11 Static elasticity

The response to a finite stress (σ_{ij}) or strain (ϵ_{ij}) of an elastic solid within the linear regime is expressed by constitutive relation:

$$\sigma_{ij} = \sum_{k,l} C_{ijkl}\epsilon_{kl} \quad or \quad \epsilon_{ij} = \sum_{k,l} S_{ijkl}\sigma_{kl}$$

where C_{ijkl} and S_{ijkl} are the fourth-order symmetric *elastic* and *compliance tensor*, respectively. Owing to the fact that stress (σ_{ij}) and strain (ϵ_{ij}) tensors are symmetric, there will be only 21 non-zero independent components in the elastic tensor. The number of non-zero independent components further decreases as the symmetry of the considered crystal increases. For convenience, these elastic constants are also expressed in contracted notation (called *Voigt notation*), where a pair of indices is replaced by one index in the following way:

$$11 \rightarrow 1, 22 \rightarrow 2, 33 \rightarrow 3, 23 = 32 \rightarrow 4, 13 = 31 \rightarrow 5, 12 = 21 \rightarrow 6.$$

In this thesis, we have studied the thermoelasticity of Fe- and Al-bearing $MgSiO_3$ perovskite, which is an orthorhombic crystal structure. Thus, there are 9 non-zero independent elastic constants (namely $C_{11}, C_{22}, C_{33}, C_{12}, C_{13}, C_{23}, C_{44}, C_{55}$, and C_{66}) for this system. In practice, a set of small strains (small enough to maintain the linear regime) are applied to the equilibrium structure and resulting stresses are utilized to obtain elastic constants C_{ij}.

2.11.1 Aggregate elastic moduli and acoustic velocities

The isotropic elastic moduli for a polycrystalline system are determined by averaging the single crystal elastic constants (C_{ij}) or compliances (S_{ij}) over all lattice orientations under appropriate assumption. In general, the exact distribution and orientation of single crystals in a polycrystalline sample are unknown and the best that can be done is to estimate the upper and lower bounds of elastic moduli. In this work, we have used the *Voigt-Reuss-Hill* (VRH) averaging scheme [45] to estimate aggregate bulk (K) and shear modulus. (G). In Voigt average scheme, it is assumed that the strain is uniform throughout a polycrystalline sample and the 'upper bound' of elastic moduli is given by

$$K_V = \frac{1}{9}\left[(C_{11}+C_{22}+C_{33})+2(C_{12}+C_{23}+C_{13})\right], \tag{2.63}$$

$$G_V = \frac{1}{15}\left[(C_{11}+C_{22}+C_{33})-(C_{12}+C_{23}+C_{13})+3(C_{44}+C_{55}+C_{66})\right]. \tag{2.64}$$

Similarly, the Reuss averages are obtained assuming the uniform stress in throughout a polycrystalline sample and the 'lower bound' of elastic moduli are

$$\frac{1}{K_R} = \left[(S_{11}+S_{22}+S_{33})+2(S_{12}+S_{23}+S_{13})\right], \tag{2.65}$$

$$\frac{15}{G_R} = \left[4(S_{11}+S_{22}+S_{33})-4(S_{12}+S_{23}+S_{13})+3(S_{44}+S_{55}+S_{66})\right], \tag{2.66}$$

where compliances S_{ij} are determined by inverting the elastic constant matrix C_{ij} (i.e., $\mathbf{S}=\mathbf{C}^{-1}$). The VRH averages are simply the arithmetic mean of the upper and lower bounds of the elastic moduli:

$$K_{VRH} = \frac{K_V + K_R}{2}, \tag{2.67}$$

$$G_{VRH} = \frac{G_V + G_R}{2}. \tag{2.68}$$

These VRH averages, although approximate, provide a very good estimate of aggregate elastic moduli of the Earth's lower mantle minerals.

Having obtained the aggregate bulk and shear modulus, isotropic average compressional (V_P), shear (V_S), and bulk (V_Φ) velocities are determined by

$$V_P = \sqrt{\frac{K + \frac{4}{3}G}{\rho}}, \qquad V_S = \sqrt{\frac{G}{\rho}}, \qquad V_\Phi = \sqrt{\frac{K}{\rho}}, \tag{2.69}$$

where ρ is the density.

2.12 Phonon calculations using density functional perturbation theory

The vibrational frequencies of the system are determined by the eigenvalues of the Hessian [121]:

$$det \left| \frac{1}{\sqrt{M_I M_J}} \frac{\partial^2 E(\mathbf{R})}{\partial \mathbf{R}_I \partial \mathbf{R}_J} - \omega^2 \right| = 0, \tag{2.70}$$

where $E(\mathbf{R})$ is again the Born-Oppenheimer potential energy surface for a fixed ionic configuration, whose Hamiltonian is rewritten from eq. 2.4

$$\hat{H}_{BO} = -\frac{\hbar^2}{2m_e} \sum_i \nabla_i^2 + \frac{1}{2} \sum_{i \neq j} \frac{e^2}{|\mathbf{r}_i - \mathbf{r}_j|} + V_{ext}(\mathbf{r}) + E_N(\mathbf{R}), \tag{2.71}$$

with the electron-iron interaction $V_{ext}(\mathbf{r}) = \sum_{i,\alpha} \frac{Z_\alpha e^2}{|\mathbf{r}_i - \mathbf{R}_\alpha|}$ and the ion-ion interaction $E_N(\mathbf{R}) = \frac{1}{2} \sum_{\alpha \neq \beta} \frac{Z_\alpha Z_\beta e^2}{|\mathbf{R}_\alpha - \mathbf{R}_\beta|}$. Using Hellmann-Feynman theorem (eq. 2.52), the Hessian of $E(\mathbf{R})$ is obtained by differentiating the forces on the ions:

$$\begin{aligned} \frac{\partial^2 E(\mathbf{R})}{\partial \mathbf{R}_I \partial \mathbf{R}_J} &\equiv -\frac{\partial F_I}{\partial \mathbf{R}_J} \\ &= \int \frac{\partial n(\mathbf{r})}{\partial \mathbf{R}_J} \frac{\partial V_{ext}(\mathbf{r})}{\partial \mathbf{R}_I} d\mathbf{r} + \int n(\mathbf{r}) \frac{\partial^2 V_{ext}(\mathbf{r})}{\partial \mathbf{R}_I \partial \mathbf{R}_J} d\mathbf{r} + \frac{\partial^2 E_N(\mathbf{R})}{\partial \mathbf{R}_I \partial \mathbf{R}_J}. \end{aligned} \tag{2.72}$$

So the calculation of the Hessian of $E(\mathbf{R})$ requires the ground state electron density $n(\mathbf{r})$ and its linear response to the ionic distortion, i.e., $\frac{\partial n(\mathbf{r})}{\partial \mathbf{R}_I}$ [121, 46, 47]. For computational convenience, this Hessian matrix for a crystal can also be expressed as

$$C_{s,s'}^{\alpha,\alpha'}(\mathbf{R} - \mathbf{R}') = \frac{\partial^2 E(\mathbf{R})}{\partial u_s^\alpha(\mathbf{R}) \partial u_{s'}^{\alpha'}()\mathbf{R}}, \tag{2.73}$$

where $u_s^{\alpha}(\mathbf{R})$ is α^{th} component of the s^{th} ion displacement located at lattice site $\mathbf{R}$. The coefficients $C_{s,s'}^{\alpha,\alpha'}(\mathbf{R}-\mathbf{R}')$ are also called the 'inter-atomic-force constants' (IFC).

The linear response of density to ionic distortion $\left(\frac{\partial n(\mathbf{r})}{\partial \mathbf{R}_I}\right)$ is determined using 'density functional perturbation theory' (DFPT). The derivative of the electron density $n(\mathbf{r})$ (eq. 2.9) with respect to the parameter $\mathbf{R}_I$ is

$$n'(\mathbf{r}) = 2Re\left(\sum_i^N \psi_i^* \psi_i^{'}\right). \tag{2.74}$$

Since the potential $V_{ext}(\mathbf{r})$ is real, the Kohn-Sham wave functions ψ_i are also real. The derivative of ψ_i can be determined using standard first-order perturbation theory which leads to:

$$\left(H_{KS}^0 - \epsilon_i^0\right)|\psi_i^{'}\rangle = -\left(V_{KS}^{'} - \epsilon_i^{'}\right)|\psi_i^0\rangle, \tag{2.75}$$

where H_{KS}^0 is the unperturbed Kohn-Sham Hamiltonian (eq. 2.18) with the potential given by eq. 2.15, $V_{KS}^{'}$ is the first-order correction to the Kohn-Sham potential

$$V_{KS}^{'} = V_{ext}^{'} + \left(e^2 \int d\mathbf{r}' \frac{n'(\mathbf{r})}{|\mathbf{r}-\mathbf{r}'|}\right) + \left[\frac{\partial}{\partial n}\left(\frac{\delta E_{xc}}{\delta n}\right)\right]_{n(\mathbf{r})} n(\mathbf{r}^{'}), \tag{2.76}$$

and the first-order correction to Kohn-Sham eigenvalue ϵ_i is given by $\epsilon_i^{'} = \langle\psi_i^0|V_{KS}^{'}|\psi_i^0\rangle$. Equations (2.74),(2.75), and (2.76) form the set of self-consistent equations similar to Kohn-Sham equations (2.9, 2.15, and 2.18).

The direct computation of IFC matrx (2.73) is not convenient in practical calculations because any localized perturbation (i.e., ionic displacement) would break the translational symmetry of the system and would require computationally expensive large super-cell. However, in the Fourier space, the IFC matrix (eq. 2.73) can be written as

$$C_{s,s'}^{\alpha,\alpha'}(\mathbf{q}) = \sum_R C_{s,s'}^{\alpha,\alpha'}(\mathbf{R}) \exp(-i\mathbf{q}.\mathbf{R}). \tag{2.77}$$

Then, the vibration frequencies $[\omega(\mathbf{q},\nu)]^2$ of the system having n atoms in the unit-cell are the eigenvalues of the $3n\times3n$ 'dynamical matrix'

$$D^{\alpha,\alpha'}_{s,s'}(\mathbf{q}) = \frac{1}{\sqrt{M_s M_{s'}}} C^{\alpha,\alpha'}_{s,s'}(\mathbf{q}), \tag{2.78}$$

where ν represent the vibrational modes of the system. Thus, the numerical computations of IFC is more convenient in the Fourier space where one can directly obtain the $\mathbf{q}$-dependent dynamical matrices. In order to obtain the vibrational density of states (VDOS) of the system, IFC are calculated in an appropriate $\mathbf{q}$-vectors grid of the unit-cell and are transformed to 'real-space' IFC matrices using *Fast-Fourier Transform* (FFT) techniques. Then, the IFC matrices are interpolated in a much denser $\mathbf{q}$-vectors grid again using FFT techniques.

2.13 Thermodynamic and thermoelastic properties within quasi-harmonic approximation

The temperature dependence of the low-temperature heat capacity ($C_V \propto T^3$) is well described in terms of a statistical ensemble of quantum mechanical harmonic oscillators (Debye model). The success of the Debye model depends on the fact that at low temperatures, amplitudes of atomic vibrations are much smaller than inter-atomic distances. Thus the energy of these vibrations can be approximated to the quadratic dependence of amplitudes (harmonic approximation). In the harmonic approximation (HA), vibrational frequencies are assumed to be independent of inter-atomic distance. However, this approximation (HA) is too simple for a proper description of solids at high pressures. Further improvements can be made by considering the volume dependence of vibrational frequencies (quasiharmonic approximation).

Thermodynamic and thermoelastic properties of solids below the melting temperature are quite well described within the quasiharmonic approximation (QHA). The

Helmholtz free-energy of the crystal within the QHA is given by

$$F(T,V,\alpha) = U_{st}(V,\alpha) + \frac{1}{2}\sum_{\mathbf{q},\nu}\hbar\omega(\mathbf{q},\nu,\alpha) + k_BT\sum_{\mathbf{q},\nu}\ln\left\{1-\exp\left(-\frac{\hbar\omega(\mathbf{q},\nu,\alpha)}{k_BT}\right)\right\}, \quad (2.79)$$

where $U_{st}(V,\alpha)$ is the static (zero temperature) internal energy calculated from standard DFT/DFT+U methods, $\mathbf{q}$ represents the phonon wave vector and ν is the vibrational mode index. Here α represents any constraint other than the volume V on which vibrational frequencies $\omega(\mathbf{q},\nu,\alpha)$ and static internal energy may depend. $\hbar$ and k_B are the Planck and Boltzmann constants, respectively. In practical calculations, equilibrium volume, static internal energy, and vibrational frequencies of a crystal are calculated at 12-15 pressure points within the desired pressure-range and then the Helmholtz free-energy F is calculated at these pressure points. Thus, calculated Helmholtz free-energies are fitted with an appropriate Birch-Murnaghan (BM) equation of state. Having obtained the good fit for the Helmholtz free-energy, all the thermodynamic properties of the system are calculated using standard thermodynamic relations.

2.13.1 A semi-analytical method for thermoelastic properties at high pressures and temperatures

The Helmholtz free-energy for a strained solid crystal is obtained by substituting an infinitesimal strain ϵ for α in equation 2.79:

$$F(T,V,\epsilon) = U_{st}(V,\epsilon) + \frac{1}{2}\sum_{\mathbf{q},\nu}\hbar\omega(\mathbf{q},\nu,\epsilon) + k_BT\sum_{\mathbf{q},\nu}\ln\left\{1-\exp\left(-\frac{\hbar\omega(\mathbf{q},\nu,\epsilon)}{k_BT}\right)\right\}. \quad (2.80)$$

The isotropic pressure

$$P = -\left(\frac{\partial F}{\partial V}\right)_T \quad (2.81)$$

and the Gibb's free-energy

$$G(T,P,\epsilon) = F(T,V) + PV \quad (2.82)$$

for the strained system can be calculated using equation 2.80.

The isothermal elastic constants C^T_{ijkl} are given by

$$C^T_{ijkl}(T,P) = \left[\frac{1}{V}\frac{\partial^2 G(T,P,\epsilon)}{\partial\epsilon_{ij}\partial\epsilon_{kl}}\right]_{T,P}, \tag{2.83}$$

where the indices $i,j,k,l = 1,2,3$. Then, the adiabatic elastic constants C^S_{ijkl} can be obtained as

$$C^S_{ijkl}(T,P) = C^T_{ijkl}(T,P) + \frac{T}{VC_V}\frac{\partial S}{\partial\epsilon_{ij}}\frac{\partial S}{\partial\epsilon_{kl}}\delta_{ij}\delta_{kl}, \tag{2.84}$$

where the entropy S, and the heat capacity at constant volume C_V are also calculated from the free-energy $F(T,V,\epsilon)$ (eq. 2.80). It is evident from the equation 2.83 that the computation of thermal elastic constants requires the calculation of the Gibb's free-energy, $G(T,P,\epsilon)$, for several strained configurations (number of these strained configurations depends on the crystal symmetry). However, the computation of the vibrational density of states (VDOS) using density functional perturbation theory (DFPT) for free-energy calculation (eq. 2.80) is usually computationally expensive, especially for large and less symmetric supercells, which are used very often to investigate materials with impurities such as Fe- and Al-bearing minerals. Thus, the computation of high pressures and high temperatures elasticity becomes exceedingly demanding (∼1000 parallel jobs each running on tens or more processors).

Owing to the above mentioned difficulty, Wu and Wentzcovitch [51] developed a more efficient semi-analytical method for elasticity calculation, which requires the calculation of VDOS only for the unstrained configurations. In this method, the isothermal elastic constants C^T_{ijkl} are expressed in terms of the *strain Grüneisen parameters* $\gamma^{ij}_{\mathbf{q},m}$ which are defined as

$$\frac{\partial\omega(\mathbf{q},\nu)}{\omega(\mathbf{q},\nu)} = -\gamma^{ij}_{\mathbf{q},m}\epsilon_{ij}. \tag{2.85}$$

Then, assuming that the angular distribution of $\gamma^{ij}_{\mathbf{q},m}$ is isotropic, the elastic constants C^T_{ijkl} can be obtained in terms of the *volume Grüneisen parameters* $\gamma_{\mathbf{q},m}$ which are defined as

$$\frac{d\omega(\mathbf{q},\nu)}{\omega(\mathbf{q},\nu} = -\gamma_{\mathbf{q},m}\frac{dV}{V}. \tag{2.86}$$

Since the calculation of $\gamma_{\mathbf{q},m}$ only requires the change in vibrational frequencies with respect to volume, the thermal elastic constants can be calculated using static elastic constants and VDOS for the unstrained equilibrium structures at 12-15 pressure points within the desired pressure-range. The approximation that $\gamma^{ij}_{\mathbf{q},m}$ have isotropic angular distribution is equivalent to assume that the thermal pressure is isotropic. In spite of this approximation, this method often provides more precise elastic constants than the traditional method proposed by Karki and coauthors [48, 50], because the error associated with this approximation is typically smaller than the numerical error introduced by calculations of VDOS, free-energy and its derivative for the strained configurations.

Chapter 3

Spin crossovers in iron-bearing $MgSiO_3$ and $MgGeO_3$: their influence on the post-perovskite transition

In this chapter, we present *ab initio* study of the pressure induced iron state changes in perovskite and post-perovskite structure of Fe-bearing $MgGeO_3$ and $MgSiO_3$. $MgGeO_3$-perovskite is known to be a low-pressure analog of $MgSiO_3$-perovskite in many respects, but especially in regard to the post-perovskite transition. As such, investigation of spin state changes in Fe-bearing $MgGeO_3$ might help to clarify some aspects of this type of state change in Fe-bearing $MgSiO_3$. Using DFT+U calculations, we have investigated pressure induced spin state changes in Fe^{2+} and Fe^{3+} in $MgGeO_3$ perovskite and post-perovskite. Owing to the larger ionic radius of germanium compared to silicon,

germanate phases have larger unit cell volume and inter-atomic distances than equivalent silicate phases at same pressures. As a result, all pressure induced state changes in iron occur at higher pressures in germanate phases than in the silicate ones, be it a spin state change or position change of (ferrous) iron in the perovskite A site. We showed that iron state transitions occur at particular average Fe-O bond-length (i.e., $\sim$2.22(1) $\mathring{A}$ and $\sim$1.86(1) $\mathring{A}$ for Fe^{2+} and Fe^{3+} substitutions, respectively) irrespective of mineral composition (silicate or germanate) or exchange correlation functionals used in the calculation (LDA+U_{sc} or GGA+U_{sc}). Ferrous iron substitution decreases the perovskite to post-perovskite (PPv) transition pressure while coupled ferric iron substitution increases it noticeably.

3.1 Introduction

Iron-bearing $MgSiO_3$ perovskite (Si-Pv), also known as bridgmanite, is one of the major constituent minerals of Earth's lower mantle along with (Mg,Fe)O ferropericlase (Fp). Unraveling the composition and thermal structure of the lower mantle requires a detailed understanding of the influence of iron (Fe) on these host minerals. It is well known that iron in (Mg,Fe)O undergoes a pressure induced spin crossover from high-spin (S=2) to low-spin (S=0) state and affects elastic properties [52, 53, 55, 56, 57, 58, 59, 60, 61]. In the case of Si-Pv, deciphering the iron spin state has been quite challenging due to complex perovskite structure and possibility of different valence states of iron (ferric and ferrous) [3, 63, 64, 66, 68, 70, 71, 72, 73, 74, 75, 76]. Si-Pv is also known to undergo a perovskite (Pv) to post-perovskite (PPv) phase transition in the pressure range $\sim$ 107–125 GPa and this will have geophysical consequences in deep lower mantle region [54, 84, 92, 99]. Understanding the effect of iron, especially, on Pv to PPv transition and on elastic properties of Pv and PPv phases is crucial to constrain lower mantle composition.

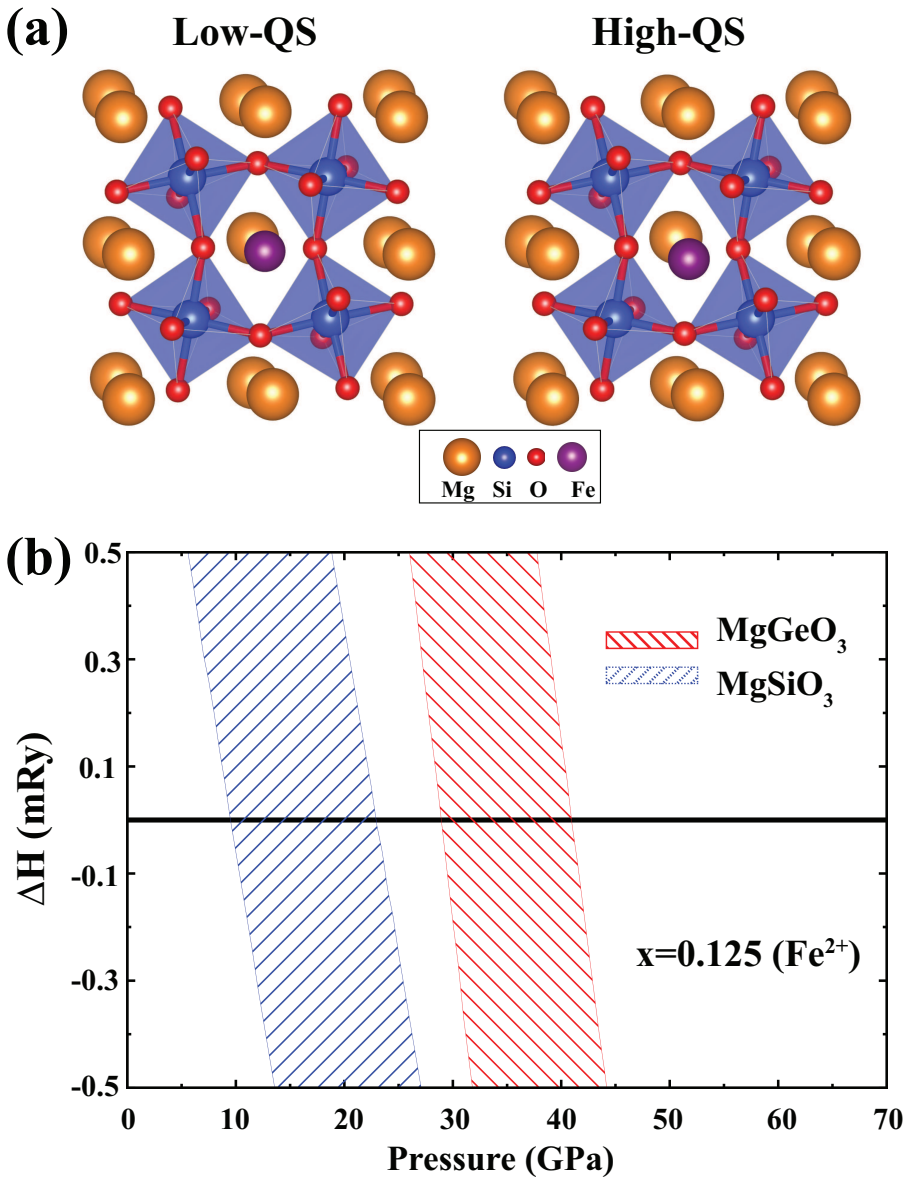

Figure 3.1: (a) Atomic structure around low-QS and high-QS Fe^{2+}-bearing $MgSiO_3$ in Pv phase at ambient pressure. Fe, Mg, O, and Si are represented as purple, orange, red, and blue sphere, respectively. $MgGeO_3$-Pv structures are similar and not shown here. (b) Enthalpy difference ($\Delta H = H_{high-QS} - H_{low-QS}$) for Fe^{2+}-bearing Si-Pv (blue) and Ge-Pv (red). Lower and upper bounds correspond to LDA+U_{sc} and GGA+U_{sc} results, respectively.

In (Mg,Fe^{2+})SiO_3-Pv, the pressure induced increase in Mössbauer quadrupole splitting (QS) above ∼30 GPa (low-QS to high-QS transition) [3, 64, 66, 68, 76, 77, 78] has been explained by lateral displacement of Fe^{2+} ion which remains in the high-spin (HS) state in the entire lower-mantle pressure range [60, 72, 74, 79]. In the case of (Mg,Fe^{3+})(Si,Fe^{3+})O_3-Pv, however, first-principles calculations by *Hsu et al., 2011* [75] reported that Fe^{3+} in B-site undergoes a high-spin (S=5/2) to low-spin (S=1/2) state change at approximately 41 GPa and 70 GPa using LDA+U_{sc} and GGA+U_{sc} methods, respectively, while in the A-site Fe^{3+} remains in the high-spin state. These findings for Fe^{3+} substitution were in good agreement with experimental observations of *Catalli et al., 2010* [81]. There have also been several experimental [71, 82, 83] and first-principles studies [85, 86, 87] about the spin crossover in $MgSiO_3$-PPv (Si-PPv). The consensus regarding the spin crossover in iron-bearing Si-PPv is that Fe^{2+} in the A-site remains in the high-spin and high-QS state throughout the lower mantle pressure range, while Fe^{3+} undergoes a high to low spin transition in the B site and remains in the high spin state in the A-site [87]. In spite of these efforts to pin down the state of iron at high pressures, it has been very difficult to ascertain the exact role of iron with its varying spin and valence state on Pv to PPv transition, especially because of the extreme pressure and temperature conditions in the deep lower mantle region.

$MgGeO_3$-perovskite (Ge-Pv) is a low pressure analog of $MgSiO_3$ perovskite [89, 90, 91, 93, 94, 95, 96, 97, 98, 100] and would be a promising candidate to investigate iron spin crossover and its structural influence on $MgSiO_3$-Pv and PPv phases. In this study, we have used first-principles DFT+U (LDA+U_{sc} and GGA+U_{sc}) calculations to investigate the iron spin states and their crossover in the Pv and PPv phases of Fe^{2+}- and Fe^{3+}-bearing $MgGeO_3$. Comparing enthalpy of the different spin states, we have determined the stability of the different states and transition pressure. Using these results, we have also investigated the effect of Fe^{2+} and Fe^{3+} substitution on Pv to PPv

transition.

3.2 Method

We have used density functional theory (DFT) within the local density approximation (LDA) [18] and generalized gradient approximation (GGA) [19]. It is well known that 3d and 4f electrons are not adequately described by standard DFT functionals due to strong correlation effects. To cope with these insufficiencies, the DFT method is augmented by the self- and structurally consist Hubbard U_{sc} (LDA/GGA+U_{sc}) [10, 11, 75, 12]. Ultrasoft pseudo-potentials, generated by Vanderbilt's method [28], have been used for Fe, Si, Ge, and O. For Mg, norm-conserving pseudo-potential generated by von Barth-Car's method, has been used. The plane-wave kinetic energy and charge density cutoff are 50 Ry and 300 Ry, respectively. Self-consistent U_{sc}, calculated by *Hsu et al., 2010, 2011* [74, 75] and *Yu et al., 2012* [87] using the linear response approach [10, 11] (Table 3.1), have been used. All calculations were performed in a 40-atoms super-cell. Electronic states were sampled on a shifted $2\times2\times2$ and $3\times2\times3$ k-point grid for Pv and PPv structure, respectively [20]. Structural optimization at any arbitrary pressure has been performed using variable cell-shape damped molecular dynamics approach [13, 14]. Structures are optimized until the inter-atomic forces are smaller than 10^{-4} $Ry/a.u.$ For every possible spin and valence state, structures are optimized at twelve volumes in the relevant pressure-range and the 3^{rd}-order Birch-Murngharn equation of state has been used to fit these compression data.

Table 3.1: Self-consistent Hubbard U_{sc}(eV) for ferrous and ferric iron calculated by *Hsu et al., 2010, 2011* [74, 75] in Si-Pv, and by *Yu et al., 2012* [87] in Si-PPv structures.

	Fe^{2+}		Fe^{3+}		
	High-QS	Low-QS	A(HS)	B(HS)	B(LS)
Pv	3.1	3.1	3.7	3.3	4.9
PPv	2.9	–	4.0	3.5	5.6

3.3 Iron spin states in Pv and PPv phases

Iron spin states have been investigated in Fe^{2+} and Fe^{3+}-bearing $MgGeO_3$ and $MgSiO_3$ in a 40-atom super-cell. One Fe^{2+} ion is substituted for a Mg^{2+} ion in the A-site in $(Mg_{0.875}Fe_{0.125})GeO_3$ and $(Mg_{0.875}Fe_{0.125})SiO_3$ while two Fe^{3+}'s are substituted for one Mg^{2+} and one first neighbor Ge^{4+} or Si^{4+} as in $(Mg_{0.875}Fe_{0.125})(Ge_{0.875}Fe_{0.125})O_3$ and $(Mg_{0.875}Fe_{0.125})(Si_{0.875}Fe_{0.125})O_3$. The nearest-neighbor Fe^{3+}-Fe^{3+} substitution has been chosen as it has been found to be the lowest energy configuration in previous first-principles studies [75, 87, 88]. The issue of site occupancy and valence states of iron in $MgSiO_3$ is still much debated experimentally [76, 101, 102]. For example, *Lin et al., 2012* [76] propose that 50% of Fe^{3+} is substituted through charge-coupled substitution in Mg and Si site while remaining 50% Fe^{3+} goes in the Si site through oxygen vacancy. *Hummer et al., 2012* [101] suggest that the ratio of Fe^{3+} in Mg and Si sites depends on total iron concentration. *Sinmyo et al., 2014* [102] concluded that all Fe^{3+} would be in Mg site. Our goal in this study is to estimate the transition pressures for iron state changes in $MgGeO_3$ as compared to $MgSiO_3$, for this we have chosen a well studied charge-coupled Fe^{3+}-Fe^{3+} substitution. Relative enthalpies have been used to calculate transition pressures (P_t) and the stability of a state or phase in a given pressure range. Effects of disorder have not been addressed at this point, but it is expected to produce a two-phase loop. Here we wish to analyze (a) the potentially different effects of Fe^{2+} and Fe^{3+} in the Pv to PPv transition and (b) whether the germanate phase could serve as a good low pressure analog to investigate spin transitions in iron.

Table 3.2: Spin state transition pressures, P_t(GPa), in iron-bearing $MgGeO_3$ and $MgSiO_3$ calculated within LDA+U_{sc} and GGA+U_{sc} methods.

	Low-QS to High-QS in Fe^{2+}-bearing Pv phase		B(HS) to B(LS) in Fe^{3+}-bearing Pv and PPv phases			
			Pv		PPv	
	LDA+U_{sc}	GGA+U_{sc}	LDA+U_{sc}	GGA+U_{sc}	LDA+U_{sc}	GGA+U_{sc}
$MgGeO_3$	28.5	40.5	56.5	85.0	49.5	82.5
$MgSiO_3$	9.5	22.5	41.0	69.5	28.0	59.5

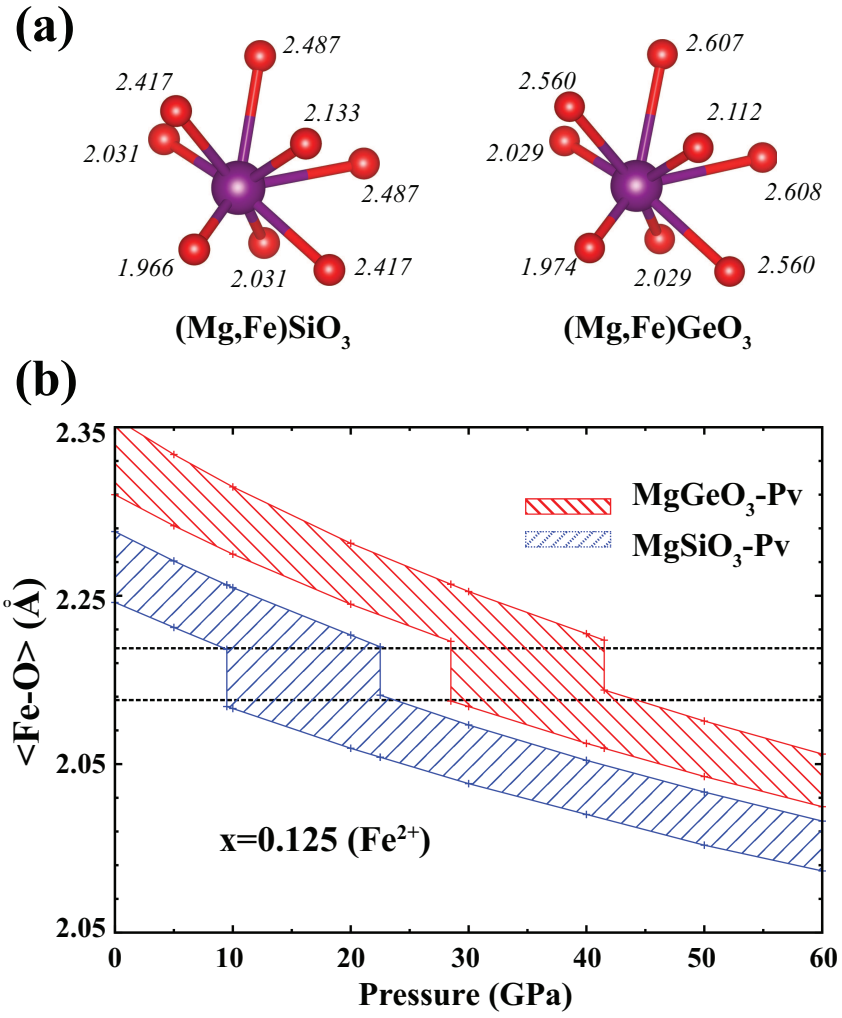

Figure 3.2: Atomic environment around iron in Fe^{2+}-bearing Si-Pv and Ge-Pv phases. (a) Fe-O distances (in $\AA$) in Si-Pv, and Ge-Pv structures at ambient pressure are shown next to the oxygen atoms. (b) Pressure dependence of average Fe-O distance. Vertical lines represent the low-QS to high-QS transition. Lower and upper bounds correspond to LDA+U_{sc} and GGA+U_{sc} results, respectively.

3.3.1 Spin states of Fe^{2+} in Ge-Pv and Si-Pv

As in the case of Fe^{2+}in Si-Pv [60, 72, 74], Fe^{2+} in Ge-Pv remains in the high-spin (HS, S=2) state in the entire lower-mantle pressure range (0-135 GPa). However, it undergoes a pressure induced lateral displacement producing a transition from low to high Mössbauer quadrupole splitting (QS). The atomic structures for the low- and high-QS states of iron in Si-Pv are shown in Fig. 3.1(a) (similar structures are for Ge-Pv which are not shown here) indicating the lateral displacement of iron in the perovskite A-site. The pressure dependence of enthalpy differences between high-QS and low-QS states (ΔH=$H_{high-QS}$-H_{low-QS}) gives the low- to high-QS transition pressure. It is well-known that LDA usually underestimates transition pressures while GGA usually overestimates it. In this study, we present both LDA+U_{sc} and GGA+U_{sc} results to provide lower and upper bounds for this transition, as shown in Fig. 3.1(b). The low- to high-QS state change in Ge-Pv occurs at ∼28.5 GPa with LDA+U_{sc} and at ∼40.5 GPa with GGA+U_{sc}. These low- to high-QS transition pressures in Ge-Pv are quite large compared to those in Si-Pv, i.e., ∼9.5 GPa and ∼22.5 GPa, respectively, as shown in Table 3.2. Owing to the larger ionic radius of Ge^{4+} (0.53 $\AA$) compared to that of Si^{4+} (0.40 $\AA$), the unit-cell volume and inter-atomic distances in Ge-Pv are larger than in Si-Pv. Zero pressure Fe-O bond-lengths in Si-Pv and Ge-Pv obtained with LDA+U_{sc} are shown Fig. 3.2(a). The average of Fe-O bond-lengths, ⟨Fe-O⟩, is also shown in Fig. 3.2(b). The larger ⟨Fe-O⟩ value in Ge-Pv allows Fe^{2+} to sustain higher pressures than in Si-Pv before changing to the high-QS state. It is also interesting to note that this transition occurs when the ⟨Fe-O⟩ reaches a particular value (∼2.22(1) $\AA$) whether in Ge-Pv or in Si-Pv, whether using LDA+U_{sc} or GGA+U_{sc} methods (Fig. 3.2.(b)). In the case of Fe^{2+}-bearing Si-PPv phase, it was shown by [87] that lowest energy state of Fe^{2+} was high-QS below 200 GPa. In spite of larger Ge size, it is very unlikely that low- to high-QS trasntion in Ge-PPv phase would interfere with the Pv to PPv transition.

For this reason, we have not investigated low- to high-QS transition in the PPv phase.

3.3.2 Spin states of Fe^{3+} in Ge-Pv, Ge-PPv, Si-Pv, and Si-PPv

Next, we investigate spin states of Fe^{3+} in the B-site of Ge-Pv (low-pressure) and PPv (high-pressure) phases. The crystal structures of Si-Pv and Si-PPv phases are shown in Fig. 3.3(a). Si-PPv has a layered structure characterized by corner-sharing and edge-sharing SiO_6 octahedron extending along the a-c plane. The pressure dependence of calculated enthalpy differences between high-spin (HS) and low-spin (LS) states of Fe^{3+} ($\Delta H = H_{B(LS)} - H_{B(HS)}$) in Pv and PPv phases are shown in Fig. 3.3 (b) and (c), respectively. The calculated HS to LS transition pressures in Ge-Pv are 56.5 GPa with LDA+U_{sc} and 85.0 GPa with GGA+U_{sc}. Similarly, these transition pressures in Ge-PPv are 49.5 GPa and 82.5 GPa with these methods. Our calculated transition pressures in Si-Pv are 41.0 GPa with LDA+U_{sc} and 69.5 GPa with GGA+U_{sc}, which are in very good agreement with previous first-principles study [75]. In the case of Si-PPv, our calculated transition pressures are 28.0 GPa and 59.5 GPa, respectively, which are quite larger than previously reported values of -30 GPa and 36 GPa [87]. These transition pressures in Si-Pv and Si-PPv are also very similar to those reported by [88] in (Mg,Al)(Si,Fe)O_3-Pv and PPv phases where it was observed that the presence of aluminum does not affect the spin transition pressure significantly. Considering the overall agreement of the stability of the iron spin states and pressure induced crossover in Si-Pv and Si-PPv phases with previous studies [74, 75, 88], the present calculations about HS to LS transition in Fe^{3+} at B site seems to be consistent and reliable.

In order to explain the increase of HS to LS transition pressures in $MgGeO_3$ phases, we compare atomic configurations around Fe^{3+} in the B-site of Si-Pv and Ge-Pv phases. As shown in Fig. 3.4(a), the coordination number of Fe^{3+} is six and Fe-O bond lengths in this site are smaller than those of Fe^{2+} in the A-site. The pressure dependence of

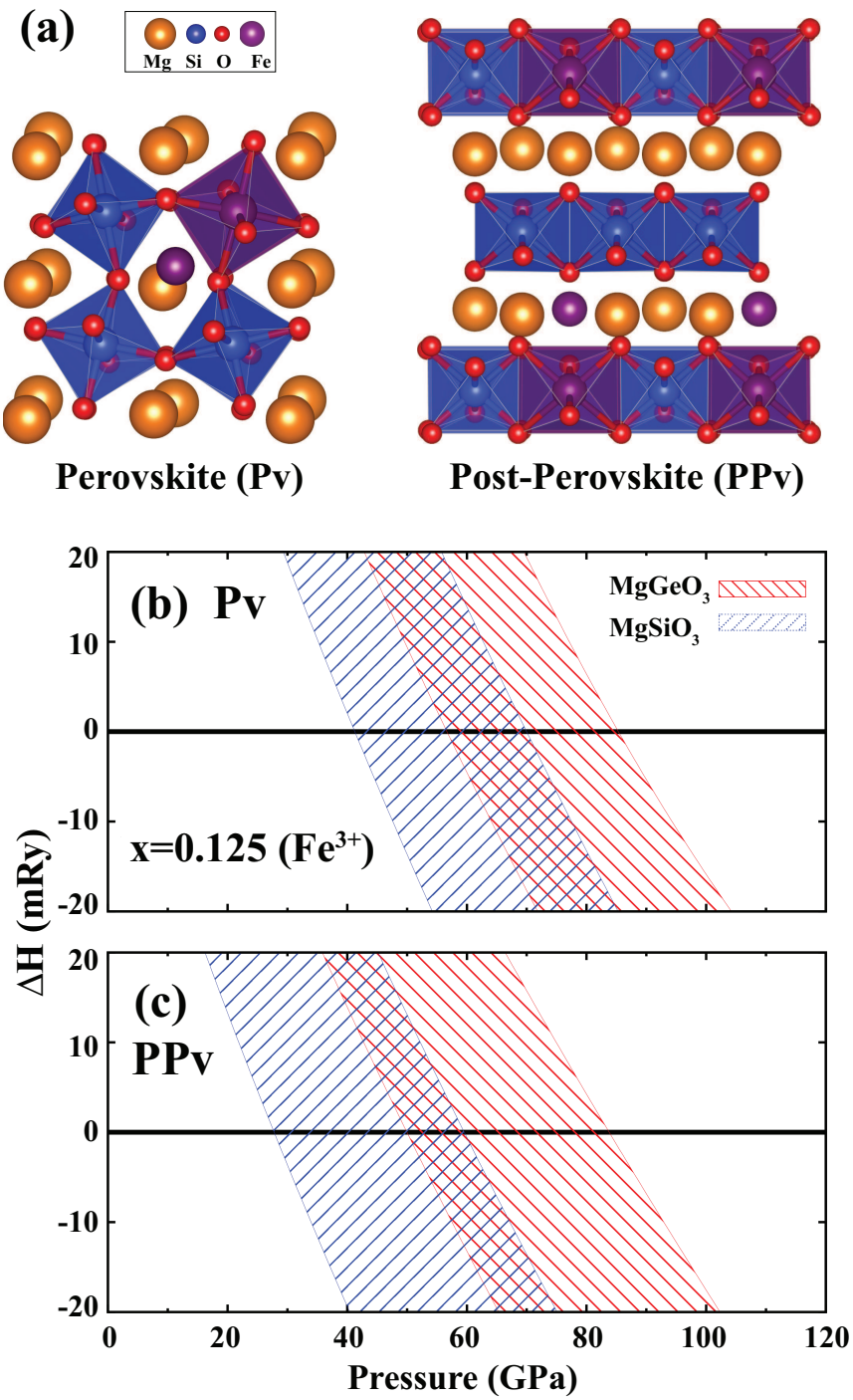

Figure 3.3: (a) Atomic structure of Fe^{3+}-bearing $MgSiO_3$ Pv and PPv phase. Structures of Pv and PPv phases of Fe^{3+}-bearing $MgGeO_3$ are similar and not shown here. Fe, Mg, O, and Si are represented as purple, orange, red, and blue sphere, respectively. Enthalpy difference ($\Delta H = H_{B(LS)} - H_{B(HS)}$) for Fe^{3+}-bearing $MgSiO_3$ (blue) and $MgGeO_3$ (red) in (b) Pv and (c) PPv phases. Lower and upper bounds correspond to LDA+U_{sc} and GGA+U_{sc} results, respectively.

the average bond-length, ⟨Fe-O⟩, for Fe^{3+} in the B-site in Si-Pv and Ge-Pv phases are shown in Fig. 3.4(b). As in the case of low- to high-QS transition in Fe^{2+} (Fig. 3.1), the HS to LS transition in Fe^{3+} in Ge-Pv and Ge-PPv phases are also large compared to those in Si-Pv and Si-PPv phases (Fig. 3.3) due to relatively larger Fe-O bond-lengths and unit-cell volumes in germanate phases at a given pressure (Fig. 3.4). Similar to low- to high-QS transition, the HS to LS transition also occurs only when the ⟨Fe-O⟩ reaches a particular value (i.e., ∼1.86(1) $\mathring{A}$ in the present case) irrespective of Ge-Pv or Si-Pv, or of the exchange-correlation functional used (Fig. 3.4(b)). This is a useful insight for predicting pressure induced spin state changes in different materials.

Having investigated the stability of different iron states in the lower mantle pressure range in the previous section, we now focus on the potential effect of Fe^{2+} and Fe^{3+} substitution on the Pv to PPv transition. This is a plain static calculation to access the overall influence of iron substitution on the Pv to PPv transition in these phases. We have not included finite temperature entropic or vibrational effects, therefore, we are not able to produce a full phase diagram with a two phase loop region. This is simply the first step towards the calculation of such phase diagrams. It is well known that the LDA functional underestimates the equilibrium volume while GGA overestimates it. After inclusion of vibrational effects LDA equations of state and elastic properties tend to agree better with experimental data than GGA results [48, 49, 50]. Therefore, we have chosen LDA+U_{sc} results to investigate the effect of Fe^{2+} and Fe^{3+} in the Pv to PPv transition in both compounds. Previous studies based on *ab initio* calculations [54, 100] and experimental measurements [91, 99] have reported the Pv to PPv transition in $MgSiO_3$ and $MgGeO_3$ to occur around ∼125 GPa and ∼63 GPa, respectively, at ∼2500 K.

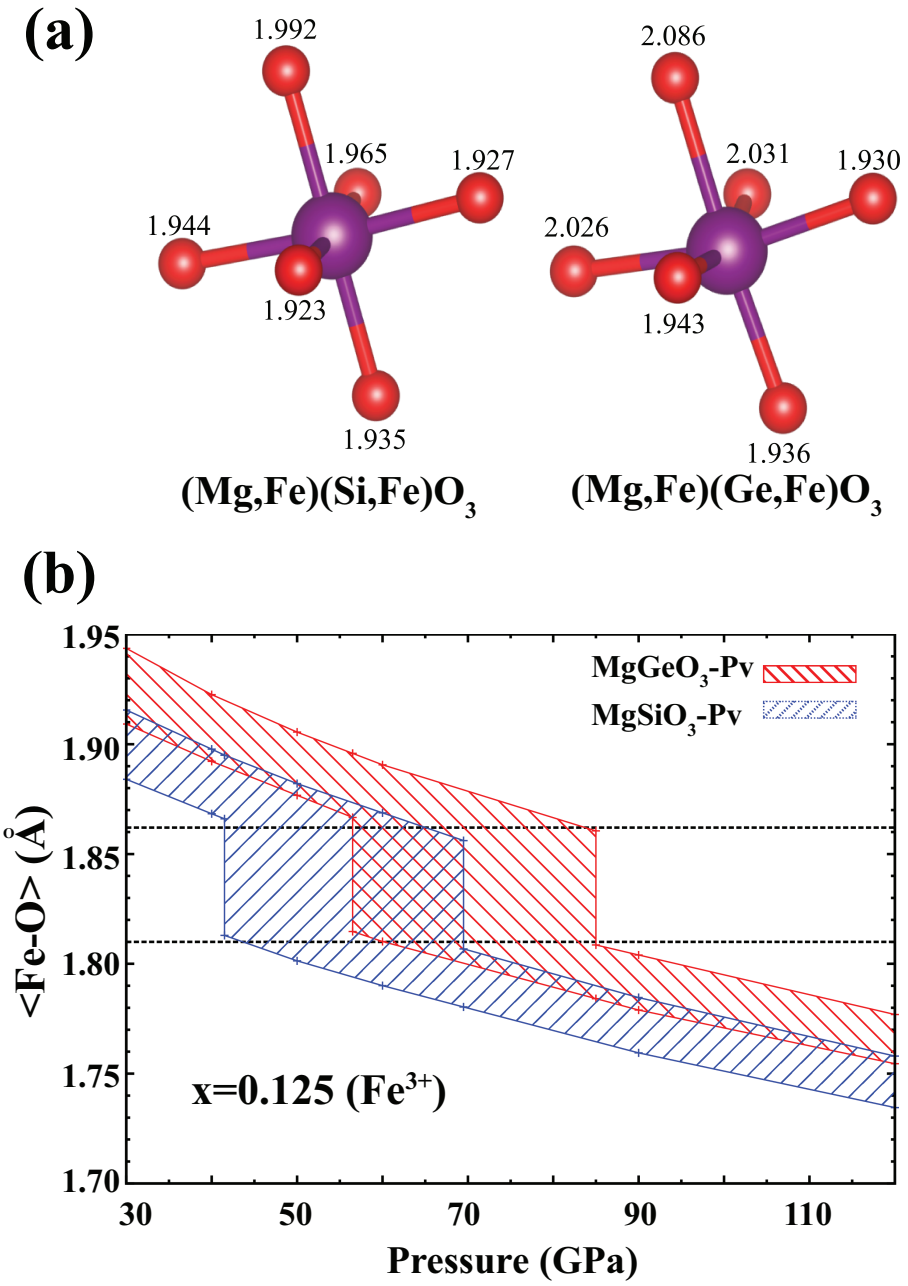

Figure 3.4: Atomic environment around Fe^{3+} in Si-Pv and Ge-Pv phases. (a) Zero pressure Fe-O bond lengths ($\AA$) in Si-Pv and in Ge-Pv obtained with LDA+U_{sc}. (b) Pressure dependence of average Fe-O bond lengths for $MgSiO_3$ (blue) and $MgGeO_3$ (red) phases. Vertical lines represent the high- (HS) to low-spin (LS) transitions in the B-site. Lower and upper bounds correspond to LDA+U_{sc} and GGA+U_{sc} results, respectively.

Table 3.3: Perovskite to post-perovskite transition pressures, P_C(GPa), calculated within LDA+U_{sc} methods. x represents the iron concentration.

x	0	0.125 (Fe^{2+})	0.125 (Fe^{3+})
$MgGeO_3$	43.2	40.5	57.5
$MgSiO_3$	94.0	88.5	104.0

3.4 Effect of Fe^{2+} and Fe^{3+} in Pv to PPv transition

As indicated in Fig. 3.1(b) and in Table 3.2, the low- to high-QS transition in Si-Pv and Ge-Pv occurs at much lower pressures than the Pv to PPv transition in these minerals [91, 99]. Considering this fact, only the high pressure high-QS state of Fe^{2+} was considered in the investigation of the Pv to PPv transition. Similarly, near the Pv to PPv transition pressure, the stable state of Fe^{3+} substituted in both Si-Pv and Si-PPv phases is HS state in the A-site (HS-A) and LS state in the B-site (LS-B). However, in germanate phases, the HS-B to LS-B transition pressure (Fig. 3.3 and Table 3.2) is near the Pv to PPv transition pressure. In order to find the appropriate spin states of Fe^{3+} across the transition we have considered all possibilities in the calculation of enthalpy differences ($\Delta H = H_{PPv} - H_{Pv}$) (see Fig. 3.5). As indicated in Fig. 3.5(b) the transition pressure 55.5 GPa involves a transition between HS-B in Ge-Pv to LS-B in Ge-PPv. Obviously iron in the A site remains in the HS state. At high temperatures, contributions by other states might be relevant as well, but this issue is well beyond the scope of this paper.This transition and transition pressure, i.e., HS-B in Pv and LS-B in PPv, is the only combination consistent with B(HS) to B(LS) transition pressures of 56.5 GPa and 49.5 GPa in Ge-Pv and Ge-PPv, respectively.

The effect of Fe^{2+} and Fe^{3+} on the Pv to PPv transition in Si-Pv and Ge-Pv is summarized in Fig. 3.6 showing the pressure dependence of enthalpy differences ($\Delta H = H_{PPv} - H_{Pv}$) for the configurations indicated in the previous paragraph. Static (zero temperature) Pv to PPv transition pressures in iron-free (x=0) $MgGeO_3$ and

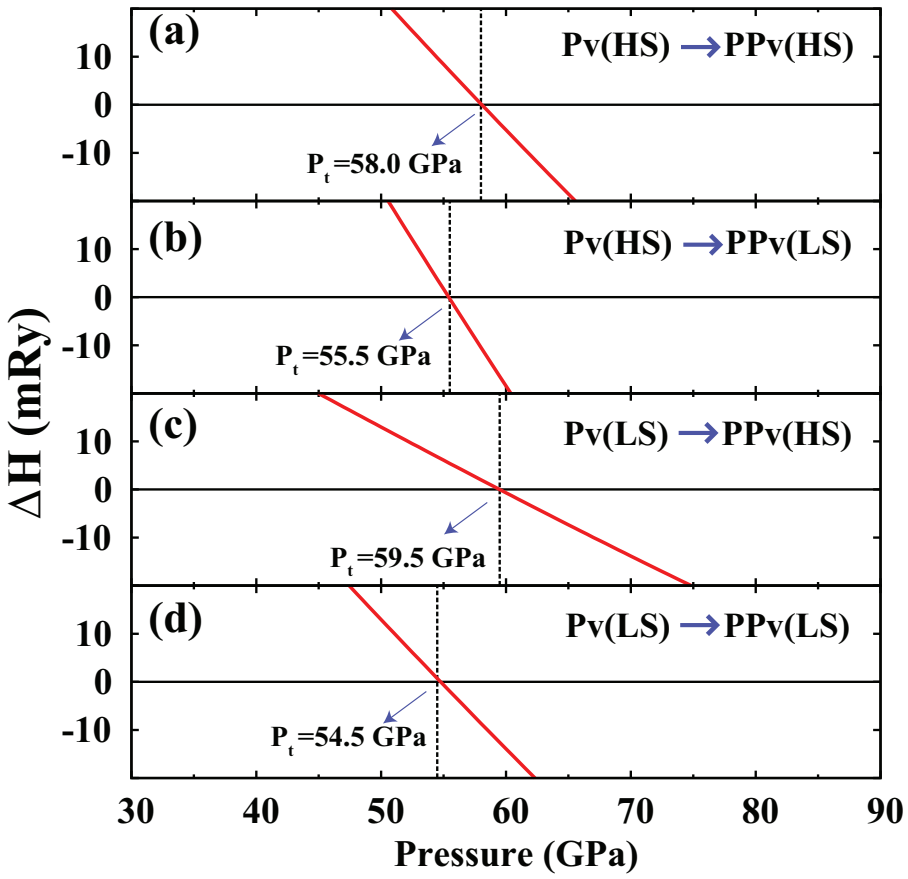

Figure 3.5: Enthalpy difference (ΔH=H$_{PPv}$-H$_{Pv}$) between Fe^{3+}-bearing Ge-Pv and Ge-PPv phase using LDA+U$_{sc}$ method with different possible spin-state combinations of Fe^{3+} at B-site. (a) Pv(HS) and PPv(HS), (b) Pv(HS) and PPv(LS), (c) Pv(LS) and PPv(HS), (d) Pv(LS) and PPv(LS).

$MgSiO_3$ are 43.2 GPa and 94 GPa, respectively. The Clapeyron slope for the Pv to PPv transitions have been previously estimated to be $\sim$ 7.5 MPa/K for $MgSiO_3$ [54] and 7.8 MPa/K for $MgGeO_3$ [100]. Taking these Clapeyron slopes approximately into account, transition pressures at $\sim$2500 K should be $\sim$ 62.7 GPa and $\sim$ 112.8 GPa for $MgGeO_3$ and $MgSiO_3$, respectively. These results are in good agreement with previous experimental measurements and *ab initio* LDA calculations [54, 91, 92, 99, 100].

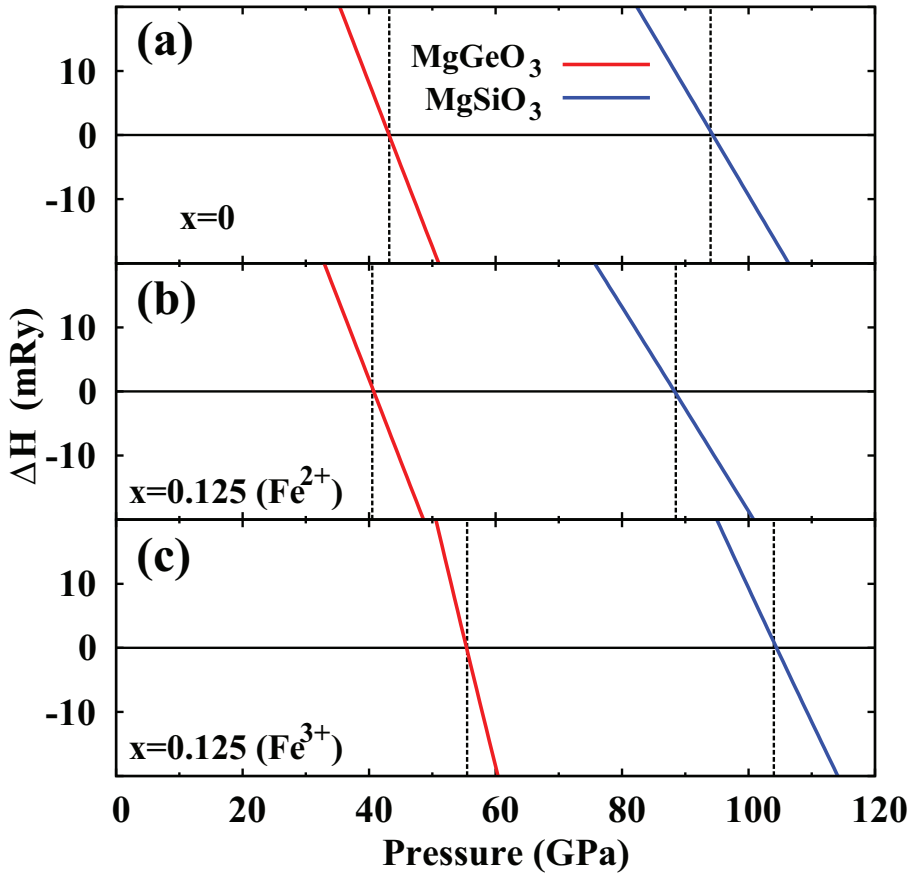

Figure 3.6: Enthalpy difference ($\Delta H = H_{PPv} - H_{Pv}$) obtained using LDA+$U_{sc}$ for (a) iron free, (b) Fe^{2+}-, and (c) Fe^{3+}-bearing Si-Pv and Ge-Pv.

A summary of Pv to PPv transition pressure shifts caused by iron in silicate and germanate phases is shown in Fig. 3.6 and Table 3.3. The inclusion of Fe^{2+} results

in decrease of the Pv to PPv transition pressure for both $MgGeO_3$ and $MgSiO_3$ which is in agreement with previous *ab initio* studies [103, 104]. This is also consistent with experimental studies by *Mao et al., 2004* [105] and *Shieh et al., 2006* [106], but contradicts the observations by *Tateno et al., 2007* [107] and *Hirose et al., 2008* [108]. *Mao et al., 2004* [105] and *Shieh et al., 2006* [106] also found that PPv phase of $MgSiO_3$ was Fe^{2+} enriched in the two phase region, while *Tateno et al., 2007* [107] and *Hirose et al., 2008* [108] noticed that Pv phase contains more Fe^{2+}. Equal Fe^{2+} concentration in our computations for Pv and PPv phases might have lead to the differences in transition pressures obtained with experimental studies. In the case of Fe^{3+} substitution, the Pv to PPv transition pressure increases noticeably and this trend is in good agreement with experimental observations [108, 109]. To understand these opposite effects of Fe^{2+} and Fe^{3+} substitution on the Pv to PPv transition, the volume difference between Si-Pv and Si-PPv phase ($\Delta V = V_{PPv} - V_{Pv}$) is shown in Fig. 3.7(a). With respect to iron-free case, the volume difference is smaller and larger in magnitude with Fe^{2+} and Fe^{3+} substitution, respectively. These smaller and larger volume difference will contribute to enthalpy difference between Pv and PPv phase in such a way that will decrease the transition pressure with Fe^{2+} substitution while it will increase when Fe^{3+} is substituted. This can be seen explicitly in Fig. 3.7(b and c), where pressure dependence of energy (ΔE) and $P \times V$ term [$\Delta(PV)$] of relative enthalpy (ΔH) are shown separately. Transition pressure points, where ΔE and $\Delta(PV)$ terms cancel each other, are shown by vertical dashed lines.

3.5 Conclusions

Using *ab initio* DFT+U calculations, we have undertaken a comparative investigation of state changes of ferrous (Fe^{2+}) and ferric (Fe^{3+}) iron in $MgSiO_3$ and $MgGeO_3$ perovskite (Pv) and post-perovskite (PPv) phases. The goal was to verify the possibility of using

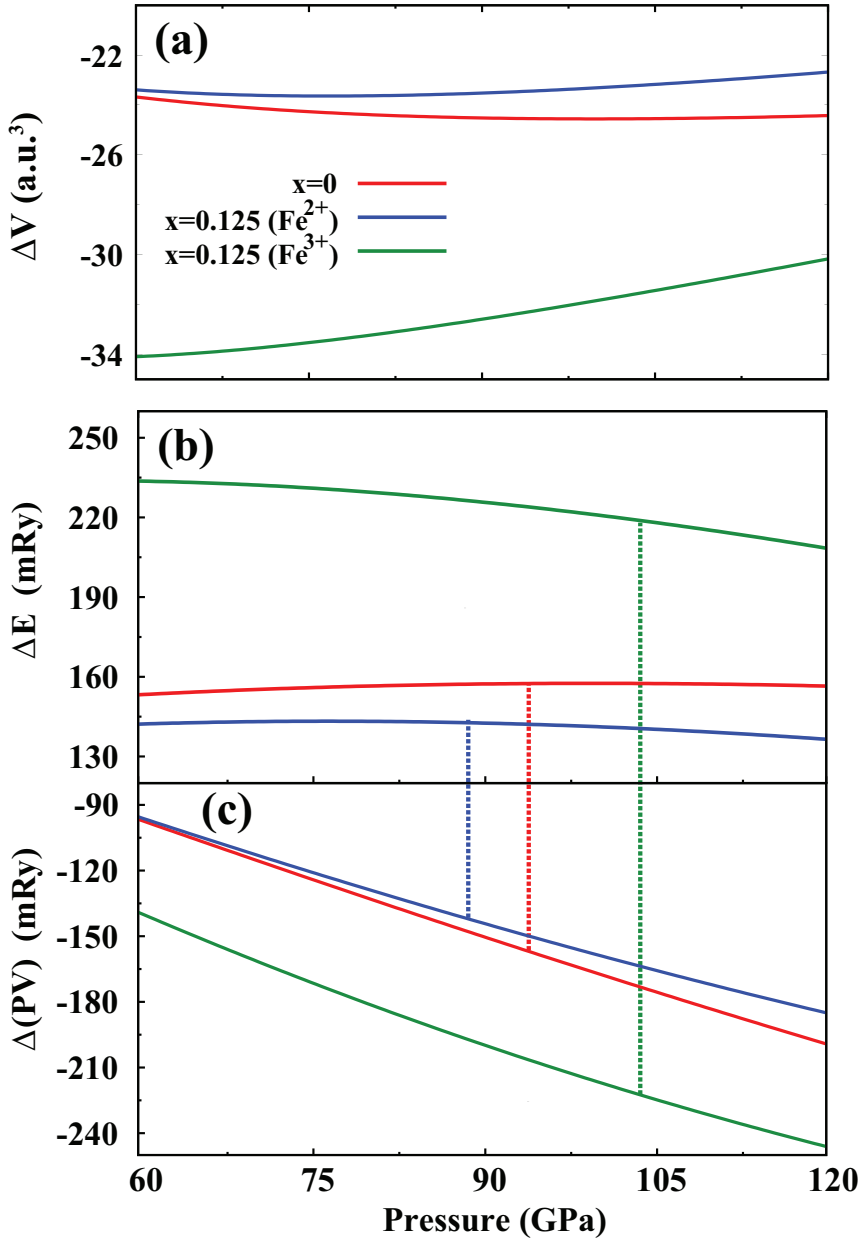

Figure 3.7: Difference in (a) volume ($\Delta V = V_{PPv} - V_{Pv}$), (b) internal energy ($\Delta E = E_{PPv} - E_{Pv}$), and (c) PV term ($\Delta(PV) = (PV)_{PPv} - (PV)_{Pv}$) of the enthalpy for iron-free (red), Fe^{2+}-bearing (blue), and Fe^{3+}-bearing (green) $MgSiO_3$. Results represent LDA+U_{sc} calculation. Vertical dashed lines represent Pv to PPv transition point.

$MgGeO_3$ as a low pressure analog of $MgSiO_3$ for better understanding of spin state changes in iron. Unfortunately, owing to the larger ionic radius of germanium, Fe-O inter-atomic distances in the germanate phases are larger than in the silicate phases, allowing the germanates to sustain higher pressures than analog silicates before state changes in iron take place. It has been clearly shown that such state changes, whether the displacement transition (low- to high-QS) of Fe^{2+} in the A-site or the HS to LS state change in Fe^{3+} in the B-site, take place at approximately the same average Fe-O, $\langle$Fe-O$\rangle$, distance irrespective of the chemistry or the exchange and correlation functional used in the calculations. This encompassing investigation also allowed us to address the effect of Fe^{2+} and Fe^{3+} substitutions on the Pv to PPv transition. Despite the simplicity of these static calculations, previously measured and calculated effect of Fe^{2+} on this transition in $MgSiO_3$ is well reproduced: Fe^{2+} substitution decreases the transition pressure, whether in germanate or silicate phases. However, we report the opposite effect for Fe^{3+} substitution in the B-site. This transition should involve the LS-B state in both Pv and PPv silicate phases but HS-B and LS-B states in Pv and PPv germanates, respectively. For both types of transitions the effect is the same: coupled substitution of Fe^{3+} increases the Pv to PPv transition in both materials. This observation has not been validated by experiments yet and should be relevant for better understanding the D“ discontinuity and the nature of the deep lower mantle.

Chapter 4

Spin crossover in Fe^{3+}-bearing bridgmanite: effects of disorder, iron concentration, and temperature

In this chapter, we investigate effects of disorder, iron concentration, and temperature on the spin crossover of $[Fe^{3+}]_{Si}$ in Fe^{3+} in $(Mg_{1-x}Fe_x)(Si_{1-x}Fe_x)O_3$ bridgmanite using *ab initio* LDA + U calculations. The effect of concentration and disorder are addressed using complete statistical samplings of coupled substituted ($[Fe^{3+}]_{Mg}$ and $[Fe^{3+}]_{Si}$ in nearest neighbor sites) configurations in 80-, 40-, and 20-atom supercells for iron concentration of x = 0.125, 0.25, and 0.50, respectively. Vibrational/thermal effects on the crossover are also addressed within the quasi-harmonic approximation for x = 0.125. $[Fe^{3+}]_{Si}$ in the perovskite octahedral site undergoes high (S=5/2) to low-spin (S=1/2) state change in the pressure range ∼40-50 GPa at 300 K, consistent with experiments,

while $[Fe^{3+}]_{Mg}$ remains in the high-spin state up to core-mantle boundary conditions. The effect of disorder on the crossover seems very small, while increase in the iron concentration (x) results in considerable increase in transition pressure. As in the spin crossover in ferropericlase, this crossover in bridgmanite is accompanied by clear volume reduction and anomalous softening of the bulk modulus throughout the crossover pressure range. These effects reduce significantly with increasing temperature. Though the concentration of $[Fe^{3+}]_{Si}$ in bridgmanite may be small, related elastic anomalies may impact the interpretation of radial and lateral velocity structures of the Earth's lower mantle.

4.1 Introduction

Bridgmanite (br), (Mg,Fe,Al)(Si,Fe,Al)O_3 perovskite (Pv), is the main constituent of the Earth's lower mantle along with (Mg,Fe)O, $CaSiO_3$ Pv, and (Mg,Fe,Al)(Si,Fe,Al)O_3 post-perovskite (PPv). Thermodynamics and elastic properties of these minerals provide a direct link to seismic tomographic models. Understanding the effect of iron (Fe) and/or aluminum (Al) substitutions on the physical, chemical, and thermodynamic properties of the host mineral is essential to constrain the composition and thermal structure of the Earth's lower mantle. Ferropericlase (Fp), (Mg,Fe)O, is know to undergo a pressure induced spin transition from the high (S=2) to the low-spin (S=0) state and affects its elastic and thermal properties [52, 53, 55, 56, 57, 58, 59, 60, 61, 62].

In the case of iron-bearing bridgmanite, in spite of considerable progress of experimental measurements at high pressures and high temperatures [3, 63, 64, 66, 68, 71, 73, 76, 77, 78, 101, 102, 110, 111, 112, 113, 114, 116, 118, 119], deciphering the valence and spin states of multivalent iron and its influence on the physical properties has been quite a formidable challenge due to complexity of the perovskite structure. Iron in bridgmanite may exists in ferrous (Fe^{2+}) and ferric (Fe^{3+}) states. Fe^{2+} occupies the

A-site ($[Fe^{2+}]_{Mg}$), while Fe^{3+} can occupy A- ($[Fe^{3+}]_{Mg}$) and/or B-site ($[Fe^{3+}]_{Si}$) of the perovskite structure [3, 63, 64, 66, 68, 70, 71, 72, 73, 74, 75, 76, 101, 102, 113, 118, 119]. In the entire lower mantle pressure-range, $[Fe^{2+}]_{Mg}$ remains the HS state (S=2) but undergoes through the pressure induced lateral displacement resulting in the state with increased iron Mössbauer quadrupole splitting (QS) [3, 72, 74, 76, 77, 79, 116, 117]. On the other hand, $[Fe^{3+}]_{Si}$ goes from the HS (S=5/2) to the LS (S=1/2) state and $[Fe^{3+}]_{Mg}$ remains in the HS (S=5/2) state [3, 75, 76, 81, 118, 119, 124].

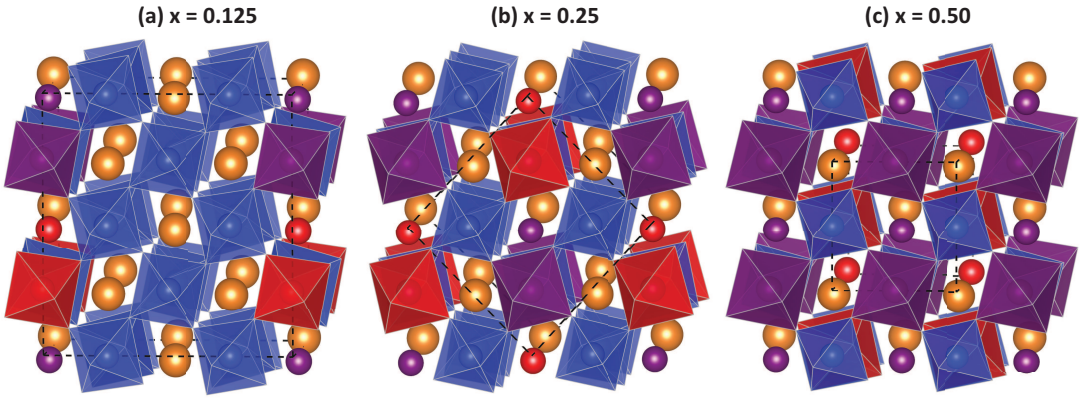

Figure 4.1: Lowest enthalpy atomic configurations for two (purple and red) nearest neighbor $[Fe^{3+}]_{Mg}$-$[Fe^{3+}]_{Si}$ pairs in $(Mg_{1-x}Fe^{3+}_x)(Si_{1-x}Fe^{3+}_x)O_3$ bridgmanite. Unit cells consists of 80 atoms ($2 \times 2 \times 1$ super-cell) for x = 0.125, 40 atoms ($\sqrt{2} \times \sqrt{2} \times 1$ super-cell) for x = 0.25, and 20 atoms for x = 0.50 are shown by black dashed lines. There are 21, 13, and 5 configurations in 80, 40 , and 20 atoms unit-cell, respectively. Si-O octahedron and Mg atom is represented by blue and orange color, respectively.

The onset of the HS to LS crossover in $[Fe^{3+}]_{Si}$ is still much debated. For x = 0.10, *Catalli et al., 2010b* [81] reported the completion the crossover at 53-63 GPa by x-ray emission spectroscopy(XES) and 48 GPa by Mössbauer spectroscopy (SMS). Using

SMS, [76] found the crossover pressure range 13-24 GPa for a sample containing about ∼2.0-2.5% of Fe^{3+}. *Lin et al., 2012* [76] and *Mao et al., 2015* [118] further argued that the lower crossover pressure obtained by them could be related to the smaller Fe^{3+} concentration in their samples. *Hsu et al., 2011* [75] calculated the crossover pressure 41 GPa and 70 GPa, for x = 0.125, within the LDA + U_{sc} and GGA+U_{sc} functionals, respectively, while *Tsuchiya et al., 2013* [119] reported 44 GPa for x = 0.0625 using LDA + U. Using thermodynamic model based on *ab initio* calculations, *Xu et al., 2015* [124] estimated $Fe^{3+}/\sum$Fe ratio under lower mantle conditions to be ∼0.01-0.07 in Al-free bridgmanite. They also predicted that spin crossover in $[Fe^{3+}]_{Si}$ would decrease the value of $Fe^{3+}/\sum$Fe in the crossover region. In an effort to understand and reconcile observations and results of these studies, we have investigated the HS to LS crossover in Fe^{3+}-bearing bridgmanite by taking into account the effect of 1) disordered substitution of nearest neighbor Fe^{3+}-Fe^{3+} pairs, 2) Fe^{3+} concentration, and 3) vibrational effects on the HS to LS crossover in Fe^{3+}-bearing bridgmanite.

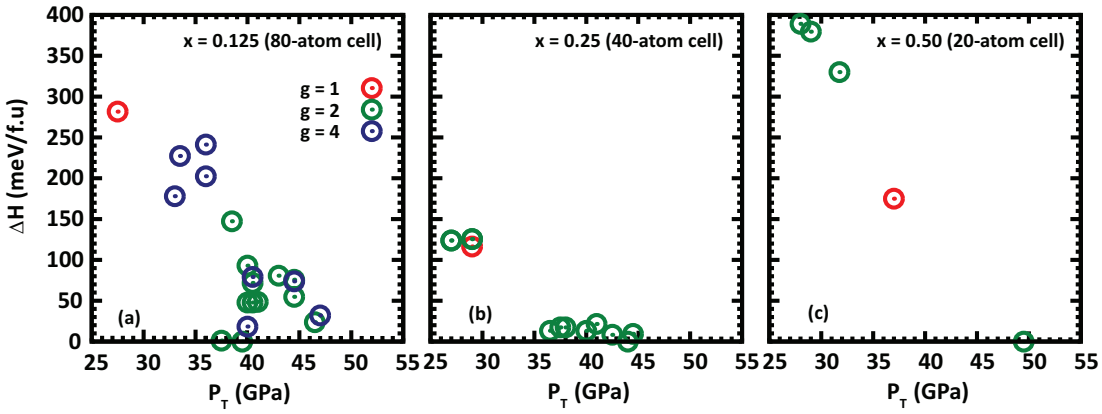

Figure 4.2: Relative enthalpy per forumula unit (f.u) at transition pressures of all configurations with respect to lowest energy configuration for (a) $x = 0.125$ (80 atoms), (b) $x = 0.25$ (40 atoms), and (c) $x = 0.50$ (20 atoms), respectively. g represents the multiplicity of a particular configuration.

4.2 Computational details and Methodology

4.2.1 Computational details

Density functional theory (DFT) within the local density approximation (LDA) [18] has been used. It is well known that standard DFT functionals do not capture strong correlation effects of $3d$ and $4f$ electrons properly. For this reason, the DFT method is augmented by the the self- and structurally consist Hubbard U_{sc} (LDA + U_{sc}) [10, 11, 12]. Self- and structurally-consistent U_{sc} values reported by *Hsu et al., 2010* [74] using the linear response approach [10, 11] have been used. Disordered substitution of Fe^{3+} in $(Mg_{1-x}Fe_x)(Si_{1-x}Fe_x)O_3$ bridgmanite with varying iron concentration has been investigated in 80- (x = 0.125), 40- (x = 0.25), and 20-atoms (x = 0.50) super-cells (Fig. 4.1). Ultrasoft pseudo-potentials [28] have been used for Fe, Si, and O. For Mg, a norm-conserving pseudo-potential generated by von Barth-Car's method has been used. A detailed description of these pseudo-potentials has been reported by *Umemoto et al., 2008* [125]. The plane-wave kinetic energy and charge density cut-off are 40 Ry and 160 Ry, respectively. For 80-, 40-, and 20-atom super-cells, the electronic states were sampled on a shifted $2 \times 2 \times 2$, $4 \times 4 \times 4$, and $6 \times 6 \times 4$ k-point grid [20], respectively. Structural optimization at arbitrary pressure has been performed using variable cell-shape damped molecular dynamics [13, 14]. Structures are optimized until the inter-atomic forces are smaller than 10^{-4} $Ry/a.u.$ Vibrational density of states (VDOS) for Fe^{3+} concentration x = 0.125 has been calculated in a 40-atom super-cell using density functional perturbation theory (DFPT) [121] within the LDA + U_{sc} functional [123]. For this, dynamical matrices on a $2 \times 2 \times 2$ q-point grid of a 40-atom cell were calculated and obtained force constants were interpolated on a $8 \times 8 \times 8$ q-point grid. High throughput calculations have been performed using the VLab cyberinfrastructure at the Minnesota Supercomputing Institute [127].

4.2.2 Disordered substitution of Fe^{3+} and spin transition

Disordered substitution of Fe^{3+} in $(Mg_{1-x}Fe^{3+}_x)(Si_{1-x}Fe^{3+}_x)O_3$ has been studied by replacing a nearest neighbor Mg^{2+}-Si^{4+} pair with a $[Fe^{3+}]_{Mg}$-$[Fe^{3+}]_{Si}$ pair and generating all possible atomic configurations consitent with super-cell size. The number of symmetrically inequivalent configurations, N_c, are 21, 13, and 5 in 80- (x = 0.125), 40- (x = 0.25), and 20-atom (x = 0.50) super-cells, respectively. Within quasi-harmonic approximation (QHA) [126], the partition function for disordered system with $[Fe^{3+}]_{Si}$ in a spin state σ is given by

$$Z^{QHA}_{\sigma}(T,V) = \sum_{i=1}^{N_c} g_i M_\sigma \exp\left\{-\frac{E^i_\sigma(V)}{k_B T}\right\} \times \prod_{j=1}^{N_{mode}} \left[\sum_{\nu_{i,j}=0}^{\infty} \exp\left\{-\left(\nu_{i,j}+\frac{1}{2}\right)\frac{\hbar\omega_{i,j,\sigma}(V)}{k_B T}\right\}\right] \quad (4.1)$$

where g_i is the multiplicity of symmetrically equivalent configurations and E^i_σ(V) is the static energy of the i^{th} inequivalent configuration at volume V. M_σ the magnetic degeneracy of the system, which includes the spin and orbital degeneracy. $\nu_{i,j}$ and $\omega_{i,j,\sigma}(V)$ are the number of exited phonons and frequency of j^{th} mode at volume V for i^{th} configuration. k_B and $\hbar$ are the Boltzmann's and Planck's constants, respectively. N_c and N_{mode} are the total number of configurations and vibrational modes of a given super-cell. After summing over $\nu_{i,j}$, the partition function is written as

$$Z^{QHA}_{\sigma}(T,V) = \sum_{i=1}^{N_c} g_i M_\sigma \exp\left\{-\frac{E^i_\sigma(V)}{k_B T}\right\} \times \prod_{j=1}^{N_{mode}} \left\{\frac{\exp\left(-\frac{\hbar\omega_{i,j,\sigma}(V)}{2k_B T}\right)}{1-\exp\left(-\frac{\hbar\omega_{i,j,\sigma}(V)}{k_B T}\right)}\right\}. \quad (4.2)$$

The Helmholtz free-energy for the system with $[Fe^{3+}]_{Si}$ in HS/LS state can be calculated as

$$F_{HS/LS}(T,V) = -k_B T \ln\left[Z^{QHA}_{HS/LS}(T,V)\right] = F^{conf+vib}_{HS/LS}(T,V) + F^{mag}_{HS/LS}(T,V), \quad (4.3)$$

where $F^{mag}_{HS/LS}(T,V) = -k_B T ln\left(M_{HS/LS}\right)$ is the magnetic contribution to free-energy. As mentioned before, Fe^{3+} in $(Mg_{1-x}Fe^{3+}_x)(Si_{1-x}Fe^{3+}_x)O_3$ occupies as a charge-coupled $[Fe^{3+}]_{Mg}$-$[Fe^{3+}]_{Si}$ pair with molar fraction x, where $[Fe^{3+}]_{Mg}$ is always in the HS state while $[Fe^{3+}]_{Si}$ undergoes HS to LS crossover. Therefore, magnetic degeneracies M_{HS} and M_{LS} are given by

$$\begin{aligned} M_{HS} &= \left[m^O_{HS}(S_{HS}+1) \times m^O_{HS}(S_{HS}+1)\right]^x \quad and \\ M_{LS} &= \left[m^O_{HS}(S_{HS}+1) \times m^O_{LS}(S_{LS}+1)\right]^x, \end{aligned} \tag{4.4}$$

where $m^O_{HS/LS}$ and $S_{HS/LS}$, respectively, are the orbital degeneracy and total spin of Fe^{3+} in HS and LS state. The Gibb's free energy of the system with $[Fe^{3+}]_{Si}$ in HS/LS state can be calculated as $G_{HS/LS}(T,V) = F_{HS/LS}(T,V) + PV$, which can be converted to $G_{HS/LS}(T,P)$ using $P = -\partial F/\partial V$.

To investigate the effect of HS to LS crossover of $[Fe^{3+}]_{Si}$, we consider the mixed state (MS) of HS and LS within the ideal solid solution approximation. This solid solution model of HS and LS iron is carried out in the $[Fe^{3+}]_{Si}$ sub-lattice only and is very appropriate for this type of problem [57, 59, 128]. The molar Gibb's free energy for the MS state is given by

$$G(P,T,n) = nG_{LS}(P,T) + (1-n)G_{HS}(P,T) + G^{mix}(P,T), \tag{4.5}$$

where n is the low-spin fraction and the mixing free-energy $G^{mix}(P,T)$ is

$$G^{mix}(P,T) = k_B T x[n\ln(n) + (1-n)ln(1-n)]. \tag{4.6}$$

Minimization of $G(P,T,n)$ with respect to LS fraction, n, leads to

$$n(P,T) = \frac{1}{1 + \frac{m^O_{HS}(2S_{HS}+1)}{m^O_{LS}(2S_{LS}+1)} \exp\left\{\frac{\Delta G^{conf+vib}_{LS-HS}}{xk_BT}\right\}}, \tag{4.7}$$

where $\Delta G^{conf+vib}_{LS-HS} = G^{conf+vib}_{LS} - G^{conf+vib}_{HS}$. For $[Fe^{3+}]_{Si}$ enclosed by ordered oxygen octahedron, orbital degeneracies are $m^{O}_{HS} = 1$ and $m^{O}_{LS} = 3$. Since the degeneracies of e_g and t_{2g} in the perovskite structure (as in the case of Fe^{3+}-bearing bridgmanite) are broken due to the presence of asymmetry in oxygen octahedron, $m_{LS} = 1$ has been used in most of the cases. However, to assess the effect of orbital degeneracies, $m_{LS} = 3$ case has also been tested while addressing the vibrational effects.

4.3 Results and discussion

4.3.1 Spin crossover in disordered system

We investigate the solid solution of $(Mg_{1-x}Fe_x)(Si_{1-x}Fe_x)O_3$ by sampling the complete phase space of configurations of $[Fe^{3+}]_{Mg}$-$[Fe^{3+}]_{Si}$ pair in supercells containing 80-, 40-, and 20-atoms. In this study, we have considered only the nearest neighbor $[Fe^{3+}]_{Mg}$-$[Fe^{3+}]_{Si}$ substitution because this is the lowest energy configuration for coupled substitution [70, 75]. Representative crystal structures for this type of substitutions are shown in Fig. 4.1. Two $[Fe^{3+}]_{Mg}$-$[Fe^{3+}]_{Si}$ pairs (shown in purple and red color) are substituted in the 80, 40, and 20-atoms supercell for x = 0.125, 0.25, and 0.50, respectively. There are 21, 13, and 5 symmetrically different configurations, respectively, in these supercells. The static crossover pressures of HS to LS in $[Fe^{3+}]_{Si}$ and their relative enthalpy at crossover point for each configurations are shown in Fig. 4.2. The static crossover pressure for these configurations ranges from ∼27.5 GPa to ∼50.0 GPa. The lowest enthalpy configurations are shown in Fig. 4.1. In these configurations, Fe^{3+} ions are ordered in (010) plane of the perovskite structure. The trend observed here is similar to the one noticed by [125] for Fe^{2+} substitution in bridgmanite, where Fe^{2+} ions energetically preferred to be in (110)-plane. This observation suggest that Fe^{3+}] substitution in bridgmanite would prefer to be segregated at lower mantle pressure conditions. For

better understanding, this ordering effect should be investigated by sampling all possible configurations in a super-cell larger than the one containing 80-atoms (i.e., 120, 160, 320, and 360 atoms super-cell). However, this will be investigated in future.

First, we investigate the effect of Fe^{3+} pair disorder. Configurational entropy and its contribution to free-energy of HS and LS states has been calculated using eq. 4.3 and disregarding the vibrational contribution. The low-spin fraction, $n(P,T)$, shown in Fig. 4.3, was calculated using eq. 4.7. For x = 0.125, $n(P,T)$ for disordered systems (solid lines) at 300 K shifts toward the smaller pressure compare to that of the lowest energy configuration (dashed lines) due to contribution form the second lowest energy configuration with smaller static crossover pressure (P_T). At higher temperatures, the contribution form other configurations with higher energy and higher static P_T (Fig. 4.2(a)) shifts $n(P,T)$ towards higher pressures. The number of symmetrically inequivalent configurations decreases drastically with increasing Fe^{3+} concentration (Fig. 4.2(b,c)). For x = 0.25, the lowest energy configuration has the second highest static crossover pressure. In the disordered system, all other configurations with smaller P_T will contribute to shift $n(P,T)$ towards smaller pressure. In the case of x = 0.50, all other configurations have much higher energy and do not contribute significantly to change in $n(P,T)$ of disordered system at lower temperatures. However, at higher temperatures ($\geq$ 2000 K) other configurations contribute to decrease the crossover pressure and shift the crossover mid-point towards smaller pressure. Overall, the crossover pressure increases significantly with increasing Fe^{3+} concentration which is consistent with previous observations [76, 118].

4.3.2 Effect of vibrational contribution

Having investigated the effect disorder, we now focus on the vibrational effects. Owing to extremely high computational cost of vibrational density of states (VDOS) calculation

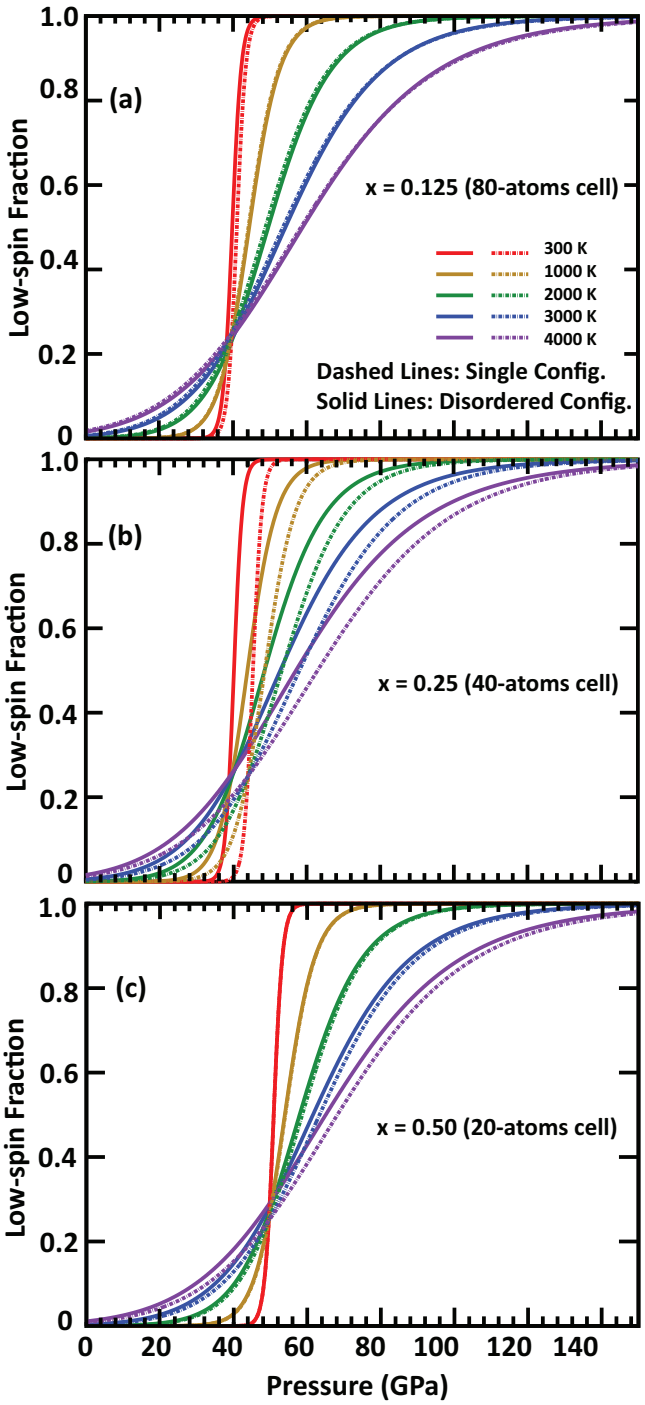

Figure 4.3: Pressure and temperature dependence of low-spin fraction (n) of $[Fe^{3+}]_{Si}$ in $(Mg,Fe^{3+})(Si,Fe^{3+})O_3$ bridgmanite in a) 80 , (b) 40, and (c) 20 atom super-cells, respectively. Solid lines represent disordered configurations while dashed lines are for the lowest energy configuration.

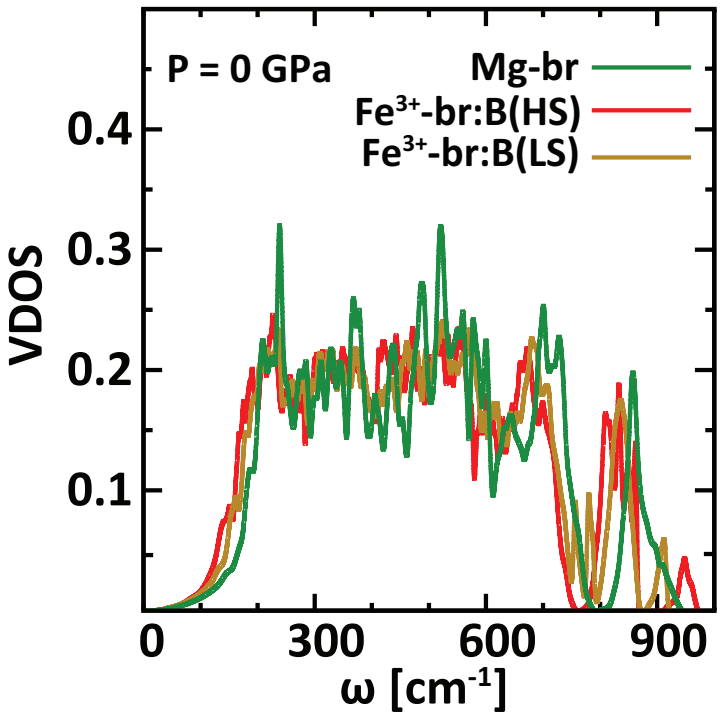

Figure 4.4: Vibrational density of states (VDOS) at 0 GPa for $MgSiO_3$ bridgmanite (Mg-br) using DFPT method [121], and for HS and LS state states of $[Fe^{3+}]_{Si}$ (i.e, ferric iron in B-site of the perovskite structure) in Fe^{3+}-bearing bridgmanite (Fe^{3+}-br) using DFPT + U_{sc} method [123].

(i.e., phonon frequencies $\omega_{i,j,\sigma}(V)$) using LDA + U_{sc} functional, we have investigated vibrational effects only for x = 0.125 concentration. Computational cost of VDOS calculation was further reduced by assuming that VDOS for a given Fe^{3+} concentration x is same for all symmetrically inequivalent configurations. For x = 0.125, VDOS calculation for HS and LS states of $[Fe^{3+}]_{Si}$ was performed in a 40-atoms super-cell. Representative of these VDOSs at 0 GPa are shown in Fig. 4.4. The VDOS spectrum for Fe^{3+}-br shifts towards lower frequencies with respect to that of $MgSiO_3$-bridgmanite (Mg-br) due to increased molecular weight of Fe^{3+}-br. The high frequency region of VDOS for the LS state of $[Fe^{3+}]_{Si}$ further shifts towards low frequency due to HS to LS crossover.

The vibrational contribution to the free-energy was calculated using QHA [120]. Using eq. 4.3, Gibb's free-energy was calculated separately for HS and LS states. The calculated low-spin fraction is shown in Fig. 4.5. Orbital degeneracy for the LS state, m_{LS}, is more likely to be 1 due to octahedron asymmetry. However, in order to assess the effects of orbital degeneracy variation, the calculated $n(P,T)$ for $m_{LS} = 1$ are also compared with that for $m_{LS} = 3$. Inclusion of vibrational contribution to free-energy increases the crossover pressure significantly. $n(P,T)$ with $m_{LS} = 1$ and 3 are also shown in Fig. 4.5(b) and in Fig. 4.5(c), respectively. Overall the pressure-temperature phase diagram of $n(P,T)$ for $m_{LS} = 1$ and 3 are similar except the smaller Clapeyron slope (dP_T/dT) in the latter case, which shifts the crossover region to the lower pressure range. Since the broadening of transition at higher temperatures is not affected by the choice of m_{LS} values, we will continue to use $m_{LS} = 1$ from here on out. The HS to LS transition shown here is much broader than that reported by *Tsuchiya et al., 2013* [119]. For example, our estimated transition pressure width at 300 K is about $\sim$8 GPa which agrees fairly well with the experimental measurements [76, 81, 118], while the one reported by *Tsuchiya et al., 2013* [119] is $<$2 GPa. These differences become more

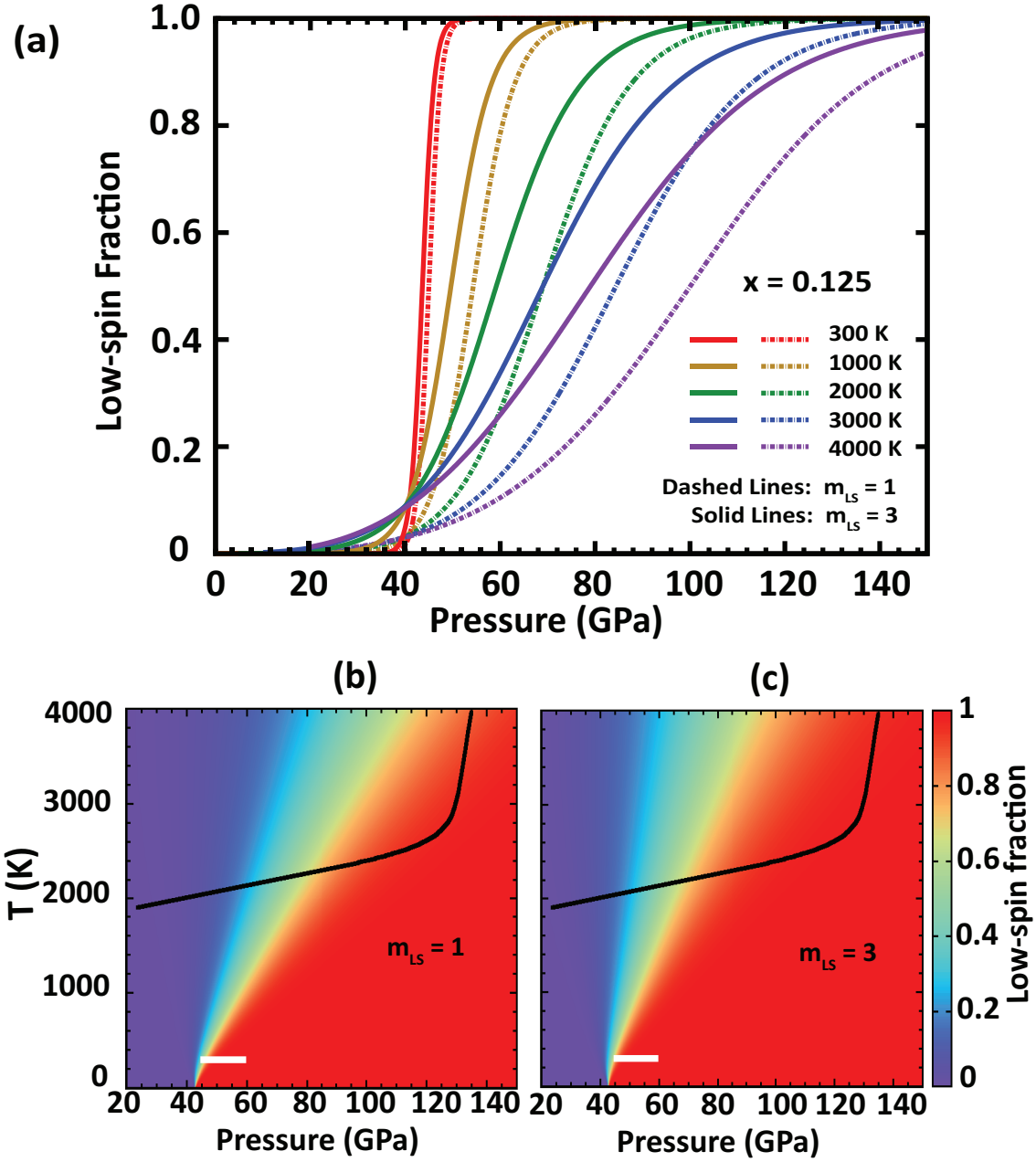

Figure 4.5: ((a) Low-spin fraction (n) of $[Fe^{3+}]_{Si}$ in $(Mg_{0.875}Fe_{0.125})(Si_{0.875}Fe_{0.125})O_3$ bridgmanite when vibrational effects are incorporated using quasi-harmonic approximation [120]. Dashed and solid lines represent the calculations for $m_{LS} = 1$ and 3, respectively. Pressure temperature phase diagram for HS to LS transition of $[Fe^{3+}]_{Si}$ (b) with $m_{LS} = 1$, and (c) $m_{LS} = 3$. Solid black curve in (b and c) represents the lower mantle model geother by *Boehler, 2000* [6], while white bar represents the experimental pressure range at room temperature in which HS to LS transition of $[Fe^{3+}]_{Si}$ is complete [81].

prominent at higher temperatures and may be related to the use of different values of Hubbard U and different techniques for VDOS calculations. The values of U used here were calculated self-consistently (i.e., starting form a trial LDA + U_{sc} ground state, self-consistent U_{sc}'s are obtained iteratively), while those reported by *Tsuchiya et al., 2013* [119] were calculated from LDA ground states. *Tsuchiya et al., 2013* [119] used a finite displacement method developed by *Alfè, 2009* [122] for VDOS computation and ignore the calculation of dielectric constant tensor that leads to LO-TO splitting for polar materials. Moreover, the numerical errors associated with small displacements may not be quite small. In this work, we have used DFPT + U_{sc} method developed by *Floris et al. 2011* [123] for VDOS computation, which is although computationally expensive but much more rigorous and effective approach to address lattice dynamical effects than that of finite displacement method [122]. This method has been successfully applied to address the lateral displacement of iron (a very delicate and highly debated phenomenon) and its associated change of Mössbauer quadrupole splitting (QS) in Fe^{2+}-bearing bridgmanite [79]. Therefore, we believe that calculation of VDOS and its free-energy contribution using DFPT + U_{sc} method is quite robust.

4.4 Effect of spin transition on volume and bulk modulus

4.4.1 Theoretical predictions

As shown in Fig. 4.5, HS to LS transition of $[Fe^{3+}]_{Si}$ in $(Mg,Fe^{3+})(Si,Fe^{3+})O_3$ is quite sharp in the lower temperature region and broadens significantly at higher temperature. To understand the elastic consequences of this transition, we used the formalism similar to [128] to calculate volume and bulk modulus for the mixed state (MS) of the HS and LS states. The pressure and temperature dependence of volume of the MS state is given as

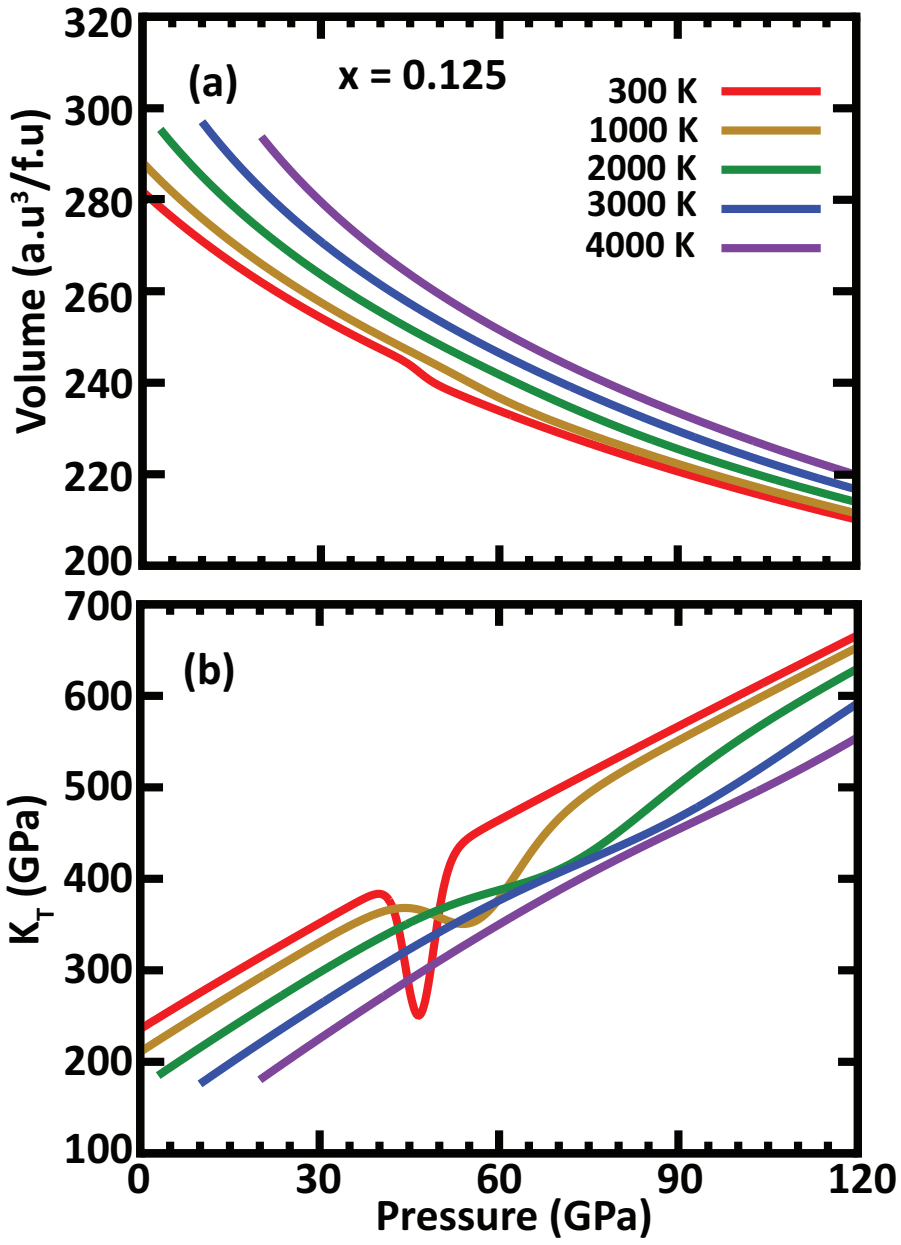

Figure 4.6: Pressure and temperature dependence of (a) volume (per formula unit), and (b) isothermal bulk moduli for $(Mg_{0.90}Fe_{0.10})(Si_{0.90}Fe_{0.10})O_3$ bridgmanite.

$$V_{MS}(T,P) = (1-n)V_{HS}(T,P) + nV_{LS}(T,P), \tag{4.8}$$

where n is the low-spin fraction. The isothermal bulk modulus can be calculated using $K_T(T,P) = -V_{MS}(dP/dV_{MS})$ and is given by

$$\frac{V_{MS}}{K_T} = n\frac{V_{LS}}{K_T^{LS}} + (1-n)\frac{V_{HS}}{K_T^{HS}} - (V_{LS}-V_{HS})\left.\frac{\partial n}{\partial P}\right|_T. \tag{4.9}$$

The HS to LS transition of $[Fe^{3+}]_{Si}$ goes through volume reduction which produces anomalous softening in the bulk modulus (K) across the transition region. The strength of the anomaly depends on the temperature, volume difference ($\Delta V^{HS\rightarrow LS} = V_{LS} - V_{HS}$), and Gibb's free energy difference ($\Delta G^{HS\rightarrow LS} = G_{LS} - G_{HS}$). The value of $\Delta V^{HS\rightarrow LS}$ for 1 mol.% of Fe_2O_3 (i.e., for $x = 0.01$) is approximately ∼-0.15%, which agrees well with the previous first-principles calculations [75, 119] and is fairly comparable to the experimental value of ∼-0.2% [118]. This volume reduction produces a quite significant anomalous softening (∼12%) at 300 K which is smeared out with increasing temperature due to broadening of the spin transition region (Fig. 3.6b). In spite of clear volume reduction across the spin crossover, [119] did not consider the anomalous softening of bulk modulus probably due to very sharp crossover observed in their calculations. However, owing to the considerable broad HS to LS crossover and noticeable volume reduction, as evidenced by experimental observations [118], bulk modulus anomalies may have significant implications for the interpretation of radial and lateral velocity structures of the lower mantle.

4.4.2 Comparison with experimental measurements

Having calculated the compression curves for $(Mg,Fe^{3+})(Si,Fe^{3+})O_3$-bridgmanite, we compare our results with the available experimental measurements. As shown in figure 4.7 (a,b,c), our calculated compression curves for pure $MgSiO_3$, $(Mg_{1-x}Fe_x^{2+})SiO_3$,

and $(Mg_{1-x}Fe^{3+}_x)(Si_{1-x}Fe^{3+}_x)O_3$ agree well with measurements [81, 110, 111, 114, 115, 133]. Compression curves for $0< x <0.125$ are linearly interpolated using $x = 0$ and 0.125 results. Using enstatite powder, *Lin et al., 2012* [76] synthesized bridgmanite sample $(Mg_{0.9}Fe_{0.1})SiO_3$ (Br10) that contains $Fe^{3+}/\sum Fe \approx 20\%$ in the octahedral sites (Si-sites) and $Fe^{2+}/\sum Fe \approx 80\%$ in the pseudododecahedral sites (Mg-sites). Compression curve for this sample at 300 K was recently measured by *Mao et al., 2015* [118]. To compare with measurements by *Mao et al., 2015* [118], we modeled their Br10 sample as

$$\begin{aligned} Br10 = (Mg_{0.9}Fe_{0.1})SiO_3 &= a(Mg_{1-x}Fe^{2+}_x)SiO_{(3)} \\ &+ b(Mg_{1-y-\alpha}Fe^{3+}_y)(Si_{1-y}Fe^{3+}_y)O_{3(1-\beta)}. \end{aligned} \quad (4.10)$$

Figure 4.7(c) shows that the presence of $[Fe^{2+}]_{Mg}$ in bridgmanite does not affect the compression curve significantly. Considering the smaller ionic radius of Fe^{3+} compared to that of Fe^{2+}, $[Fe^{3+}]_{Mg}$ may also not affect the compression curve significantly and dominant changes would be due to the presence of $[Fe^{3+}]_{Si}$ [81]. We calculated the compression curves for our modeled Br10 with $10\% \leq Fe^{3+}_{Si}/\sum Fe \leq 20\%$ (red curve in figure 4.7d). Stoichiometric coefficients in equation 4.10 for 10% $Fe^{3+}_{Si}/\sum Fe$ (lower-bound) are: a = 0.505, b = 0.505, x = 0.15842, y = 0.019802, α = 0.039604, β = 0.019802, and for 20% $Fe^{3+}_{Si}/\sum Fe$ (upper-bound) are: a = 0.51, b = 0.51, x = 0.11765, y = 0.039216, α = 0.078431, β = 0.039217. Figure 4.7(d) shows that compression curve measured by *Mao et al., 2015* [118] (black symbol) tend to agree better with the calculated values for $(Mg_{0.9}Fe^{2+}_{0.1})SiO_3$ (blue curve) in the lower-pressure range, while in the higher-pressure range agreement with our modeled Br10 (red curve) is good. This observation suggests that Fe^{2+} present in the sample at ambient condition may tend to transform into Fe^{3+} with increasing pressure.

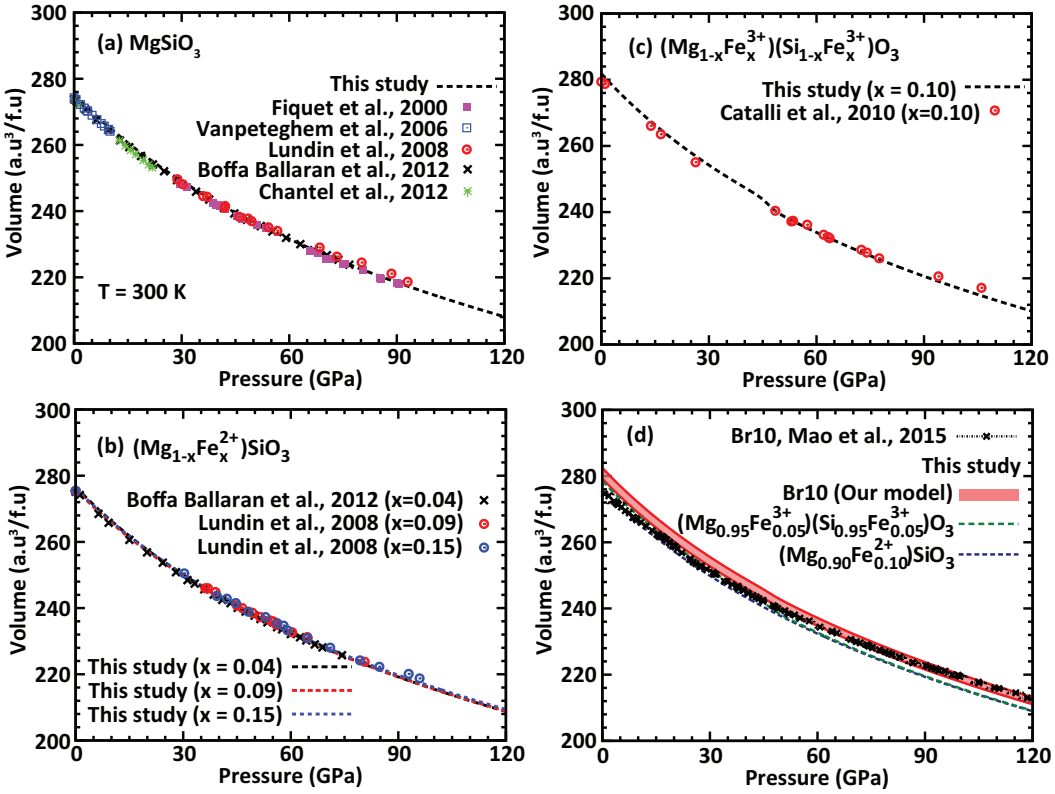

Figure 4.7: 300 K compression curves for (a) $MgSiO_3$, (b) $(Mg_{1-x}Fe_x^{2+})SiO_3$, (c) $(Mg_{1-x}Fe_x^{3+})(Si_{1-x}Fe_x^{3+})O_3$, and (d) bridgmanite with 10 mol.% Fe (Br10). Our first-principles calculations (lines) are compared with experimental measurements (symbols). Br10 sample was synthesized by *Lin et al., 2012* and compression curve was measured by *Mao et al., 2015* (black symbol in Fig. d). In this study, Br10 has been been modeled by balancing the stoichiometry with appropriate molar fractions of $Mg_{1-x}Fe_x^{2+})SiO_3$ and $(Mg_{1-x}Fe_x^{3+})(Si_{1-x}Fe_x^{3+})O_3$ bridgmanite (red filed-curve in Fig. d). Lower- and upper-bound of our model are determined by balancing the stoichiometry with 10% Fe^{3+} and 20% Fe^{3+} in octahedral site (Si-site), respectively.

4.5 Geophysical Significance

Bulk moduli of $(Mg_{1-x}Fe^{3+}_x)(Si_{1-x}Fe^{3+}_x)O_3$ interpolated along the lower mantle geotherm [6] (temperature profile for three relevant model geotherms are displayed in Fig. A.1) for several Fe^{3+} concentrations are shown in Fig. 4.8. For x = 0.125, the strength of bulk modulus softening (about ∼7%) is smaller than that for (Mg,Fe)O (about ∼11%) reported by *Wu et al., 2013* [59] for similar iron concentration. This bulk modulus anomaly reduces rapidly with decreasing in iron concentration and almost disappear for x = 0.02. Based on thermodynamics model, *Xu et al., 2015* [124] estimated the amount of $Fe^{3+}/\sum Fe$ to very small (∼0.01-0.07) in Al-free bridgmanite under lower mantle conditions. Considering this fact, the spin crossover of $[Fe^{3+}]_{Si}$ may not have as noticeable impact on lower mantle properties as was reported by [61] due the (Mg,Fe)O ferropericlase. Nevertheless, the volume reduction due to HS and LS transition of $[Fe^{3+}]_{Si}$ and its associated elastic anomalies should be taken into account while constraining the composition and thermal structure of the Earth's lower mantle.

4.6 Conclusions

We have presented the first-principles LDA + U_{sc} investigation of the spin transition in $(Mg,Fe^{3+})(Si,Fe^{3+})O_3$ bridgmanite. In order to investigate the system close to the experimental conditions, the disordered substitution of Fe^{3+} was considered using Boltzmann distribution of symmetrically inequivalent configurations of nearest neighbor $[Fe^{3+}]_{Mg}$-$[Fe^{3+}]_{Si}$ pairs. Thermal effects were captured properly by calculating the vibrational contribution to free-energy within quasi harmonic approximation. $[Fe^{3+}]_{Si}$ undergoes pressure induced high-spin to low-spin state while $[Fe^{3+}]_{Mg}$ remains in the high-spin state. Disordered distribution of Fe^{3+} does not seem to affect the HS to

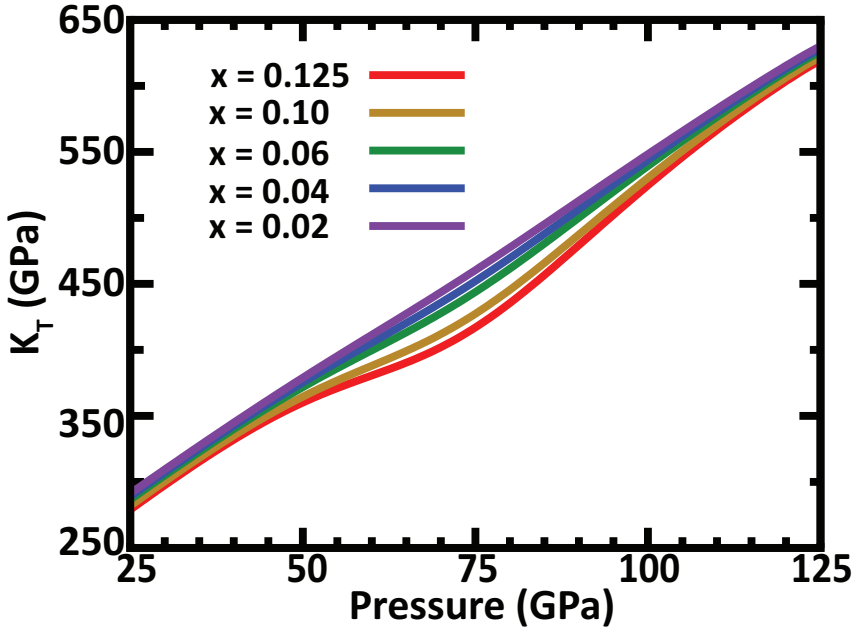

Figure 4.8: Bulk moduli (K_T) for $(Mg_{1-x}Fe_x^{3+})(Si_{1-x}Fe_x^{3+})O_3$ bridgmanite along the Earth's lower mantle geotherm [6] for varying Fe^{3+} concentration.

LS crossover significantly. The transition pressure increases with increasing Fe^{3+} concentration which is consistent with the experimental observations [76, 118]. The spin crossover is also accompanied by significant volume reduction and anomalous decrease of the bulk modulus across the crossover region. Further investigations regarding the effect of spin transition on the elastic properties such as adiabatic bulk moduli, shear moduli, and acoustic velocities would be needed to better understand the the thermal structure and the composition of the Earth's lower mantle.

Chapter 5

Thermoelasticity of Fe^{2+}-bearing bridgmanite

In this chapter, we present LDA+U calculations of high temperature elastic properties of bridgmanite with composition $(Mg_{(1-x)}Fe^{2+}_x)SiO_3$ for $0 \leq x \leq 0.125$. Results of elastic moduli and acoustic velocities for the Mg-end member (x=0) agree very well with the latest high pressure and high temperature experimental measurements. In the iron-bearing system, we focus particularly on the change in thermoelastic parameters across the state change that occurs in ferrous iron above ∼30 GPa, often attributed to a high-spin (HS) to intermediate spin (IS) crossover but explained by first principles calculations as a lateral displacement of substitutional iron in the perovskite cage. We show that the measured effect of this change on the equation of state of this system can be explained by the lateral displacement of substitutional iron, not by the HS to IS crossover. The calculated elastic properties of $(Mg_{0.875}Fe^{2+}_{0.125})SiO_3$ along an adiabatic mantle geotherm, somewhat overestimate longitudinal velocities but produce densities and shear velocities quite consistent with Preliminary Reference Earth Model data throughout most of the lower mantle.

5.1 Introduction

Thermoelastic properties of lower mantle minerals provide a direct link to seismological observations. In order to constrain the composition and thermal structure of the Earth's lower mantle, a detailed investigation of elastic properties of the constituent minerals is needed. Bridgmanite, (Mg,Fe,Al)(Si,Fe,Al)O_3 perovskite (Pv), is the main constituent of the lower mantle along with ferropericlase, (Mg,Fe)O, $CaSiO_3$ perovskite, and (Mg,Fe,Al)(Si,Fe,Al)O_3 post-perovskite (PPv). Although there has been considerable progress in measurements of elastic properties of these minerals at high pressures and temperatures [65, 67, 69, 114, 110, 111, 112, 129, 130, 131, 132, 133, 134, 135, 136], owing to extreme pressure and temperature conditions in the lower mantle the availability of data on Fe-bearing bridgmanite is quite limited to well constrain lower mantle composition and temperature. Several experiments and first-principles calculations have shown that pressure induced iron spin crossover [52, 55, 63, 76] affects elastic properties of (MgFe)O ferropericlase (fp) [53, 56, 57, 58, 59, 61, 62, 128]. In the case of iron-bearing bridgmanite, effects of spin crossover on elastic properties have been quite uncertain due to possible coexistence of ferrous (Fe^{2+}) and ferric (Fe^{3+}) iron along with the more complex perovskite crystal structure. Experimentally, it has been difficult to isolate the effects of ferrous and ferric iron unambiguously.

Acoustic velocity measurements using ultrasonic technique [111] and compression curve measurements [110] in iron-bearing bridgmanite, demonstrated a significant change in bulk modulus across the state change in iron. By fitting experimental data with 3^{rd}-order Birch-Murnaghan equation of state to small (0-40 GPa) and large (0-75 GPa) pressure ranges, *Boffa-Ballaran et al., 2012* [110] found ambient condition bulk modulus smaller (245 GPa) and larger (253 GPa), respectively. Since these fitting pressure ranges had no effect on the iron-free phase, *Boffa-Ballaran et al., 2012* [110] attributed this behavior to change in compression mechanism caused by the high-spin (HS) to

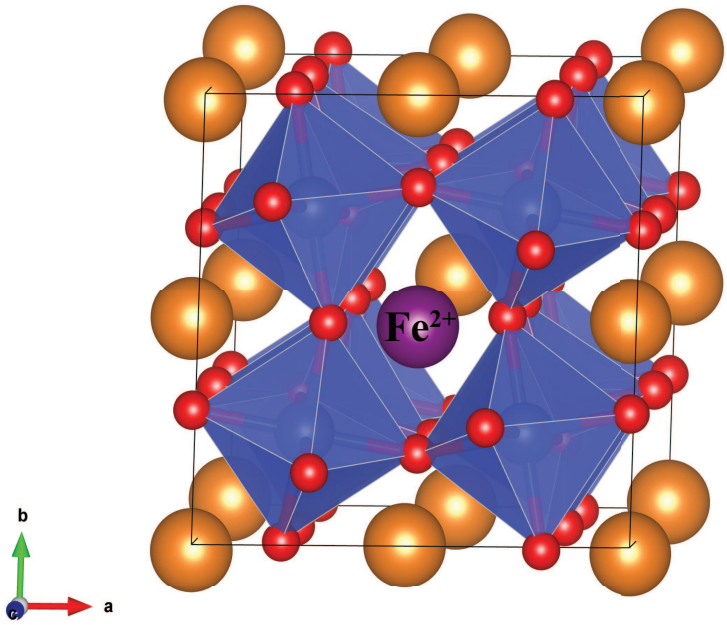

Figure 5.1: Atomic structure Fe^{2+}-bearing $MgSiO_3$ bridgmanite phase. Fe, Mg, O, and Si are represented as purple, orange, red, and blue sphere, respectively.

intermediate-spin (IS) crossover [77]. However the HS to IS crossover has not been found in first-principle studies [60, 72, 74, 75]. Using the local density approximation augmented by the Hubbard type correction (LDA+U) method, *Hsu et al., 2010* [74] showed that iron in Fe^{2+}-bearing bridgmanite should remain in the HS state throughout the lower mantle and should, instead, undergo a pressure induced displacement producing a state with increased iron Mössbauer quadrupole splitting (QS). The calculated low (1.9-2.4 mm/s) and high (3.3-3.9 mm/s) QS states were consistent with experimental measurements [76, 77, 116, 117]. Owing to lack of sufficient experimental measurements on elasticity of iron-bearing bridgmanite, effects of the proposed HS to IS crossover [77] or iron displacement [60, 72, 74, 75] have not been properly understood. To clarify this issue we have calculated the high temperature and high-pressure elastic moduli and acoustic velocities of $(Mg_{1-x}Fe_x)SiO_3$ for x=0 and x=0.125, with iron in low- and

high-QS states. We also compare the effects of the HS to IS transition [60] in the static equation of state of Fe^{2+}-bearing bridgmanite.

Unlike in $(MgFe^{3+})(SiFe^{3+})O_3$ [75], the high-spin (HS) to low-spin (LS) transition in $(MgFe^{2+})SiO_3$ has not been found in the lower-mantle pressure range using the LDA+U method [60, 74]. However, there have been several studies suggesting that HS to LS transition might occur at around $\sim$ 90 GPa [63, 64, 66, 68, 77, 76, 125] and might have consequences for the vibrational spectrum [137]. Recently *Zhang et al., 2014* [138] found that iron-bearing bridgmanite dissociates into nearly iron-free phase and into an iron-rich hexagonal silicate phase in the deep lower mantle. As the dissociation phase boundary is still not well known, we present results for elasticity of Fe^{2+}-bearing bridgmanite with constant iron concentration in the entire pressure range of the lower mantle.

5.2 Method and Calculation Details

We have used density functional theory (DFT) within the local density approximation (LDA) [18] augmented by the Hubbard U (LDA+U) calculated self-consistently [10, 11, 12]. Ultrasoft pseudo-potentials [28] have been used for Fe, Si, and O. For Mg, a norm-conserving pseudo-potential generated by von Barth-Car's method has been used. A detailed description about pseudo-potentials is available in [125]. The plane-wave kinetic energy and charge density cut-off are 40 Ry and 160 Ry, respectively. Structural optimization at arbitrary volumes has been performed using variable cell-shape damped molecular dynamics [13, 14]. Self- and structurally-consistent U_{sc}=3.1 eV, reported by [74] using the linear response approach [10, 11], has been used for high-spin low-QS and high-QS iron. Vibrational density of states (VDoS), needed to calculate free energy within quasi-harmonic approximation (QHA) [120], have been calculated using density functional perturbation theory (DFPT) [121] using the LDA+U functional

[123]. $(Mg_{1-x}Fe_x)SiO_3$ for x=0 and 0.125 have been investigated in a 40-atom supercell. Elastic properties for 0<x<0.125 are linearly interpolated using x=0 and x=0.125 results. Electronic states have been sampled on $2 \times 2 \times 2$ Monkhorst-Pack k-point grid shifted by $(1/2, 1/2, 1/2)$ from the Brillouin Zone origin. VDoS have been obtained by calculating dynamical matrices on a $2 \times 2 \times 2$ q-point grid and interpolating the obtained force constants on a $8 \times 8 \times 8$ q-point grid. The structure for x=0, and x=0.125 with high-QS state have been optimized at twelve pressures between -10 and 150 GPa. The low-QS structure has been optimized up to 60 GPa only. Beyond this pressure unstable phonons appear. To obtain static elastic coefficients (zero temperature), C_{ij}, at each pressure, positive and negative strains of 1% magnitude have been applied and after relaxing the internal degrees of freedom, associated stresses have been calculated. Thermoelastic moduli have been calculated using a semi-analytical approach [51]. This method uses an analytical expression for strain Grüneisen parameters to calculate the thermal contribution to elastic coefficients using the quasi-harmonic approximation. This method allows calculations of thermal elastic coefficients using static values and vibrational density of states for unstrained configurations only. It is almost two orders of magnitude more efficient than the fully numerical method [48, 50], which required vibrational density of states also for strained configurations. It also appears to be more accurate since it avoids numerical differentiation on a reduced number of grid points as well as calculations of VDoS and free energies for strained configurations. The method has been applied successfully to several minerals already [51, 139, 140]. Calculations have been performed using VLab cyberinfrastructure at the Minnesota Supercomputing Institute [127].

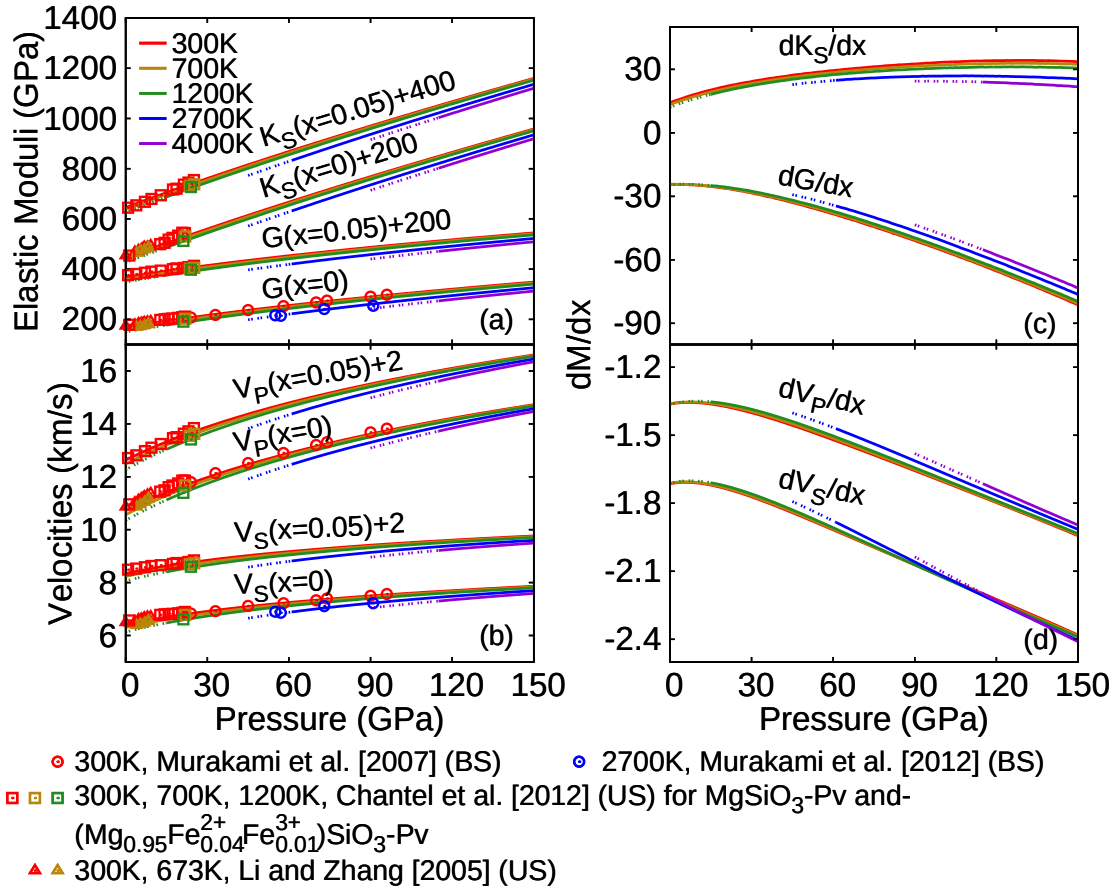

Figure 5.2: Pressure and temperature dependence of elastic moduli and sound velocities for $(Mg_{1-x}Fe_x^{2+})SiO_3$ with x=0 and 0.05 (a, b), and of dM/dx (M= K_S, G, V_P, V_S) (c, d). Solid (dashed) lines represent first-principles results within (outside) the validity of quasi-harmonic approximation. BS: Brillouin scattering, US: Ultrasonic technique.

5.3 Results and Discussion

5.3.1 Elasticity of Iron-free and Fe^{2+}-bearing Bridgmanite

The calculated aggregate elastic moduli, K and G, and acoustic velocities, V_P and V_S, of iron-free bridgmanite compare well with Brillouin scattering measurements of [135, 136] as shown in Fig. 5.2(a) and 5.2(b). Within experimental uncertainties, ultrasonic measurements of [65] and [111] also compare well with our results. Table 5.1 compares calculated elastic properties at zero pressure and 300 K with measurements and simulations at ambient conditions. As compared to experimental measurements, our calculated volume is overestimated by $\sim$ 0.5% while elastic moduli and acoustic velocities are underestimated by $\sim$ 1-3% , which is typical for LDA calculations after including zero-point energy [48, 50]. Calculated pressure derivatives of elastic moduli, K$'$ and G$'$, are 3.96 and 1.79, respectively. Our K$'$ agrees reasonably well with previous studies while G$'$ compares well with those reported by *Sinnelnikov et al., 1998* [132] and *Zhang et al., 2013* [141]. Comparing acoustic velocities and elastic moduli at higher temperatures, especially shear velocities and shear moduli at 2,700 K by *Murakami et al., 2012* [136], we find that the temperature dependence of elastic properties has been captured well. As shown in Fig. 5.3, our calculated $\frac{dK_S}{dT}$ and $\frac{dG}{dT}$ are smaller in magnitude compared to values obtained by ultrasonic [65, 129, 132] at 0 GPa and Brillouin scattering measurements [111] at 22 GPa. Calculated values of $\frac{dK_S}{dT}$ compare well with those of previous calculations [50, 141, 142, 143]. Calculated $\frac{dG}{dT}$ agrees well with Brillouin scattering measurements by *Murakami et al., 2012* [136] and non-self consistent calculation by *Marton and Cohen, 2002* [143] but differs substantially from that of *Wentzcovitch et al., 2004* [50], *Zhang et al., 2013* [141], and *Oganov et al., 2001* [142].

The semi-analytical method used here had produced well the temperature dependence of elasticity for all applied materials [51, 139, 140]. This method has also produced slightly better results for MgO [51] than the fully numerical method [48, 50]. This is because this method avoids calculations of vibrational frequencies in strained configurations and numerical errors associated with finite difference calculations of elastic coefficients.

The elastic moduli and acoustic velocities of iron-bearing bridgmanite at lower mantle pressures are also shown in Fig. 5.2. To compare with measurements of *Boffa-Ballaran et al., 2012* [110] and *Chantel et al., 2012* [111] in the iron-bearing phase, we estimated elastic properties for $0<x<0.125$ by linearly interpolating our calculated results for x=0 and x=0.125. The calculated volume at ambient conditions is in agreement with measurements by *Boffa-Ballaran et al., 2012* [110] for x=0.04 and is smaller by ∼2% when compared with measurements by *Chantel et al., 2012* [111] for x=0.05 (Table 5.1). As shown in Fig. 5.2(b), comparison of calculated acoustic velocities, V_P and V_S, for x=0.05 with the only available experimental measurements for $(Mg_{0.95}Fe^{2+}_{0.04}Fe^{3+}_{0.01})SiO_3$ [111] is also good except for the shear velocity data in the lower pressure range. As seen in Fig. 5.2 (c) and (d) and in Table 5.1, the presence of iron has very little to no effect on bulk modulus, K_S, but shear modulus G softens by ∼2 to 6%, consistent with previous static first-principles studies [114, 144]. The effect of iron on the temperature dependence of acoustic velocities and elastic moduli is not very significant (see Fig. 5.2).

5.3.2 Effect of Pressure Induced Iron Displacement on Elasticity

We have investigated the elastic consequences of the pressure induced iron displacement [60, 74] by calculating thermal elastic moduli and acoustic velocities for x=0.125 with iron in low-QS and high-QS sites. The low-QS structure is stable up to 60 GPa in LDA+U calculations. Above this pressure unstable phonon modes start appearing. As

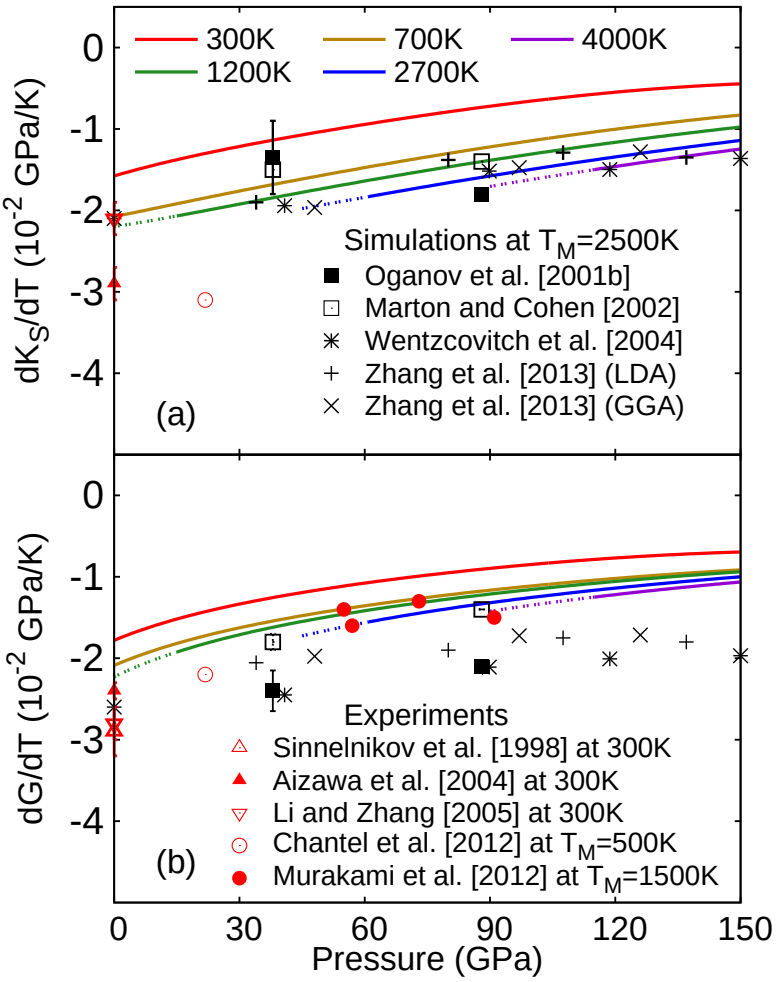

Figure 5.3: Pressure and temperature dependence of (a) $\frac{dK_S}{dT}$, and (b) $\frac{dG}{dT}$ for iron-free bridgmanite. Results from this study (lines) are compared with previous simulations (black symbols) and experimental data (red symbols). The values of $\frac{dK_S}{dT}$ and $\frac{dG}{dT}$ obtained from previous simulations [50, 141, 142, 143] and experimental measurements [111, 136] shown here are calculated at the midpoint between extreme temperatures [i.e., $\frac{dM(P,T_M)}{dT}=\frac{M(P,T_2)-M(P,T_1)}{T_2-T_1}$, where $T_M = \frac{T_1+T_2}{2}$ and M=(K_S, G)]. Error bars on *Oganov et al., 2001* [142] and *Marton and Cohen, 2002* [143] results are reproduced from *Zhang et al., 2013* [141], while on *Wentzcovitch et al., 2004* [50] and *Zhang et al., 2013* [141], they are smaller than the symbols size.

Table 5.1: Volume, sound velocities, elastic moduli and their pressure derivatives at ambient pressure and temperature conditions. BS: Brillouin scattering, US: Ultrasonic, XRD: X-ray diffraction.

$V(A^3)$	x	$V_P(km/s)$	$V_S(km/s)$	K_S(GPa)	G(GPa)	K'	G'	References
163.2	0	10.72	6.42	245.5	168.2	3.96	1.79	This study, single crystal/LDA
163.3	0.05	10.63	6.34	245.8	167.02	4.03	1.79	This study, single crystal/LDA+U (Low-QS)
162.3(0.6)	0	11.04	6.57	264(5)	177(4)	-	-	[131], sinlge-crystal/BS
162.3	0	-	6.51	-	176(5)	-	1.8(0.4)	[132], poly-crystal, US
162.4(0.5)	0	10.84(0.1)	6.47(0.06)	253(5)	173(3)	-	-	[134], poly-crystal/BS
162.4(0.5)	0	10.88(0.06)	6.54(0.03)	253(3)	175(2)	-	-	[134], sinlge-crystal/BS
162.3	0	10.86(0.05)	6.49(0.04)	253(2)	173(1)	4.4(0.1)	2.0(0.1)	[65], poly-crystal/US
-	0	10.85(0.03)	6.49(0.03)	-	172.9(1.5)	-	1.56(0.04)	[136], poly-crystal/BS
162.2(0.2)	0	10.82(0.06)	6.54(0.04)	247(4)	176(2)	4.5(0.2)	1.6(0.1)	[111], poly-crystal/US
166.5(0.2)	0.05	10.60(0.06)	6.46(0.04)	236(2)	174(1)	4.7(0.1)	1.56(0.5)	[111], poly-crystal/US
162.4	0	-	-	267	180	4.10	-	[142], Simulations
162.49	0	-	-	269(2)	159(2)	-	-	[143], Simulations
162.4	0	-	-	250.5	172.9	4.01	1.74	[141], Simulations
Compression Studies								
$V(\AA^3)$				K_T		K'		
162.3	0			259.5		3.69		[133]
162.4	0			248.8		4		[130]
162.7	0.05			255.4		4		[130]
164.1	0			247		3.97		[145], Simulations
162.30	0			255-261		4		[114]
162.18	0.09			257-259		4		[114]
163.30	0.15			257-259		4		[114]
163.09(0.06)	0.04			253(2)		3.99(0.07)		[110], (0-75 GPa)
163.16(0.06)	0.04			245(4)		4.4(0.03)		[110], (0-40 GPa)
166.5(0.2)	0.05			246(2)		4		[111],
163.0	0.09			251(13)		4		[112]

shown in Fig. 5.4, vibrational density of states (VDoS) for x=0 and for x=0.125 with iron in the high-QS and low-QS sites are not very different except for a small shift towards lower frequencies owing to the presence of iron. However, there is an extra peak at $\sim$ 150 cm^{-1} in the VDoS if iron is in the low-QS site. It is worth noting that the vibrational mode associated with this extra peak in the low-QS structure is infra-red active while the same mode is infra-red inactive in the high-QS structure. This information may provide a crucial test to investigate the state of ferrous iron in bridgmanite.

The effect of iron displacement (low-QS to high-QS transition) on unit-cell volume, acoustic velocities, and elastic moduli of iron-bearing bridgmanite with x=0.125 is shown in Fig. 5.5. To quantify the magnitude of the property change, we define the contrast

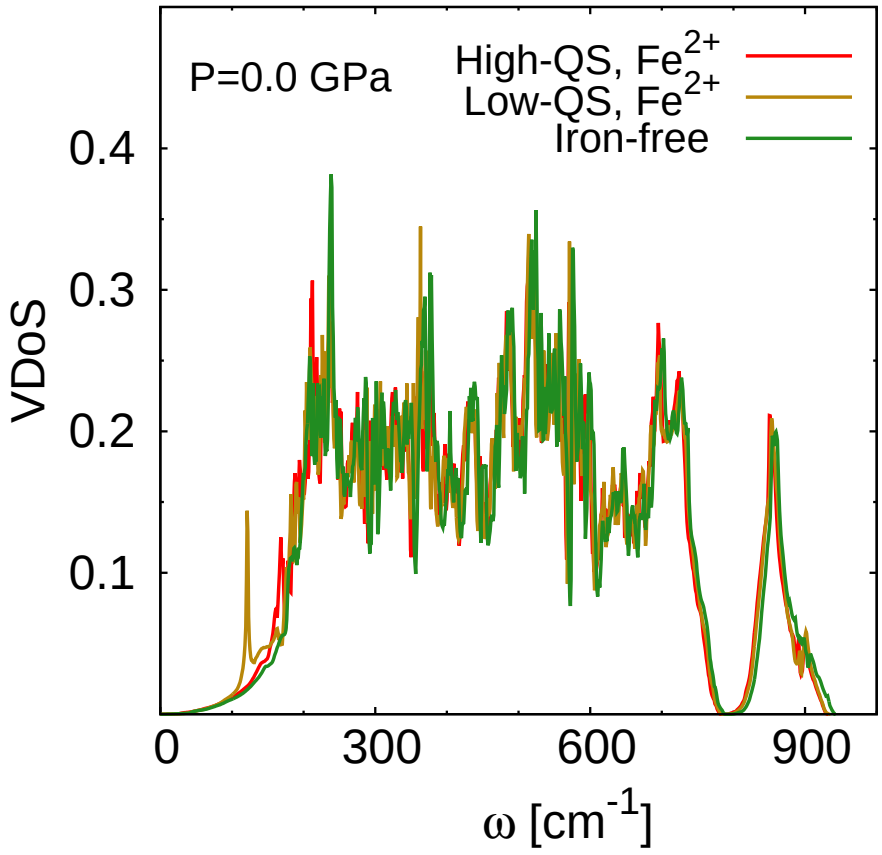

Figure 5.4: Vibrational density of states (VDoS) at $P = 0$ for iron-free bridgmanite using LDA, and for low and high QS state of $(Mg_{0.875}Fe^{2+}_{0.125})SiO_3$ using LDA + U_{sc}.

Table 5.2: Calculated equation of state parameters for Low-QS, High-QS, and combined results at 30 GPa for low-QS and high-QS fitted with different pressure range.

	300K			700K		
	$V(\mathring{A}^3)$	K_T	K'	$V(\mathring{A}^3)$	K_T	K'
Low-QS	163.81	247.16	4.05	165.62	234.05	4.12
High-QS	163.64	248.90	3.97	165.44	236.44	4.03
Combined data (0-150 GPa)	163.81	245.59	4.02	165.62	233.93	4.06
Combined data (0-90 GPa)	163.87	243.41	4.09	165.67	232.32	4.11
Combined data (0-75 GPa)	163.93	241.25	4.15	165.68	232.29	4.12

Δ in a particular property M as $\Delta M = \frac{M_{high-QS} - M_{low-QS}}{M_{low-QS}} \times 100$. As shown in Fig. 5.5, the volume contrast is very small ($\sim$0.1%), consistent with *Boffa-Ballaran et al., 2012* [110] and *Lundin et al., 2008* [114], and is unlikely to be detected in experiments. The contrast in bulk modulus, K_S, and acoustic velocities, V_P and V_S, are also small. However, the shear modulus contrast is about $\sim$0.5-1.5%. This change in G, was also suggested by *Boffa-Ballaran et al., 2012* [110] using spontaneous strain analysis. To investigate the fitting pressure-range behavior observed by *Boffa-Ballaran et al., 2012* [110] and *Chantel et al., 2012* [111] the calculated results for low-QS and high-QS have been combined at 30 GPa, the pressure above which the HS to IS crossover was proposed by *McCammon et al., 2008* [77] and *Potapkin et al., 2013* [117]. The 3^{rd}-order Birch-Murnaghan equation of state was used to fit these combined results. As shown in Table 5.2, depending on the pressure-range of the combined results, an isothermal bulk modulus softening of $\sim$3 to 7 GPa has been found. This softening, however, reduces with increasing temperature.

Intermediate spin (IS) states of the iron in Fe^{2+}-bearing bridgmanite are energetically unfavored in the lower mantle pressure-range [60, 74] and phonon calculations have been extremely difficult for these states. To understand the overall trend of fitting parameters of combined low-QS and IS data, we have used static data for low-QS state and IS state with QS value 0.9-1.6 mm/s [60]. The static bulk modulus at zero pressure for low-QS and IS states are 263.2 GPa and 254.1 GPa, respectively. When static low-QS and IS results have been combined at 30 GPa and fitted within different pressure-ranges of 0-150 GPa and 0-120 GPa, static bulk modulus of the combined fit are 305 GPa and 348.7 GPa, respectively. The fitting pressure-range trend of combined low-QS and high-QS is the same as that observed by *Boffa-Ballaran et al., 2012* [110] and *Chantel et al., 2012* [111] while of combined low-QS and IS states the fitting trend is opposite. These findings substantiate our understanding that ferrous iron in perovskite

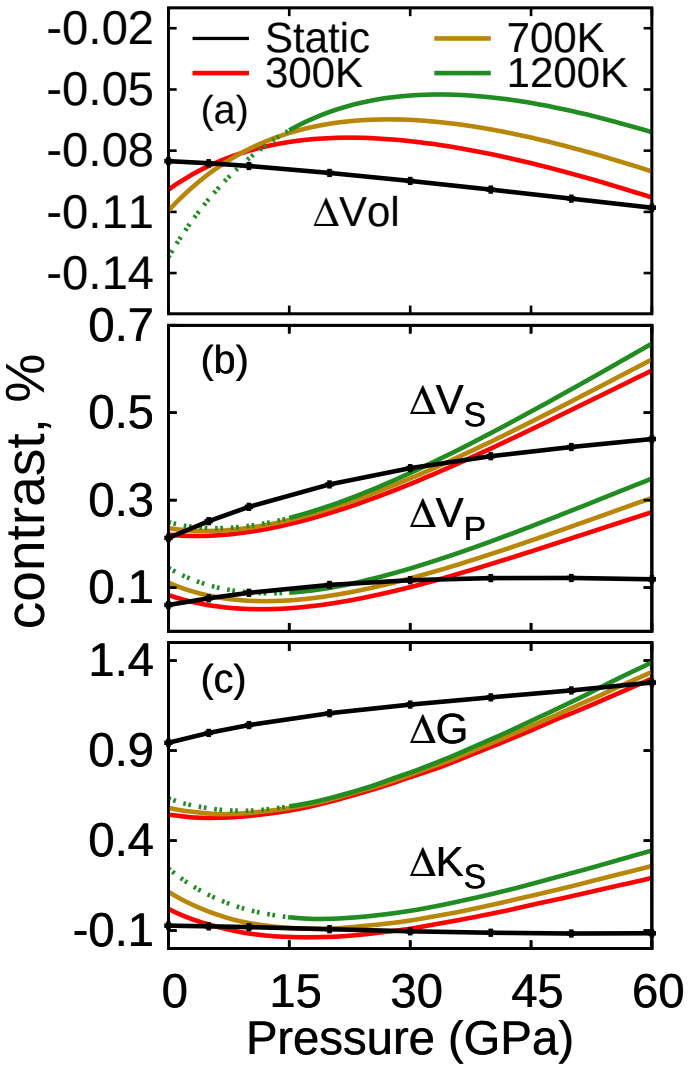

Figure 5.5: Contrast (ΔM) in (a) unit-cell volume, (b) compressional and shear velocity (V_P, V_S), and (c) bulk and shear modulus (K_S, G) between low-QS and high-QS states in $(Mg_{0.875}Fe^{2+}_{0.125})SiO_3$ pereovskite.

remains in the HS state in the lower mantle pressure range, but instead, undergoes a horizontal displacement in the perovskite cage which results in an increase in Mössbauer quadrupole splitting.

5.4 Geophysical Significance

As shown in Fig. 5.6, elastic moduli (K_S, G), acoustic velocities (V_P, V_S), and densities (ρ) are calculated along the Boehler's geotherm [6] (temperature profile for three relevant model geotherms are displayed in Fig. A.1) using new [51] and previous [48, 50] methods and the results are compared with seismic values from the Preliminary Reference Earth Model (PREM) [1]. Owing to the smaller magnitude of $\frac{dG}{dT}$ obtained here, present results for G and Vs differ more from previous results by *Wentzcovitch et al., 2004* [50] in the deep lower mantle region, where temperatures are higher. This difference is sufficient to alter conclusions regarding mantle composition. Inclusion of 12.5% Fe^{2+} in $MgSiO_3$ perovskite produces good agreement of ρ, V_S, and G with PREM values (Fig. 5.6c,d). Therefore, comparison of calculated V_S with PREM's V_S may indeed suggest a more perovskitic lower manle [136]. However, relatively large values of K_S and V_P are found, suggesting that the lower mantle may accommodate a reasonable amount of ferropericlase, (MgFe)O, and $CaSiO_3$ pereovskite as previously indicated [50]. Resolving whether the lower mantle composition is pyrolytic or perovskitic still needs more detailed investigations of the effect of Al_2O_3 and Fe_2O_3 on the elasticity of bridgmanite along with the elasticity of $CaSiO_3$ perovskite. Ultimately, the analysis of one dimensional velocity profiles might be too limited to address this question more conclusively. Analysis of lateral heterogeneities, including effects of spin crossovers in (MgFe)O and in bridgmanite might prove more useful to address this question.

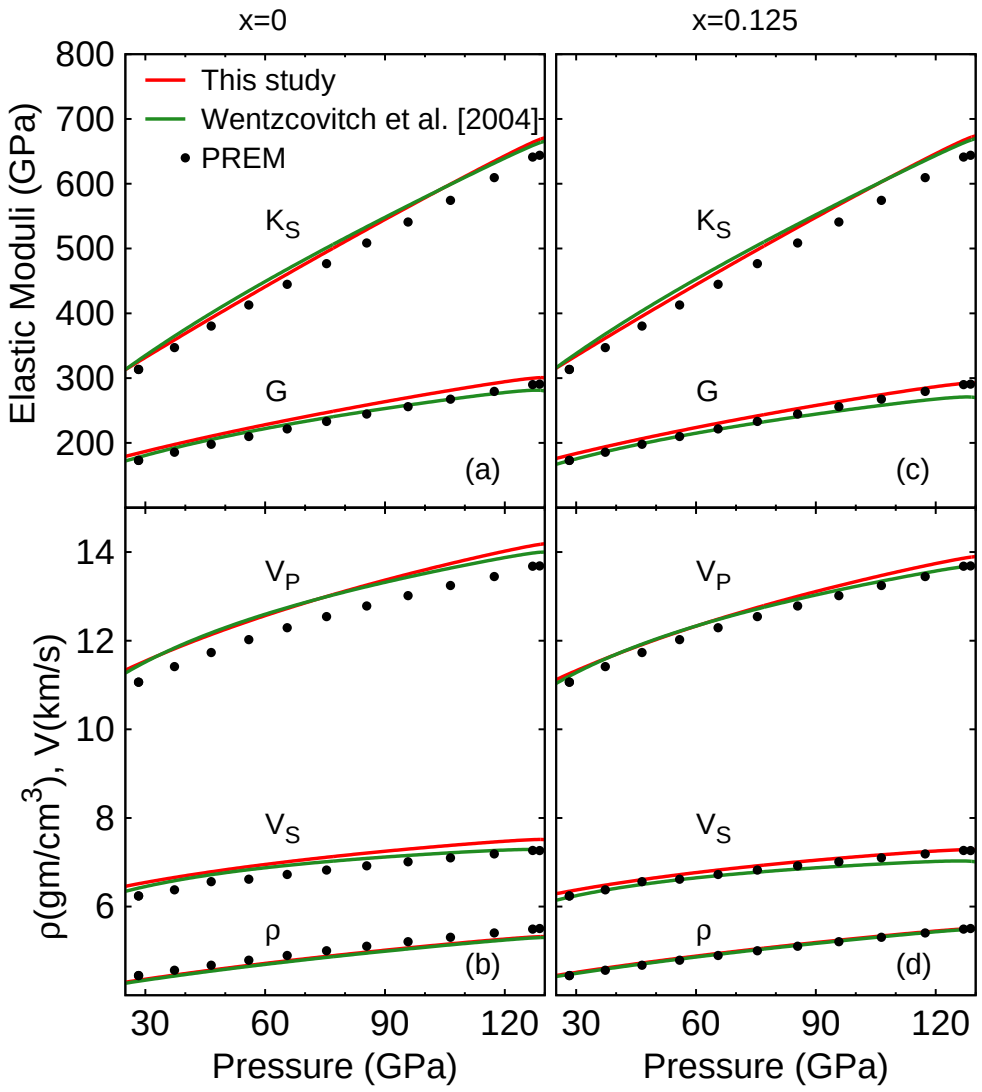

Figure 5.6: Elastic moduli (K_S, G), sound velocities (V_P, V_S), and density (ρ) for $(Mg_{1-x}Fe_x^{2+})SiO_3$ pereovskite with x=0 (a, b) and x=0.125 (c, d) calculated along the Boehler's geotherm [6] using present [51] and previous [50] methods.

5.5 Conclusions

We have presented first-principles LDA + U_{sc} calculations of aggregate elastic moduli and acoustic velocities for Fe^{2+}-bearing bridgmanite at lower mantle conditions. Using the new semi-analytical approach for high temperature elasticity [51], we find an unexpected difference of temperature gradients with respect to previous fully numerical calculations [50] also based on the quasi-harmonic approximation. New results for $\frac{dG}{dT}$ and $\frac{dV_S}{dT}$ for iron-free bridgmanite are in good agreement with the latest high temperature high pressure measurements of these quantities by *Murakami et al., 2012* [136], which also differ from previous calculations and previous experiments. Overall, it appears that pressure and temperature gradients of bulk and shear moduli are better estimated now. Calculated acoustic velocities for iron-bearing bridgmanite also agree well with ultrasonic measurements of *Chantel et al., 2012* [111]. We do not find any significant effect of iron-site change (low-QS to high-QS) on sound velocities and elastic moduli, except for $\sim$1% increase in shear modulus, consistent with findings by *Boffa-Ballaran et al., 2012* [110]. Effects of fitting combined data for low-QS and high-QS states on elastic properties are consistent with previously observed fitting pressure-range behavior [110, 111]. Calculated shear modulus and shear velocities of bridgmanite along a typical mantle geotherm are qualitatively more consistent with PREM values now compared with previous first principles results [50]. Differences in bulk modulus and longitudinal velocities remain noticeable.

Chapter 6

Thermoelasticity of Al^{3+} and Fe^{3+}-bearing bridgmanite

In this chapter, we present a quasi-harmonic local density approximation augmented by the Hubbard type correction (LSDA+U_{sc}) calculations of thermoelastic properties of ferric iron (Fe^{3+})- and aluminum (Al^{3+})-bearing bridgmanite ($MgSiO_3$ perovskite), the main Earth forming phase, at relevant pressure and temperature conditions and compositions. Three charge-coupled substitutions, namely, $[Al^{3+}]_{Mg}$-$[Al^{3+}]_{Si}$, $[Fe^{3+}]_{Mg}$-$[Fe^{3+}]_{Si}$, and $[Fe^{3+}]_{Mg}$-$[Al^{3+}]_{Si}$ have been investigated. Aggregate elastic moduli and sound velocities are successfully compared with limited experimental measurements available. In the case of $[Fe^{3+}]_{Mg}$-$[Fe^{3+}]_{Si}$ substitution, the pressure induced high-spin (S=5/2) to low-spin (S=1/2) transition of $[Fe^{3+}]_{Si}$ passes through a volume collapse and produces elastic anomalies across the transition region. However, this spin transition and associated anomalies would disappear with the presence of aluminum as in $[Fe^{3+}]_{Mg}$-$[Al^{3+}]_{Si}$ substitution. Calculated elastic properties along a lower mantle model geotherm suggests that overall elastic features of simultaneous substitution of Fe_2O_3 and Al_2O_3 in $MgSiO_3$ are similar to that of $(Mg,Fe^{2+})SiO_3$ bridgmanite.

6.1 Introduction

Aluminum (Al) and iron (Fe)-bearing bridgmanite (br), (Mg,Fe,Al)(Si,Fe,Al)O_3 perovskite, is the dominant mineral of the Earth's lower mantle along with (Mg,Fe)O ferropericlase (fp), $CaSiO_3$ perovskite, and (Mg,Fe,Al)(Si,Fe,Al)O_3 post-perovskite (PPv). In order to unravel the composition and thermal structure of the lower mantle, a very good estimate of thermal and elastic properties of these constituents minerals is required. In spite of the considerable experimental [65, 67, 69, 114, 110, 111, 112, 129, 130, 131, 132, 133, 134, 135, 136] and computational effort [48, 49, 50, 51, 57, 59, 79, 80, 128, 141, 142, 143, 144, 145], the available data on high pressure and high temperature elastic properties of these minerals is still quite limited due to ack of sufficient understanding of the physics and chemistry of these minerals under extreme pressure and temperature conditions typical of the Earth's lower mantle. In the case of Al- and Fe-bearing bridgmanite (br), the elasticity data base is even more limited due to uncertainties associated with the possible coexistence of ferrous (Fe^{2+}) and ferric (Fe^{3+}) iron and their pressure induced state change. Moreover, the uncertainties associated with the site occupancy of aluminum and iron in the perovskite structure make the measurements and calculations of elastic properties of Al- and Fe-bearing bridgmanite even more challenging.

It has been shown that the iron in (Mg,Fe)O ferropericlase undergoes a pressure induced spin crossover from high-spin (S=2) to low-spin (S=0) state and affects elastic properties [52, 53, 55, 56, 57, 58, 59, 61, 62, 63]. Similarly, the ferric iron at Si-site, $[Fe^{3+}]_{Si}$, in the Fe-bearing bridgmanite also goes through the pressure induced high-spin (S=5/2) to low-spin (S=1/2) state change [3, 63, 73, 75, 76, 81, 101, 113, 118, 119, 124]. In Chapter 4, it has been shown that the spin-state change of $[Fe^{3+}]_{Si}$ also goes through a noticeable volume collapse across the transition region producing the anomalous softening of the bulk modulus. These anomalies may have significant impact

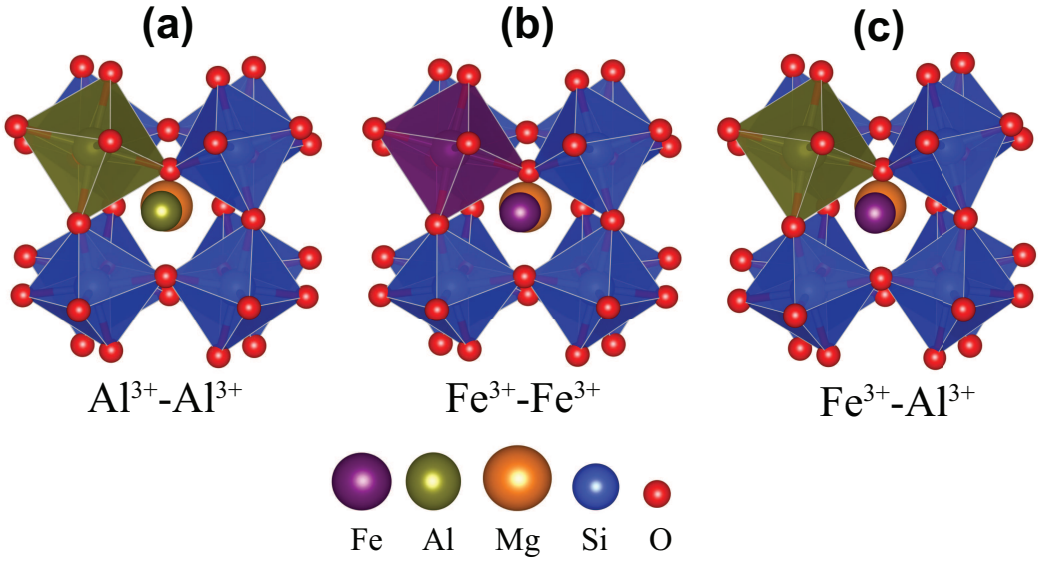

Figure 6.1: (a) Atomic structure of Al^{3+}- and Fe^{3+}-bearing bridgmanite with charge-coupled substitutions (a) $[Al^{3+}]_{Mg}$-$[Al^{3+}]_{Si}$, (b) $[Fe^{3+}]_{Mg}$-$[Fe^{3+}]_{Si}$, and (c) $[Fe^{3+}]_{Mg}$-$[Al^{3+}]_{Si}$. Fe,Al, Mg, Si, and O are represented as purple, green, orange, blue, and red sphere, respectively.

on the lower mantle properties. Experimental observations on Al-bearing bridgmanite (Al^{3+}-br) suggest that Al^{3+} occupies the lattice through charge-coupled substitutions as $[Al^{3+}]_{Mg}$-$[Al^{3+}]_{Si}$ [67, 69, 130]. In the case of simultaneous substitution of Al^{3+} and Fe^{3+} in bridgmanite (Fe^{3+}-Al^{3+}-br), *Hsu et al., 2012* [88] reported that $[Fe^{3+}]_{Mg}$-$[Al^{3+}]_{Si}$ substitution is energetically favored, wherein $[Fe^{3+}]_{Mg}$ remains in the HS state (S=5/2) in the entire lower mantle pressure range. Owing to the extremely high pressure and temperature conditions, experimental observations of the anomalous nature of elastic moduli and acoustic velocities of Fe^{3+}-bearing bridgmanite are still not available. In an effort to understand the elastic consequences of spin-state transition of $[Fe^{3+}]_{Si}$, a first-principles calculation for thermoelastic properties of the Fe^{3+}-br and Al^{3+}-br is presented here.

6.2 Computational details

Owing to the strong correlation of iron's $3d$ electrons, we have used the density functional theory augmented by the Hubbard type correction (DFT+U method) within the local density approximation (LDA) [18]. Three charge-coupled substitutions of Al^{3+} and Fe^{3+} (shown in Fig. 6.1): $(Mg_{1-x}Al_x)(Si_{1-x}Al_x)O_3$, $(Mg_{1-x}Fe_x)(Si_{1-x}Fe_x)O_3$, and $(Mg_{1-x}Fe_x)(Si_{1-x}Al_x)O_3$ bridgmanite for $x = 0.125$ have been investigated. Elastic moduli and density for other concentration in the range $0<x<0.125$ have been linearly interpolated using the calculated data for $x = 0$ and $x = 0.125$. All calculations are performed in a 40-atom super-cell. Ultrasoft pseudo-potentials [28] have been used for Al, Fe, Si, and O. For Mg, a norm-conserving pseudo-potential generated by von Barth-Car's method has been used. A detailed description of these pseudo-potentials has been reported by *Umemoto et al., 2008* [125]. The plane-wave kinetic energy and charge density cut-off are 40 Ry and 160 Ry, respectively. For all three configurations mentioned above, the electronic states have been sampled on a shifted $2\times2\times2$ k-point grid [20]. The equilibrium geometry at any arbitrary pressure has been optimized using the variable cell-shape damped molecular dynamics (VCS-MD) [13, 14]. Thermal effects have been addressed within the quasiharmonic approximation (QHA). The vibrational density of states (VDOS) for QHA have been computed using the density functional perturbation theory (DFPT) [123] within the LDA+U_{sc} approximation for the exchange-correlation energy functional.

Aggregate elastic moduli and acoustic velocities were calculated for $[Al^{3+}]_{Mg}$-$[Al^{3+}]_{Si}$, $Fe^{3+}]_{Mg}$-$[Fe^{3+}]_{Si}$, and $[Fe^{3+}]_{Mg}$-$[Al^{3+}]_{Si}$ substitutions using Wu and Wentzcovitch method [51]. For this purpose, equilibrium structures were obtained at 10-12 pressure points in the relevant pressure-range and dynamical matrices at each pressure points were calculated using DFPT in a $2 \times 2 \times 2$ q-point grid. Thus obtained force constants from dynamical matrices were interpolated in a $8 \times 8 \times 8$ q-point grid to obtain VDOS. In

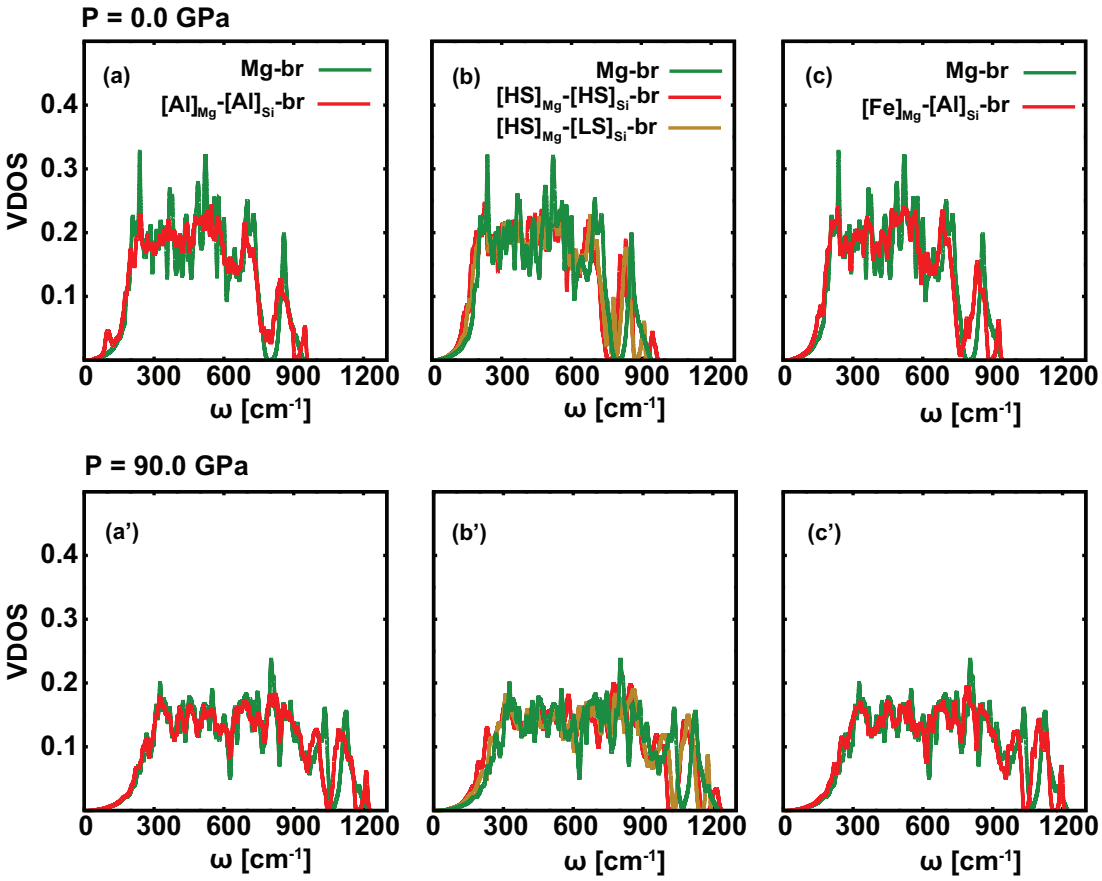

Figure 6.2: Vibrational density of states (VDOS) for (a, d) $(Mg_{0.875}Al_{0.125})(Si_{0.875}Al_{0.125})O_3$ ($[Al]_{Mg}$-$[Al]_{Si}$-br), (b, e) $(Mg_{0.875}Fe_{0.125})(Si_{0.875}Fe_{0.125})O_3$ ($[HS]_{Mg}$-$[HS]_{Si}$-br, $[HS]_{Mg}$-$[LS]_{Si}$-br), and (c, f) $(Mg_{0.875}Fe_{0.125})(Si_{0.875}Al_{0.125})O_3$ bridgmanite ($[Fe]_{Mg}$-$[Al]_{Si}$-br) compared with that of $MgSiO_3$ (Mg-br) at P = 0.0 GPa and 90.0 GPa. $[HS]_{Mg}$-$[HS]_{Si}$-br and $[HS]_{Mg}$-$[LS]_{Si}$-br represent the high- and the low-spin state of ferric iron (Fe^{3+}) at the Si-site in $[Fe]_{Mg}$-$[Fe]_{Si}$-br.

Fig. 6.2, representatives of the calculated VDOS for each substitutions and their comparison with that of pure $MgSiO_3$ bridgmanite (Mg-br) at 0 and 90 GPa are shown. By increasing the pressure, inter-atomic forces become stronger resulting in the spread of VDOS to larger frequency range (Fig. 6.2 a', b', and c'). The static (zero temperature) elastic constants, C_{ijkl}^{static}, needed for Wu and Wentzcovitch method, were obtained at each pressure point by applying small $\pm 1\%$ strains (this choice for the value of applied strain is small enough to maintain the linear regime for stress and strain relation $\sigma_{ij} = \sum C_{ijkl}\epsilon_{kl}$ and large enough to avoid numerical errors) and calculating the associated stresses after relaxing the internal degrees of freedom. Owing to the orthorhombic crystal symmetry, bridgmanite mineral has nine independent elastic constants (i.e., C_{11}, C_{22}, C_{33}, C_{44}, C_{55}, C_{66}, C_{12}, C_{13}, C_{23} in Voigt notation) and the aggregate bulk (K) and shear modulus (G) have been estimated by computing Voigt-Reuss-Hill averages. Using the values of K and G along with the high temperature equation of states (for density, ρ), we obtained the pressure and temperature dependent acoustic velocities (compressional velocity, V_P, shear velocity, V_S, and bulk velocity, V_Φ).

6.3 Results and discussion

6.3.1 Elasticity of $[Al^{3+}]_{Mg}$-$[Al^{3+}]_{Si}$-bearing bridgmanite

The pressure dependence of elastic moduli, acoustic velocities, and density for pure $MgSiO_3$ and Al-bearing bridgmanite at several temperatures are shown in Fig. 6.3. A very good agreement with the experimental measurements of our calculated elastic moduli and acoustic velocities for pure $MgSiO_3$ bridgmanite (Mg-br) [65, 111, 135], especially shear velocities and shear moduli at 2700 K by *Murakami et al., 2012* [136] (Fig. 6.3 a, a$'$), shows that our first-principles calculations provide a robust estimate for elastic properties of minerals at the extreme pressure and temperature conditions

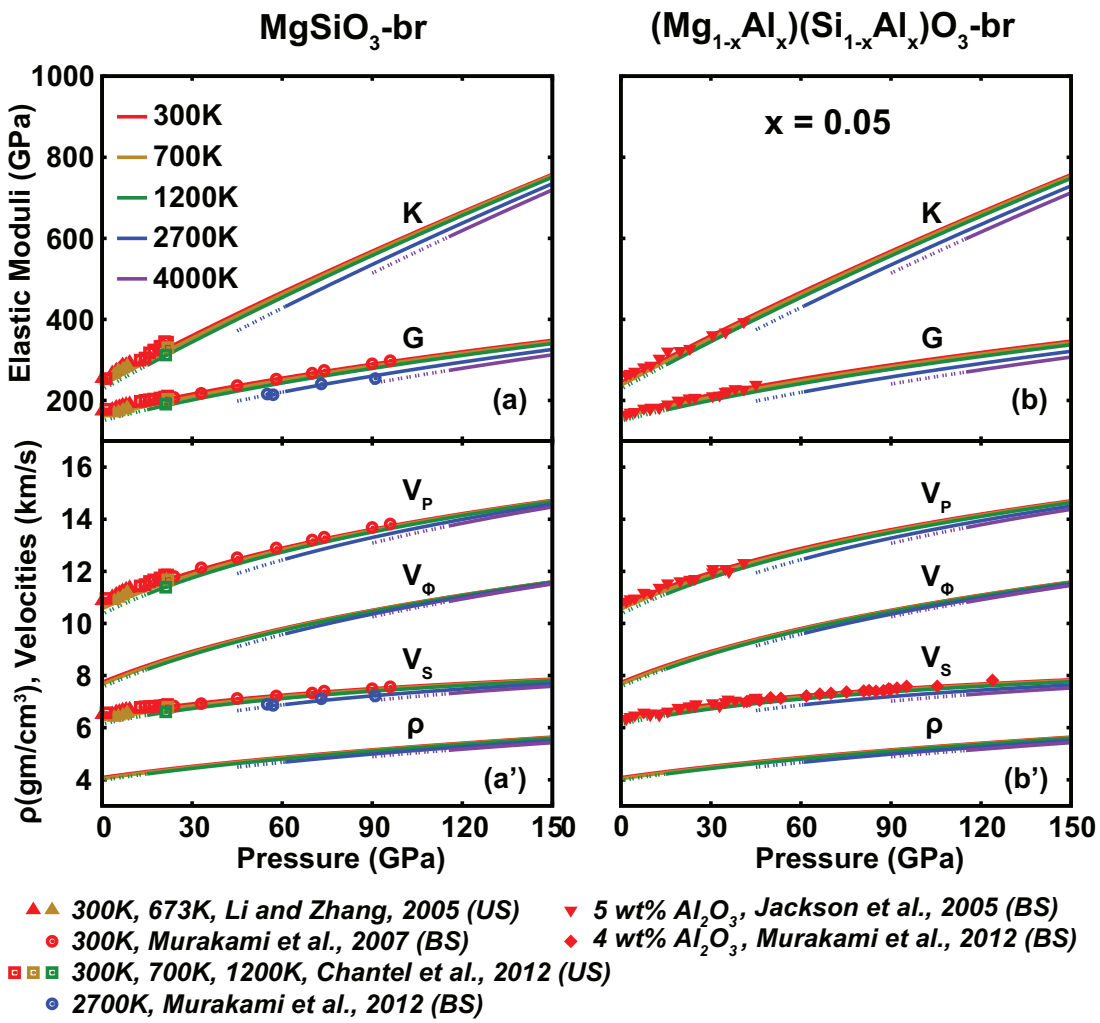

Figure 6.3: Pressure and temperature dependence of elastic moduli (bulk modulus K, and shear modulus G) and acoustic velocities (compressional velocity V_P, shear velocity V_S, and bulk velocity V_Φ) for (a,a') pure $MgSiO_3$ and (b,b') $(Mg_{0.95}Al_{0.05})(Si_{0.95}Al_{0.05})O_3$ bridgmanite. Our calculated results within LDA (lines) are compared with available experimental measurements (symbols). Solid (dashed) lines represent first-principles results within (outside) the validity of quasi-harmonic approximation. BS: Brillouin scattering, US: ultrasonic technique.

typical of the Earth's lower mantle. Our calculated data for $(Mg_{-1x}Al_x)(Si_{1-x}Al_x)O_3$ bridgmanite with $x = 0.05$ at 300 K also compare very well with the room temperature experimental measurements by *Jackson et al., 2005* [69] and *Murakami et al., 2012* [136] for Al-bearing sample that contains ∼5 wt% and ∼4 wt% of Al_2O_3, respectively (Fig. 6.3 b, b′). Overall trend of Al_2O_3 substitution at 300 K is consistent with the previous experimental observations[67, 69, 136].

6.3.2 Elasticity of $[Fe^{3+}]_{Mg}$-$[Fe^{3+}]_{Si}$ and $[Fe^{3+}]_{Mg}$-$[Al^{3+}]_{Si}$-bearing bridgmanite

Having successfully calculated the elastic properties for pure and Al-bearing bridgmanite, we now investigate the elastic consequences of the pressure induced high-spin (HS) to low-spin (LS) transition of $[Fe^{3+}]_{Si}$ in $(Mg_{1-x}Fe_x)(Si_{1-x}Fe_x)O_3$. For this purpose, we calculate the elastic properties of the system in the mixed spin (MS) state of pure HS and LS state by extending the approach of *Wu et al., 2013* [59]. The molar Gibb's free energy for the system (under stress σ) in the MS state is given by

$$G(P,T,n,\sigma) = nG_{LS}(P,T,\sigma) + (1-n)G_{HS}(P,T,\sigma) + G^{mix}(P,T,\sigma), \tag{6.1}$$

where $n(P,T,\sigma)$ is the low-spin fraction (eq. 4.7), T is temperature, P is pressure, $G_{LS/HS}$ is the free energy for pure HS/LS state, and G^{mix} is the mixing free energy for ideal solid solution of HS and LS states of $[Fe^{3+}]_{Si}$. Then, the elastic compliances S^{ij} can be calculated as

$$S^{ij} = -\frac{1}{V}\frac{\partial^2 G}{\partial\sigma_i\partial\sigma_j}\bigg|_{P,T}. \tag{6.2}$$

The derivative of G with respect to σ is computed from eq. 6.1

$$\frac{\partial G}{\partial\sigma_i} = n\frac{\partial G_{LS}}{\partial\sigma_i} + (1-n)\frac{\partial G_{HS}}{\partial\sigma_i} + (G_{LS}-G_{HS})\frac{\partial n}{\partial\sigma_i} + \frac{\partial G^{mix}}{\partial\sigma_i}. \tag{6.3}$$

However, at equilibrium

$$\frac{\partial G}{\partial n} = \left[(G_{LS} - G_{HS})\frac{\partial n}{\partial \sigma_i} + \frac{\partial G^{mix}}{\partial \sigma_i}\right]\frac{\partial \sigma_i}{\partial n} = 0. \tag{6.4}$$

In eq. 6.4, the derivative $\frac{\partial \sigma_i}{\partial n} \neq 0$ ensures that

$$(G_{LS} - G_{HS})\frac{\partial n}{\partial \sigma_i} + \frac{\partial G^{mix}}{\partial \sigma_i} = 0. \tag{6.5}$$

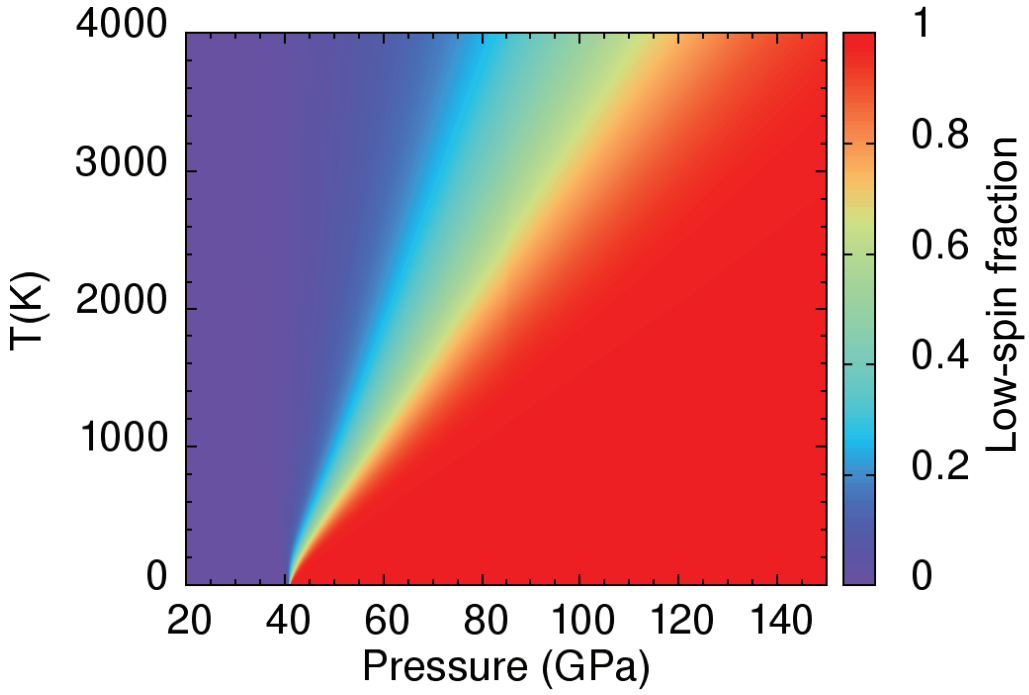

Figure 6.4: Pressure and temperature dependence of low-spin fraction, n(P,T), of $[Fe^{3+}]_{Si}$ in $(Mg_{1-x}Fe_x)(Si_{1-x}Fe_x)O_3$ bridgmanite with $x = 0.125$.

Elastic compliances for the system in MS state are

$$S^{ij}V = nS^{ij}_{LS}V_{LS} + (1-n)S^{ij}_{HS}V_{HS} + \left(\frac{\partial G_{HS}}{\partial \sigma_i} - \frac{\partial G_{LS}}{\partial \sigma_i}\right)\frac{\partial n}{\partial \sigma_j}, \tag{6.6}$$

where volume V in MS state is calculated using $V = nV_{LS} + (1-n)V_{HS}$. The last term in the above equation (6.6) is responsible for the elastic anomalies due the HS to LS transition. Using the relation

$$\frac{\partial}{\partial \sigma_i} \equiv \frac{\partial}{\partial P}\frac{\partial P}{\partial \sigma_i} = \frac{1}{3}\frac{\partial}{\partial P}, \tag{6.7}$$

for $i = 1 - 3$ and assuming that the response of low-spin fraction to the shear stress is negligible, i.e., $\frac{\partial n}{\partial \sigma_4} = \frac{\partial n}{\partial \sigma_5} = \frac{\partial n}{\partial \sigma_6} \approx 0$, the elastic compliances for the orthorhombic system are:

$$S^{ij}V = nS^{ij}_{LS}V_{LS} + (1-n)S^{ij}_{HS}V_{HS} - \frac{1}{9}(V_{LS} - V_{HS})\frac{\partial n}{\partial P} \tag{6.8}$$

for $i, j = 1 - 3$ and

$$S^{ii}V = nS^{ii}_{LS}V_{LS} + (1-n)S^{ii}_{HS}V_{HS} \tag{6.9}$$

for $i = 4 - 6$. The elastic constants, C_{ij}, are obtained by inverting the compliance matrix $\mathbf{S}$:

$$C_{ij} = \left[\mathbf{S}^{-1}\right]^{ij}. \tag{6.10}$$

The pressure and temperature dependence of calculated low-spin fraction, $n(P,T)$, of $[Fe^{3+}]_{Si}$ in $(Mg_{1-x}Fe_x)(Si_{1-x}Fe_x)O_3$ bridgmanite for $x = 0.125$ is shown in Fig. 6.4. Fig. 6.5(a,a') depicts the calculated elastic moduli, acoustic velocities, and density for $x = 0.05$. The HS to LS transition of $[Fe^{3+}]_{Si}$ produces anomalous softening in the bulk modulus (K) across the transition region and this anomalous behavior is also reflected in the compressional (V_P) and the bulk velocity (V_Φ). The strength of anomaly depends on the temperature, volume difference ($\Delta V^{HS\rightarrow LS} = V_{LS} - V_{HS}$), and Gibb's free energy difference ($\Delta G^{HS\rightarrow LS} = G_{LS} - G_{HS}$). The value of $\Delta V^{HS\rightarrow LS}$ per 1% of Fe_2O_3 (i.e., for $x = 0.01$) is approximately ∼-0.15% (Fig. 4.6), which is in good agreement with the previous first-principles calculations [75, 119] and is fairly comparable to the experimental value of ∼-0.2% [118]. This volume reduction causes a quite significant anomalous softening (∼12% at 300 K) in the bulk modulus while the shear modulus increases only in small amount (∼0.5% at 300 K) across the transition region.

Effects of aluminum (Al) on the spin transition of Fe^{3+} was previously studied by *Hsu et al., 2012* [88] using first-principles static calculations within the LDA+U_{sc}

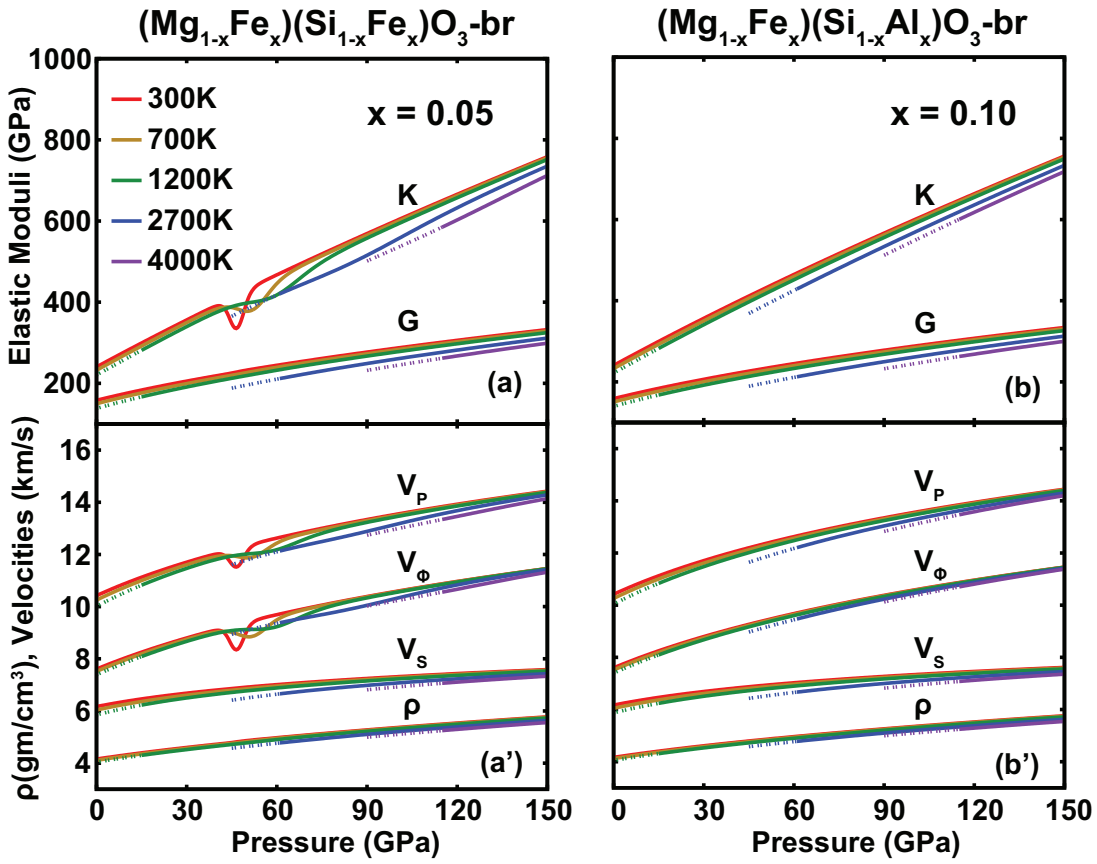

Figure 6.5: Pressure and temperature dependence of elastic moduli (bulk modulus K, and shear modulus G) and acoustic velocities (compressional velocity V_P, shear velocity V_S, and bulk velocity V_Φ) for (a,a') $(Mg_{0.95}Fe_{0.05})(Si_{0.95}Fe_{0.05})O_3$ and (b,b') $(Mg_{0.90}Fe_{0.10})(Si_{0.90}Al_{0.10})O_3$ bridgmanite. Solid (dashed) lines represent first-principles results within (outside) the validity of quasi-harmonic approximation.

Table 6.1: Calculated volume (V), elastic moduli (K, G) and their pressure derivatives (K', G') at ambient pressure and temperature conditions.

	$V(\AA^3)$	K (GPa)	K'	G (GPa)	G'	References
$MgSiO_3$	163.2	245.5	3.96	168.2	1.79	*Shukla et al., 2015*
$(Mg_{0.875}Fe^{2+}_{0.125})SiO_3$	163.7	246.7	4.03	165.2	1.80	*Shukla et al., 2015*
$(Mg_{0.875}Al^{3+}_{0.125})(Si_{0.875}Al^{3+}_{0.125})O_3$	164.1	242.5	4.06	162.7	1.85	*This study*
$(Mg_{0.875}Fe^{3+}_{0.125})(Si_{0.875}Fe^{3+}_{0.125})O_3$	168.1	233.6	4.05	143.4	1.88	*This study*
$(Mg_{0.875}Fe^{3+}_{0.125})(Si_{0.875}Al^{3+}_{0.125})O_3$	165.3	239.4	4.05	156.4	1.83	*This study*

approximation for the exchange-correlation energy functional and the change-coupled $[Fe^{3+}]_{Mg}$-$[Al^{3+}]_{Si}$ substitution was found to be energetically favorable. Therefore, we have chosen this substitution to investigate the elastic properties of bridgmanite due to simultaneous substitution of Al and Fe. Elastic moduli and acoustic velocities for $(Mg_{1-x}Fe_x)(Si_{1-x}Al_x)O_3$ bridgmanite with $x = 0.10$ are shown in Fig. 6.5(b,b'). $[Fe^{3+}]_{Mg}$ has been found to be always in the high-spin (HS, S = 5/2) state in the entire lower mantle pressure range. Owing to the absence of any spin state transition in $[Fe^{3+}]_{Mg}$-$[Al^{3+}]_{Si}$ substitution, the elastic anomalies, otherwise present in the Fe^{3+}-bearing bridgmanite, would disappear in this case.

6.4 Geophysical significance

The precise understanding of the effect of iron and aluminum substitution on the elastic properties of bridgmanite is essential to unravel the composition, thermal structure, and dynamics of the Earth's lower mantle. Table 6.1 compares calculated volume, elastic moduli (bulk modulus, K, and shear modulus, G), their pressure derivatives (K′, G′), and acoustic velocities (V_P, V_S, and V_Φ) at ambient pressure and temperature conditions for the most relevant substitutions. The inclusion of 12.5 mol% of Al_2O_3 in the bridgmanite as the charge-coupled substitution $[Al^{3+}]_{Mg}$-$[Al^{3+}]_{Si}$ increases the calculated volume by ∼0.5% and decreases the value of K and G by ∼1.2% and ∼3.5%,

respectively. This trend become even more noticeable when the same amount (12.5 mol%) of Fe_2O_3 is substituted as $[Fe^{3+}]_{Mg}$-$[Fe^{3+}]_{Si}$, which results in ∼3% increase of volume, and ∼5% and ∼15% decrease of K and G, respectively. It is important to note that the effect of Fe_2O_3 substitution is different from that of the FeO one. As seen in Table 6.1, the presence of 12.5 mol% of FeO increases the value of K by ∼0.5%, while the same amount of Fe_2O_3 decreases it by ∼5%. Simultaneous substitution of Fe_2O_3 and Al_2O_3 as $[Fe^{3+}]_{Mg}$-$[Al^{3+}]_{Si}$ increases the volume by ∼1.3% and decreases K and G by ∼2.5% and ∼7%, respectively. These changes in volume and elastic moduli due to Al and Fe substitutions are also reflected in calculated acoustic velocities. The incorporation of Al_2O_3 (x = 0.125) in bridgmanite, decreases V_P, V_S, and V_Φ by ∼0.9%, ∼1.6%, and ∼0.3%, respectively, while of Fe_2O_3 decreases these values by ∼6.9%, ∼9.7%, and ∼4.4%, respectively. For simultaneous substitution of Al_2O_3 and Fe_2O_3, the decrease in V_P, V_S, and V_Φ is ∼3.5%, ∼4.8%, and ∼2.3%, respectively.

Table 6.2: Calculated values of temperature derivatives of aggregate elastic moduli $\left(\frac{dK(P,T)}{dT}, \frac{dG(P,T)}{dT}\right)$ in unit of GPa/K at 300 K and at 0 GPa, 60 GPa, and 120 GPa.

	$\frac{dK(0,300)}{dT}$	$\frac{dK(60,300)}{dT}$	$\frac{dK(120,300)}{dT}$	$\frac{dG(0,300)}{dT}$	$\frac{dG(60,300)}{dT}$	$\frac{dG(120,300)}{dT}$
$MgSiO_3$	-0.0157	-0.0093	-0.0054	-0.0178	-0.0108	-0.0077
$(Mg_{0.875}Fe^{2+}_{0.125})SiO_3$	-0.0160	-0.0097	-0.0059	-0.0178	-0.0107	-0.0077
$(Mg_{0.875}Al^{3+}_{0.125})(Si_{0.875}Al^{3+}_{0.125})O_3$	-0.0116	-0.0095	-0.0086	-0.0144	-0.0109	-0.0095
$(Mg_{0.875}Fe^{3+}_{0.125})(Si_{0.875}Fe^{3+}_{0.125})O_3$	-0.0191	-0.0088	-0.0001	-0.0205	-0.0101	-0.0066
$(Mg_{0.875}Fe^{3+}_{0.125})(Si_{0.875}Al^{3+}_{0.125})O_3$	-0.0165	-0.0097	-0.0054	-0.0182	-0.0106	-0.0074

The temperature derivatives of elastic moduli for various Fe and Al substitutions at 300 K and at 0 GPa, 60 GPa, and 120 GPa are compared in Table 6.2. The calculated values of $\frac{dK}{dT}$ and $\frac{dG}{dT}$ for pure, Fe^{2+}-, and $[Fe^{3+}]_{Mg}$-$[Al^{3+}]_{Si}$-bearing bridgmanite are very similar. This observation suggests that the aluminum present in the lower mantle may be accommodated with equal amount of ferric iron (without affecting temperature dependence significantly), and the remaining iron may be present as ferrous iron.

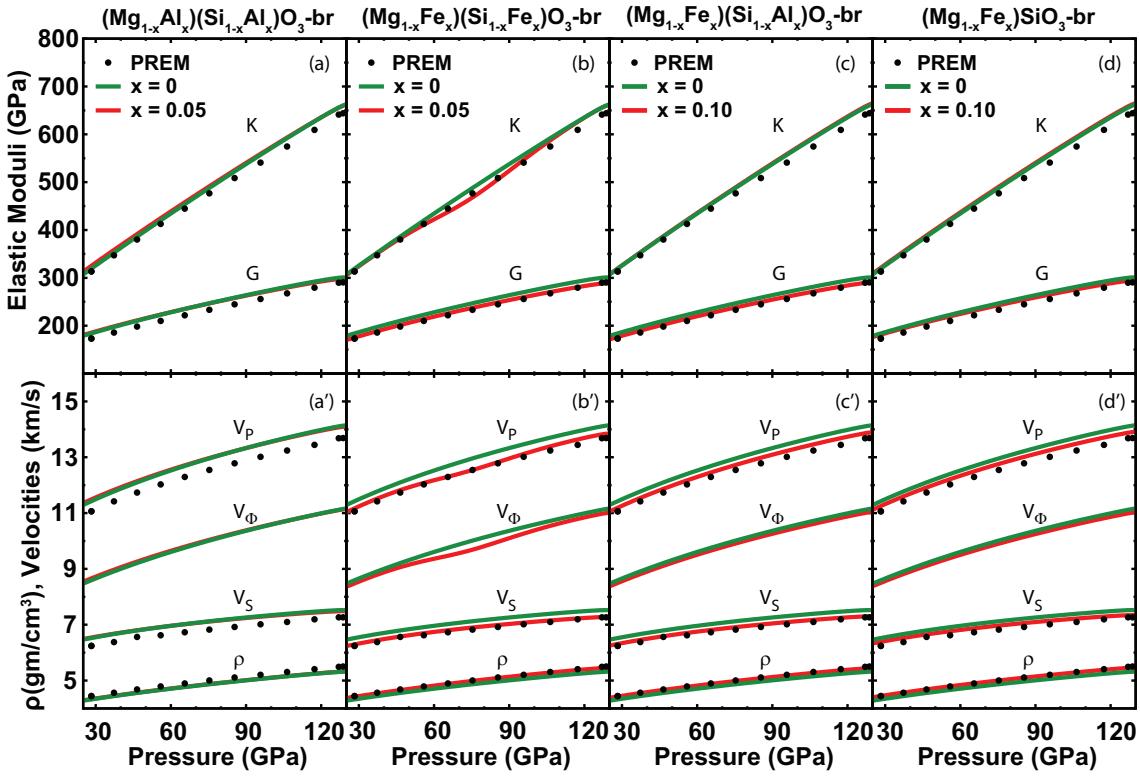

Figure 6.6: Elastic moduli, acoustic velocities, and density along the lower mantle model geotherm by *Boehler, 2000* [6] for (a,a') $[Al^{3+}]_{Mg}$-$[Al^{3+}]_{Si}$, (b,b') $[Fe^{3+}]_{Mg}$-$[Fe^{3+}]_{Si}$, (c,c') $[Fe^{3+}]_{Mg}$-$[Al^{3+}]_{Si}$, and $[Fe^{2+}]_{Mg}$ substitution in $MgSiO_3$ bridgmanite. The calculated results (red lines) are compared with that of pure $MgSiO_3$ bridgmanite (green lines) and with the Preliminary Reference Earth Model (PREM) [1] data (black points).

Elastic moduli, acoustic velocities, and density interpolated along the lower mantle model geotherm [6] for $(Mg_{0.95}Al^{3+}_{0.05})(Si_{0.95}Al^{3+}_{0.05})O_3$, $(Mg_{0.95}Fe^{3+}_{0.05})(Si_{0.95}Fe^{3+}_{0.05})O_3$, $(Mg_{0.90}Fe^{3+}_{0.10})(Si_{0.90}Al^{3+}_{0.10})O_3$, and $(Mg_{0.90}Fe^{2+}_{0.10})SiO_3$ bridgmanite are shown in Fig. 6.6. The concentration of Al and Fe in these configurations is chosen appropriately to represent the expected lower mantle composition. The calculated results are also compared with that of pure $MgSiO_3$ bridgmanite and with the Preliminary Reference Earth Model (PREM) [1]. The inclusion of Al_2O_3 does not seem to affect the elastic properties of bridgmanite significantly. The signature of anomalous softening due to HS to LS transition of $[Fe^{3+}]_{Si}$ is present in $[Fe^{3+}]_{Mg}$-$[Fe^{3+}]_{Si}$ substitution (Fig. 6.6 b,b'). However, these anomalies no longer exist with the simultaneous inclusion of Al and Fe as in $[Fe^{3+}]_{Mg}$-$[Al^{3+}]_{Si}$ substitution and overall agreement with the PREM data is quite good except for the bulk modulus, K, and compressional velocity, V_P. Relatively larger values of K and V_P compare to PREM values indicate that the lower mantle may also accommodate a reasonable amount of ferropericlase, (MgFe)O, and $CaSiO_3$ perovskite. The presence of elastic anomalies due to HS to LS transition in Fe^{3+}-bearing bridgmanite and their disappearance with the inclusion of Al_2O_3 may play an important role in deciphering the source of lateral velocity heterogeneities in the lower mantle. The elastic features of $(Mg_{0.90}Fe^{3+}_{0.10})(Si_{0.90}Al^{3+}_{0.10})O_3$ are very similar to those of $(Mg_{0.90}Fe^{2+}_{0.10})SiO_3$ bridgmanite. This again suggest that the aluminum present in the lower mantle may be accommodated as a charge-coupled substitution with equal amount of ferric iron while the remaining iron may exist as ferrous iron.

6.5 Conclusions

We have presented first-principles calculations of thermoelastic properties Al^{3+}- and Fe^{3+}-bearing bridgmanite. Aggregate elastic moduli, acoustic velocities, and density for

three charge-coupled substitutions, $[Al^{3+}]_{Mg}$-$[Al^{3+}]_{Si}$, $[Fe^{3+}]_{Mg}$-$[Fe^{3+}]_{Si}$, and $[Fe^{3+}]_{Mg}$-$[Al^{3+}]_{Si}$ at pressure and temperature conditions typical of the Earth's lower mantle have been computed by combining the vibrational density of states and static LDA/LDA+U_{sc} calculations within the quasi-harmonic approximation. Our calculated results for pure $MgSiO_3$ and Al^{3+}-bearing bridgmanite compare very with the available experimental measurements [65, 69, 111, 135, 136]. Elastic anomalies due to the HS to LS transition of $[Fe^{3+}]_{Si}$ in Fe^{3+}-bearing bridgmanite cease to exist with the presence of Al_2O_3 and this effect may have a noticeable impact on the lower mantle properties, especially the lateral velocity heterogeneities. Elastic properties calculated along the lower mantle model geotherm [6] suggest that Al_2O_3 may be accommodated with Fe_2O_3 in a charge-coupled substitution without altering the overall elastic features of $(Mg,Fe^{2+})SiO_3$ bridgmanite.

Chapter 7

Conclusions

Influence of aluminum (Al) and iron (Fe) substitutions on thermal and elastic properties of $MgSiO_3$ perovskite (also known as bridgmanite) has been investigated using quantum mechanical first-principles calculations. State-of-the art computational techniques of condensed matter physics, such as density functional theory (DFT) and density functional perturbation theory (DFPT), have been employed to advance the understanding of the thermoelastic properties of Al- and Fe-bearing bridgmanite under extreme pressure and temperature conditions. The observations for pure (Mg-br) and Al-bearing bridgmanite (Al-br) find good agreement with available experimental measurements. In particular, agreement in calculated shear velocities at 2700 K with experimental measurements by *Murakami et al., 2012* [136] shows the robust predictive power of our first-principles calculations at very hight temperature typical of the Earth's interior. In the case of Fe-br, pressure induced iron state changes and their consequences to elastic properties have been studied in detail. The existence of elastic anomalies due to iron spin state transition and their disappearance with Al_2O_3 inclusion may play an important role in deciphering the source of lateral velocity heterogeneities in the Earth's lower mantle.

References

[1] Dziewonski, A. M., and D. L. Anderson (1981), Preliminary reference Earth model, *Phys. Earth Planet. Int.*, *25*, 297–356.

[2] Bovolo, C. I., (2005), The physical and chemical composition of the lower mantle, *Phil. Trans. R. Soc. A*, *363*, 2811–2836

[3] Lin, J. F., S. Speziale, Z. Mao, and H. Marquardt (2013), Effects of the electronic spin transitions of iron in lower-mantle minerals: implications to deep-mantle geophysics and geochemistry, *Rev. Geophys.*, *51*, 244–275.

[4] Brown, J.M., and T. J. Shankland, (1981), Thermodynamic parameters in the Earth as determined from seismic profiles. *Geophys. J. R. Astron. Soc.*, *66*, 579–596.

[5] Anderson, O.L., (1982), The Earth's core and the phase diagram of iron. *Phil. Trans. R. Soc. A*, *306*, 21–35.

[6] Boehler, R. (2000), High-pressure experiments and the phase diagram of lower mantle and core materials, *Rev. Geophys.*, *38(2)*, 221–245.

[7] Houser, C., G. Masters, M. P. Flanagan, and P. M. Shearer (2008), Determination and analysis of long-wavelength transition zone structure using SS precursors. textitGeophys. J. Int., *174*, 178–194

[8] Giannozzi et al., (2009), Quantum ESPRESSO: a modular and open-source software project for quantum simulations of materials, *J. Phys.: Condens. Matter*, *21*, 395502, http://www.quantum-espresso.org

[9] Cococcioni, M. (2002), A LDA+U study of selected iron compounds, *Ph.D. Thesis*, SISSA–Scuola Internazionale Superiore di Studi Avanzati and INFM-DEMOCRITOS National Simulation Center, Trieste, Italy.

[10] Cococcioni, M., and S. de Gironcoli (2005), Linear response approach to the calculation of the effective interaction parameters in the LDA+U method, *Phys. Rev. B*, *71*, 035105.

[11] Kulik, H., M. Cococcioni, D. A. Scherlis, and N. Marzari (2006), Density functional theory in transition metal chemistry: a self-consistent Hubbard U approach, *Phys. Rev. Lett.*, *97*, 103001.

[12] Himmetoglu, B., A. Floris, S. de Gironcoli, and M. Cococcioni (2014), Hubbard-Corrected DFT Energy Functionals: The LDA+U Description of Correlated Systems, *Int. J. Quantum Chem*, *114*, 14–49.

[13] Wentzcovitch, R. M., (1991), Invariant molecular dynamics approach to structural phase transitions, *Phys. Rev. B*, *44*, 2358-2361.

[14] Wentzcovitch, R. M., J. L. Martins, and G. D. Price (1993), Ab initio molecular dynamics with variable cell shape: application to $MgSiO_3$, *Phys. Rev. Lett.*, *70*, 3947.

[15] Hohenberg, P., and W. Kohn (1964), Inhomogeneous Electron Gas, *Phys. Rev.*, *136*, B864871.

[16] Kohn, W., and L. J. Sham (1964), SelfConsistent equations including exchange and correlation effects, *Phys. Rev. A*, *140*, 1133–1138.

[17] Martin, R. M., (2004), Electronic Structure: Basic Theory and Practical Methods, *Cambridge University Press*.

[18] Ceperley, D. M., and B. J. Alder (1980), Ground state of the electron gas by a stochastic method, *Phys. Rev. Lett.*, *45*, 566–569.

[19] Perdew, J. P., K. Burke, and M. Ernzerhof (1996), Generalized Gradient Approximation Made Simple, *Phys. Rev. Lett.*, *77*, 3865.

[20] Monkhorst, H. J., and J. D. Pack (1976), Special points for Brillouin-zone integrations, *Phys. Rev. B*, *13*, 13, 5188.

[21] Phillips, J. C. (1958), Energy-band interpolation scheme based on a pseudopotential, *Phys. Rev.*, *112 (3)* 685

[22] Phillips, J. C. and L. Kleinman (1959), New method for calculating wave functions in crystals and molecules. *Phys. Rev.*, *116 (2)*, 287.

[23] Keine, V. (1970), The Pseudopotential Concept of Solid State Physics, *Academic Press, New York*.

[24] Ihm, J. (1988), Total energy calculations in solid-state physics, *Rep. Prog. Phys.*, *51*, 105.

[25] Pickett, W. E. (1989), Pseudopotential methods in condensed matter applications, *Comp.Phys. Rep.*, *9*, 115.

[26] Hamann, D. R., M. Schluter, and C. Chiang (1979) Norm-Conserving Pseudopotentials, *Phys. Rev. Lett.*, *43*, 1494.

[27] Troullier, N. and J. L. Martins (1991), Efficient pseudopotentials for plane-wave calculations, *Phys. Rev. B*, *43*, 1993.

[28] Vanderbilt, D., (1990), Soft self-consitent pseudopotentials in a genrelized eigenvalue formalism, *Phys. Rev. B*, *41*, 7892–7895.

[29] Laasonen, K., A. Pasquarello, R. Car, C. Lee, and D. Vanderbilt (1993), Car-Parrinello molecular dynamics with Vanderbilt ultrasoft pseudopotentials, *Phys. Rev. B*, *47*, 10142.

[30] Anisimov, V. I., J. Zaanen, and O. K. Andersen (1991), Band theory and Mott insulators - Hubbard-U instead of Stoner-I, *Phys. Rev. B*, *44*, 943–954.

[31] Anisimov, V. I., I. V. Solovyev, M. A. Korotin, M. T. Czyzyk, and G. A. Sawatzky (1993), Density functional theory and NiO photoemission spectra, *Phys. Rev. B*, *48*, 16929–16934.

[32] Anisimov, V. I., F. Aryasetiawan, and A. I. Lichtenstein (1997), First-principles calculations of the electronic structure and spectra of strongly correlated systems: The LDA+U method, *Phys. Rev. B*, *9*, 767–808.

[33] Hubbard, J. (1963), Electron Correlations in Narrow Energy Bands, *Proc. R. Soc. London A*, *276*, 238.

[34] Hubbard, J. (1964), Electron Correlations in Narrow Energy Bands. II. The Degenerate Band Case, *Proc. R. Soc. London A*, *277*, 237.

[35] Hubbard, J. (1964), Electron Correlations in Narrow Energy Bands. III. An Improved Solution, *Proc. R. Soc. London A*, *281*, 401.

[36] Hubbard, J. (1965), Electron Correlations in Narrow Energy Bands. IV. The Atomic Representation, *Proc. R. Soc. London A*, *285*, 542.

[37] Hubbard, J. (1967), Electron Correlations in Narrow Energy Bands. V. A Perturbation Expansion About the Atomic Limit, *Proc. R. Soc. London A*, *296*, 82.

[38] Hubbard, J. (1967), Electron Correlations in Narrow Energy Bands. VI. The Connexion with Many-Body Perturbation Theory, *Proc. R. Soc. London A*, *296*, 100.

[39] Perdew, J. P., R. G. Parr, M. Levy, and J. L. Balduz, Jr. (1982), Density-Functional Theory for Fractional Particle Number: Derivative Discontinuities of the Energy, *Phys. Rev. Lett.*, *49*, 1691.

[40] Dudarev, S. L., G. A. Botton, S. Y. Savrasov, C. J. Humphreys, and A. P. Sutton (1998), Electron-energy-loss spectra and the structural stability of nickel oxide:An LSDA+U study, *Phys. Rev. B*, *57*, 1505.

[41] Nielsen, O. H., and R. M. Martin (1985), Quantum-mechanical theory of stress and force, *Phys. Rev. B*, *32*, 3780.

[42] Parrinello, M., and A. Rahman (1981), Polymorphic transitions in single crystals: A new molecular dynamics method, *J. App. Phys.*, *52*, 7182–7190.

[43] Parrinello, M., and A. Rahman (1982), Strain fluctuations and elastic constants, *J. Chem. Phys.*, *76*, 2662–2666.

[44] Poirier, J. P. (2000), Introduction to the Physics of the Earth's Interior, *Cambridge University Press, UK.*

[45] Watt, J. P., Hashin-Shtrikman bounds on the effective elastic moduli of polycrystals with orthorhombic symmetry, *J. App. Phys.*, *50*, 6290–6295.

[46] De Cicco, P. D., and F. A. Johnson (1969), The Quantum Theory of Lattice Dynamics. IV, *Proc. R. Soc. London, A*, *310*, 11-119.

[47] Pcik, R., M. H. Cohen, and R. M. Martin (1970), Microscopic theory of force constants in the adiabatic approximation, *Phys. Rev. B*, *1*, 910.

[48] Karki, B. B., R. M. Wentzcovitch, S. de Gironcoli, and S. Baroni (1999), First principles determination elastic anisotropy and wave velocities of MgO at lower mantle conditions, *Science*, *286*, 1705.

[49] Karki, B. B., R. M. Wentzcovitch. S. de Gironcoli, and S. Baroni (2000), *Ab initio* lattice dynamics of $MgSiO_3$-perovskite, *Phys. Rev. B*, *62*, 14750.

[50] Wentzcovitch, R. M., B. B. Karki, M. Cococcioni, and S. de Gironcoli (2004), Thermoelastic properties of of $MgSiO_3$-perovskite: insights on the nature of the Earths lower mantle, *Phys. Rev. Lett.*, *92*, 018501.

[51] Wu, Z., and R. M. Wentzcovitch (2011), Quasiharmonic thermal elasticity of crystals: An analytical approach, *Phys. Rev. B*, *83*, 184115.

[52] Badro J., G. Fiquet, F. Guyot, J. P. Rueff, V. V. Struzhkin, G. Vank, and G. Monaco (2003), Iron Partitioning in Earth's Mantle: Toward a Deep Lower Mantle Discontinuity, *Science*, *300*, 789-791.

[53] Crowhurst, J. C., J. M. Brown, A. F. Goncharov, and S. D. Jacobsen (2008), Elasticity of (Mg,Fe)O through the spin transition of iron in the lower mantle, *Science*, *319*, 451–453.

[54] Tsuchiya, T., J. Tsuchiya, K. Umemoto, and R. M. Wentzcovitch (2004), Phase transition in $MgSiO_3$ perovskite in the earth's lower mantle, *Earth Planet. Sci. Lett.*, *224*, 241-248.

[55] Tsuchiya, T., R. M. Wentzcovitch, C. R. S. da Silva, S. de Gironcoli (2006), Spin transition in magnesiowstite in Earth's lower mantle, *Phys. Rev. Lett.*, *96(19)*, 198501.

[56] Marquardt M., S. Speziale, H. J. Reichmann, D. J. Frost, F. R. Schilling, and E. J. Garnero (2009), Elastic Shear Anisotropy of Ferropericlase in Earth's Lower Mantle, *Science*, *324*, 224–226.

[57] Wu, Z., J. F. Justo, C. R. S. da Silva, S. de Gironcoli, and R. M. Wentzcovitch (2009), Anomalous thermodynamic properties in ferropericlase throughout its spin crossover, *Phys. Rev. B*, *80*, 014409.

[58] Antonangeli, D., J. Siebert, C. M. Aracne, D. L. Farber, A. Bosak, M. Hoesch, M. Krisch, F. J. Ryerson, G. Fiquet, and J. Badro (2011), Spin Crossover in Ferropericlase at High Pressure: A Seismologically Transparent Transition?, *Science*, *331*, 64-67.

[59] Wu, Z., J. F. Justo, and R. M. Wentzcovitch (2013), Elastic Anomalies in a Spin-Crossover System: Ferropericlase at Lower Mantle Conditions, *Phys. Rev. Lett.*, *110*, 228501.

[60] Hsu, H., and R. M. Wentzcovitch (2014), First-principles study of intermediate-spin ferrous iron in the Earth's lower mantle, *Phys. Rev. B*, *90(19)*, 195205.

[61] Wu, Z., and R. M. Wentzcovitch (2014), Spin crossover in ferropericlase and velocity heterogeneities in the lower mantle, *Proc. Natl. Acad. Sci.*, *111(29)*, 10468–10472.

[62] Goncharov, A. F., V. V. Struzhkin, and S. D. Jacobsen (2006), Reduced Radiative Conductivity of Low-Spin (Mg,Fe)O in the Lower Mantle, *Science*, *312*, 1205–1208.

[63] Badro J., J. P. Rueff, G. Vanko, G. Monaco, G. Fiquet, and F. Guyot (2004), Electronic Transitions in Perovskite: Possible Nonconvecting Layers in the Lower Mantle, *Science*, *305*, 383.

[64] Li, J., V. V. Struzhkin, H. K. Mao, J. Shu, R. J. Hemley, Y. Fei, B. Mysen, P. Dera, V. Prakapenka, and G. Shen (2004), Electronic spin state of iron in lower mantle perovskite, *Proc. Natl. Acad. Sci.*, *101*, 14027–14030.

[65] Li, B., and J. Zhang, (2005), Pressure and temperature dependence of elastic wave velocity of MgSiO3 perovskite and the composition of the lower mantle, *Phys. Earth Planet. Inter.*, *151*, 143–154.

[66] Li, J., W. Sturhahn, J. M. Jackson, V. V. Struzhkin, J. F. Lin, J. Zhao, H. K. Mao, and G. Shen (2006), Pressure effect on the electronic structure of iron in (Mg,Fe)(Si,Al)O_3 perovskite: A combined synchrotron Mssbauer and X-ray emission spectroscopy study up to 100 GPa, *Phys. Chem. Minerals*, *33*, 575–585.

[67] Jackson, J. M., J. Zhang, and J. D. Bass (2004), Sound velocities and elasticiy of al uminous $MgSiO_3$ pervoskite: Implications for aluminum heterogeneity in Earth's lower mantel, *Geophys. Res. Lett.*, *31*, L10614.

[68] Jackson, J.M., W. Sturhahn, G. Shen, J. Zhao, M. Y. Hu, D. Errandonea, J. D. Bass, and Y. Fei (2005a), A synchrotron Mssbauer spectroscopy study of (Mg,Fe)SiO_3 perovskite up to 120 GPa, *Am. Mineral.*, *90*, 199–205.

[69] Jackson, J. M., J. Zhang, Shu, S. V. Sinogeikin, and J. D. Bass (2005b), High-pressure sound velocities and elasticity of aluminous $MgSiO_3$ perovskite to 45 GPa: Implications for lateral heterogeneity in Earths lower mantle, *Geophys. Res. Lett.*, *32*, L21305.

[70] Stackhouse, S., J. P. Brodholt, and G. D. Price (2007), Electronic spin transitions in iron-bearing $MgSiO_3$ perovskite, *Earth Planet. Sci. Lett.*, *253*, 282–290.

[71] Lin, J., H. Watson, G. Vanko, E. E. Alp, V. B. Prakapenka, P. Dera, V. V. Struzhkin, A. Kubo, J. Zhao, C. McCammon, and W. J. Evans (2008),

Intermediate-spin ferrous iron in lowermost mantle post-perovskite and perovskite, *Natl. Geosci*, *1*, 688–691.

[72] Bengtson, A., J. Li, and D. Morgan (2009), Mössbauer modeling to interpret the spin sate of iron in (Mg,Fe)SiO_3, *Geophys. Res. Lett.*, *36*, L15301.

[73] Dubrovinsky, L., T. Boffa-Ballaran , K. Glazyrin , A. Kurnosov , D. Frost , M. Merlini , M. Hanfland , V.B. Prakapenka , P. Schouwink , T. Pippinger, and N. Dubrovinskaia (2010), Single-crystal X-ray diffraction at megabar pressures and temperatures of thousands of degrees, *High Pressure Research*, *30(4)*, 620–633.

[74] Hsu, H., K. Umemoto, R. M. Wentzcovitch, and P. Blaha (2010), Spin states and hyperfine interactions of iron in (Mg,Fe)SiO_3 perovskite under pressure, *Earth Planet. Sci. Lett.*, *294*.

[75] Hsu, H., P. Blaha, M. Cococcioni, and R. M. Wentzcovitch (2011), Spin-state crossover and hyperfine interactions of ferric iron in $MgSiO_3$ perovskite, *Phys. Rev. Lett.*, *106*, 118501.

[76] Lin, J. F., E. E. Alp, Z. Mao, T. Inoue, C. McCammon, Y. Xiao, P. Chow, and J. Zhao (2012), Electronic spin and valence states of iron in the lower-mantle silicate perovskite by synchrotron Mssbauer spectroscopy, *American Mineralogist*, *97*, 592–597.

[77] McCammon, C., I. Kantor, O. Narygina, J. Rouquette, U. Ponkratz, I. Sergueev, M. Mezouar, V. Prakapenka, and L. Dubrovinsky (2008), Stable intermediate-spin ferrous iron in lower-mantle perovskite, *Nat. Geosci.*, *1*, 684–687.

[78] McCammon, C., L. Dubrovinsky, O. Narygina, I. Kantor, X. Wu, K. Glazyrin, I. Sergueev, and A. I Chumakov (2010), Low-spin Fe^{2+} in silicate perovskite and

a possible layer at the base of the lower mantle, *Phys. Earth Planet. Inter.*, *180*, 215–221.

[79] Shukla, G., Z. Wu, H. Hsu, A. Floris, M. Cococcioni, and R. M. Wentzcovitch (2015), Thermoelasticity of Fe^{2+}-bearing bridgmanite, *Geophys. Res. Lett.*, *42*, 1741-1749.

[80] Shukla, G., M. M. Topsakal, and R. Wentzcovitch (2015), Spin crossovers in iron-bearing $MgSiO_3$: their influence on the post-perovskite transition, *Phys. Earth and plane. Inter.*, *249*, 11–17.

[81] Catalli, K., S.-H. Shim, V. B. Prakapenka, J. Zhao, W. Sturhahn, P Chow, Y. Xiao, H. Liu, H. Cynn, and W.J. Evans (2010a), Spin state of ferric iron in $MgSiO_3$ perovskite and its effect on elastic properties, *Earth Planet. Sci. Lett.* , *289*, 68–75.

[82] Catalli, K., S.-H. Shim, V. B. Prakapenka, J. Zhao, and W. Sturhahn (2010b), X-ray diffraction and Moessbauer spectroscopy of Fe^{3+}-bearing Mg-silicate post-perovskite at 128–138 GPa, *American Mineralogist*, *95*, 418–421.

[83] Mao, Z., J.F. Lin, C. Jacobs, H. C. Watson, Y. Xiao, P. Chow, E. E. Alp, and V. B. Prakapenka (2010), Electronic spin and valence states of Fe in $CaIrO_3$-type silicate post-perovskite in the Earth's lowermost mantle, *Geophys. Res. Lett.*, *37*, L22304.

[84] Oganov, A.R., and S. Ono (2004), Theoretical and experimental evidence for a post-perovskite phase of $MgSiO_3$ in Earth's D“ layer, *Nature*, *430*, 445–448.

[85] Zhang, F., and A. R. Oganov (2006), Valence state and spin transitions of iron in Earth's mantle silicates, *Earth Planet. Sci. Lett.*, *249*, 436-443.

[86] Caracas, R., and R. E. Cohen (2008), Ferrous iron in post-perovskite from first-principles calculations, *Phys. Earth Planet. Inter.*, *168*, 147–152.

[87] Yu, Y. G., H. Hsu, M. Cococcioni, and R. M. Wentzcovitch (2012), Spin states and hyperfine interactions of iron incorporated in $MgSiO_3$ post-perovskite, *Earth Planet. Sci. Lett.*, *331-332*, 1-7.

[88] Hsu, H., Y. Yu, and R. M. Wentzcovitch (2012), Effects of aluminum on spin-state crossover of iron in the Earths lower mantle, *Earth Planet. Sci. Lett.*, *359-360*, 34-39.

[89] Ross, N. L., and A. Navrotsky (1988), Study of the $MgGeO_3$ Polymorphs (ortho-Pyroxene, Clinopyroxene, and Ilmenite Structures) by Calorimetry, Spectroscopy, and Phase-Equilibria, *American Mineralogist*, *73*, 1355–1365.

[90] Leinenweber, K., Y. B. Wang, T. Yagi, and H. Yusa (1994), An Unquenchable Perovskite Phase of $MgGeO_3$ and Comparison with $MgSiO_3$ Perovskite, *American Mineralogist*, *179*, 197-199.

[91] Hirose, K., K. Kawamura, Y. Ohishi, S. Tateno, N. Sata (2005), Stability and Equation of State of $MgGeO_3$ Post-Perovskite Phase, *American Mineralogist*, *90*, 262–265.

[92] Hirose, K., and R. Sinmyo (2006), Determination of post-perovskite phase transition boundary in $MgSiO_3$ using Au and MgO pressure standards, *Geophys. Res. Lett.*, *33*, L01310.

[93] Kubo, A., B. Kiefer, G. Shen, V. Prakapenka, R. Cava, and T. Duffy (2006), Stability and Equation of State of the Post-Perovskite Phase in $MgGeO_3$ to 2 Mbar, *Geophys. Res. Lett.*, *33*, L12812.

[94] Merkel, S., A. Kubo, L. Miyagi, S. Speziale, T. Duffy, H. Mao, and H. Wenk (2006), Deformation of $MgGeO_3$ post-Perovskite at Lower Mantle Pressures, *Science*, *311*, 644–646.

[95] Runge, C., A. Kubo, B. Kiefer, Y. Meng, V. Prakapenka, G. Shen, R. Cava, and T. Duffy (2006), Equation of State of $MgGeO_3$ Perovskite to 65 GPa: Comparison with the Post-Perovskite Phase, *Phys. and Chem. Minerals*, *33*, 699–709.

[96] Shim, S., A. Kubo, and T. Duffy (2007), Raman Spectroscopy of Perovskite and Post-Perovskite Phases of $MgGeO_3$ to 123 GPa, *Earth Planet. Sci. Lett.*, *260*, 166–178.

[97] Duffy, T. (2008), Some Recent Advances in Understanding the Mineralogy of Earths Deep Mantle, *Phil. Trans. Royal Soc. A*, *366*, 4273–4293.

[98] Ito, E., D. Yamazaki, T. Yoshino, H. Fukui, S. Zhai, A. Shatzkiy, T. Katsura, Y. Tange, and K. Funakoshi (2010), Pressure Generation and Investigation of the Post-Perovskite Transformation in $MgGeO_3$ by Squeezing the Kawai-Cell Equipped with Sintered Diamond Anvils, *Earth Planet. Sci. Lett.*, *293*, 84–89.

[99] Murakami, M., K. Hirose, K. Kawamura, N. Sata, Y. Ohishi (2004), Post-perovskite phase transition in $MgSiO_3$ data, *Science*, *304*, 855–858.

[100] Tsuchiya, T., and J. Tsuchiya (2007), High-Pressure-High-Temperature Phase Relations of $MgGeO_3$: First-Principles Calculations, *Phys. Rev. B*, *76*, 092105.

[101] Hummer, D. R., and Y. Fei (2012), Synthesis and crystal chemistry of Fe^{3+}-bearing $(Mg,Fe^{3+})(Si,Fe^{3+})O_3$ perovskite, *American Mineralogist*, *97*, 1915–2012.

[102] Sinmyo R., E. Bykova, C. McCammon, I. Kupenko, V. Potapkin , and L. Dubrovinsky (2014), Crystal chemistry of Fe^{2+}bearing (Mg,Fe)SiO3 perovskite: a singlecrystal Xray diffraction study, *Phys. Chem. Minerals*, *41*, 409-417.

[103] Caracas, R., and Cohen, R. E., (2005), . Effect of chemistry on the stability and elasticity of the perovskite and post-perovskite phases in the $MgSiO_3FeSiO_3Al_2O_3$ system and implications for the lowermost mantle., *Geophys. Res. Lett.*, *32*, L16310.

[104] Stackhouse, S., J. P. Brodholt, and G. D. Price (2006), Elastic anisotropy of $FeSiO_3$ end-members of the perovskite and post-perovskite phases, *Geophys. Res. Lett.*, *33*, L01304.

[105] Mao, W.L., G. Shen, V. B. Prakapenka, Y. Meng, A. J. Campbell, D. L. Heinz, J. Shu, R. J. Hemley, and H.-K. Mao (2004), Ferromagnesian postperovskite silicates in the D" layer of the earth. *Proc. Natl. Acad. Sci.*, *101(45)*, 15867–15869.

[106] Shieh, S.R., T. S. Duffy, A. Kubo, G. Shen, V. B. Prakapenka, N. Sata, K. Hirose, and Y. Ohishi (2006), Equation of state of the postperovskite phase synthesized from a natural $(Mg,Fe)SiO_3$ orthopyroxene, *Proc. Natl. Acad. Sci.*, *103(9)*, 3039-3043.

[107] Tateno, S., K. Hirose, N. Sata, and Y. Ohishi (2007), Solubility of FeO in $(Mg,Fe)SiO_3$ perovskite and the post-perovskite phase transition , *Phys. Earth. Planet. Inter.*, *160*, 319–225.

[108] Hirose, K., N. Takafuji, K. Fujino, S. R. Shieh, and T. S. Duffy (2008), Iron partitioning between perovskite and post-perovskite: A transmission electron microscope study, *American Mineralogist*, *93*, 1678–1681.

[109] Catalli, K., S.-H. Shim, and V. Prakapenka (2009), Thickness and Clapeyron slope of the post-perovskite boundary, *Nature*, *462*, 782–785.

[110] Boffa Ballaran, T., A. Kurnosov, K. Glazyrin, D. J. Frost, M. Merlini, M. Hanfland, and R. Caracas (2012), Effect of chemistry on the compressibility of silicate perovskite in the lower mantle, *Earth Planet. Sci. Lett.*, *333-334*, 181–190.

[111] Chantel, J., D. J. Frost,C. A. McCammon, Z. Jing, and Y. Wang (2012), Acoustic velocities of pure and iron-bearing magnesium silicate perovskite measured to 25 GPa and 1200 K, *Geophys. Res. Lett.*, *39*, L19307.

[112] Dorfman, S. M., Y. Meng, V. B. Prakapenka, and T. S. Duffy (2013), Effects of Fe-enrichment on the equation of state and stability of (Mg,Fe)SiO_3 perovskite, *Earth Planet. Sci. Lett.*, *361*, 249–257.

[113] Fujino, K., D. Nishio-Hamane, Y. Seto, N. Sata, T. Nagai, T. Shinme, T. Irifune, H. Ishii, N. Hiraoka, Y. Q. Cai, K. D. Tsue (2012), Spin transition of ferric iron in Al-bearing Mgperovskite up to 200 GPa and its implication for the lower mantle, *Earth Planet. Sci. Lett.*, *317-318*, 407–412.

[114] Lundin, S., L. Catalli, J. Santillan, S.-H. Shim, V. B. Prakapenka, M. Kunz, and Y. Meng (2008), Effect of Fe on the equation of state of mantle silicate perovskite over 1 Mbar, *Phys. Earth Planet. Inter.*, *168*, 97–102.

[115] Vanpeteghem, C.B., J. Zhao, R. J. Angel, N. L. Ross, and N. Bolfan-Casanova (2006), Crystal structure and equation of state of $MgSiO_3$ perovskite, *Geophys. Res. Lett.*, *33*, L03306.

[116] McCammon, C., K. Glazyrin, A. Kantor, I. Kantor, I. Kupenko, O. Narygina, V. Potapkin, C. Prescher, R. Sinmyo, A. Chumakov, R. R*ü*ffer, I. Sergueev, G. Smirnov, and L. Dubrovinsky (2013), Iron spin state in silicate perovskite at conditions of the Earth's deep interior, *High Press. Res.*, *43(3)*, 663–672.

[117] Potapkin, V, C. McCammon, K. Glazyrin, A. Kantor, I. Kupenko, C. Prescher, R. Sinmyo, G. V. Smirnov, A. I. Chumakov, R. R*ü*ffer, and L. Dubrovinsky (2013), Effect of iron oxidation state on the electrical conductivity of the Earth's lower mantle , *Nature Communication*, *4*,1427.

[118] Mao, Z., J.-F. Lin, J. Yang, T. Inoue, and V. B. Prakapenka (2015), Effects of the Fe^{3+} spin transition on the equation of state of bridgmanite, *Geophys. Res.Lett.*, *42*, 4335–4342.

[119] Tsuchiya, T., and X. Wang (2013), Ab initio investigation on the high-temperature thermodynamic properties of Fe^{3+}-bearing $MgSiO_3$ perovskite, *J. Geophys. Res. Solid Earth*, *118*, 83–91.

[120] Carrier, P., R. M. Wentzcovitch, and J. Tsuchiya (2007), First principles prediction of crystal structures at high temperatures using the quasiharmonic approximation, *Phys. Rev. B*, *76*, 064116.

[121] Baroni, S., A. Dal Corso, S. de Gironcoli, and P. Gianozzi (2001), Phonons and related crystal properties from density-functional perturbation theory, *Rev. Mod. Phys.*, *73(2)*, 515LP–565LP.

[122] Alfè, D. (2009), PHON: A program to calculate phonons using the small displacement method, *Comp. Phys. Commun.*, *180*, 26222633, doi:10.1016/j.cpc.2009.03.010.

[123] Floris, A., S. de Gironcoli, E. K. U. Gross, and M. Cococcioni (2011), Vibrational properties of MnO and NiO from DFT +U-based density functional perturbation theory, *Phys. Rev. B*, *84*, 161102(R).

[124] Xu S., S-H. Shim, and D. Morgan (2015), Origin of Fe^{3+} in Fe-containing, Al-free mantle silicate perovskite, *Earth Planet. Sci. Lett.*, *409*, 319-328.

[125] Umemoto, K., R. M. Wentzcovitch, Y. Yu, and R. Requist (2008), Spin transition in (Mg,Fe)SiO_3 perovskite under pressure, *Earth Planet. Sci. Lett.*, *276*, 198–206.

[126] Umemoto, K., R. M. Wentzcovitch, S. de Gironcoli, and S. Baroni (2010), Orderdisorder phase boundary between ice VII and VIII obtained by first principles, *Chem. Phys. Lett.*, *499*, 236–240.

[127] da Silva, P., C. R. S. da Silva and R. M. Wentzcovitch (2008), Metadata management for distributed first principles calculations in VLab - A collaborative cyberinfrastructure for materials computation, *Comp. Phys. Comm.*, *178*, 186.

[128] Wentzcovitch, R. M., J. F. Justo, Z. Wu, C. R. S da Silva, A. Yuen, and D. Kohlstedtd (2009), Anomalous compressibility of ferropericlase throughout the iron spin cross-over, *Proc. Natl. Acad. Sci.*, *106*, 21.

[129] Aizawa, Y., A. Yoneda, T. Katsura, E. Ito, T. Saito, and I. Suzuki (2004), Temperature derivatives of elastic moduli of $MgSiO_3$ pervoskite, *Geophys. Res. Lett.*, *31*, L01602.

[130] Andrault, D., N. Bolfan-Casanova, and N. Guignot (2001), Equation of state of lower mantle (Al,Fe)-$MgSiO_3$ pereovskite, *Earth planet. Sci. Lett.*, *193*, 501–508.

[131] Yeganeh-Haeri, A., (1994), Synthesis and re-investigation of the elastic properties of single-crystal magnesium silicate perovskite, *Phys. Earth Planet. Inter.* , *87*, 111–121.

[132] Sinnelnikov, Y. D., G. Chen, D. R. Neuville, M. T. Vaughan, and R. C. Liebermann (1998), Ultrasonic shear wave velocites of $MgSiO_3$ perovskite at 8 GPa and 800 K and lower mantel composition, *Science* , *281*, 667–679.

[133] Fiquet, G., A. Dewaele, D. Andrault, M. Kunz, and T. L. Bihan (2000), Thermoelastic properties and crystal structure of $MgSiO_3$ perovskite at lower mantle pressure and temperature conditions, *Geophys. Res. Lett.*, *27(1)*, 21–24.

[134] Sinogeikin, S. V., J. Zhang, and J. D. Bass (2004), Elasticity of single crystal and polycrystalline $MgSiO_3$ perovskite by Brillouin spectroscopy, *Geophys. Res. Lett.*, *31*, L06620.

[135] Murakami, M., S. V. Sinogeikin, H. Hellwig, J. D. Bass, and J. Li (2007), Sound velocity of $MgSiO_3$ perovskite to Mbar pressure, *Earth Planet. Sci. Lett.*, *256*, 47–54.

[136] Murakami, M., Y. Ohishi, N. Hirao, and K. Hirose (2012), A perovskitic lower mantle inferred from high-pressure, high-temperature sound velocity data, *Nature*, *485*, 90–94.

[137] Caracas, R., H. Ishii , M. Hiraoka, Y. Ohishi, and N. Hirao (2014), Identifying the spin transition in Fe^{2+}-rich $MgSiO_3$ perovskite from X-ray diffraction and vibrational spectroscopy, *American Mineralogist*, *99(7)*, 1270–1276.

[138] Zhang, L., Y. Meng, W. Yang, L. Wang, W. L. Mao, Q-S. Zeng, J. S. Jeong, A. J. Wagner, K. A. Mkhoyan, W. Liu, R. Xu, and H-K. Mao, (2014), Disproportionation of (Mg,Fe)SiO_3 perovskite in Earths deep lower mantle, *Science*, *344*, 877.

[139] Nunez-Valdez, M., Z. Wu, Y. G. Yu, J. Revenaugh, and R. M. Wentzcovitch (2012a), Thermoelastic properties of ringwoodite $(Fe_xMg_{1-x})_2SiO_4$: Its relationship to the 520 km seismic discontinuity, *Earth Planet. Sci. Lett.*, *351-352*, 115–122.

[140] Nunez-Valdez, M., Z. Wu, Y. G. Yu, and R. M. Wentzcovitch (2013), Thermal elasticity of $(Fe_xMg_{1-x})_2SiO_4$ olivine and wadsleyite, *Geophys. Res. Lett.*, *40*, 290–294.

[141] Zhang, Z., L. Stixrude, J. Brodholt (2013), Elastic properties of $MgSiO_3$-perovskite under lower mantle conditions and the composition of the deep Earth, *Earth. Planet. Sci. Lett.*, *379*, 1–12.

[142] Oganov, A. R., J. P. Brodholt, and G. D. Price (2001b), The elastic constants of $MgSiO_3$ perovskite at pressure and temperatures of the Earth's mantle , *Nature*, *411*, 934–9370.

[143] Marton, F. C., R. E. Cohen (2002), Constraints on lower mantle composition from molecular dynamics simulations of $MgSiO_3$ perovskite, *Phys. Earth Planet. Inter.*, *134*, 239–252.

[144] Kiefer, B., L. Stixrude, and R. M. Wentzcovitch (2002), Elasticity of (Mg,Fe)SiO_3-perovskite at lower mantle conditions, *Geophys. Res. Lett.*, *29*, 1–4.

[145] Karki, B. B., R. M. Wentzcovitch, S. de Gironcoli, and S. Baroni (2001), First principles thermoelasticity of $MgSiO_3$-perovskite:consequences for the inferred properties of the lower mantle, *Geophys. Res. Lett.*, *28*, 2699–2702.

Appendix A

Model geotherms

Temperature variation as a function of depth or pressure in the Earth's lower mantle for three different models are shown in Fig. A.1.

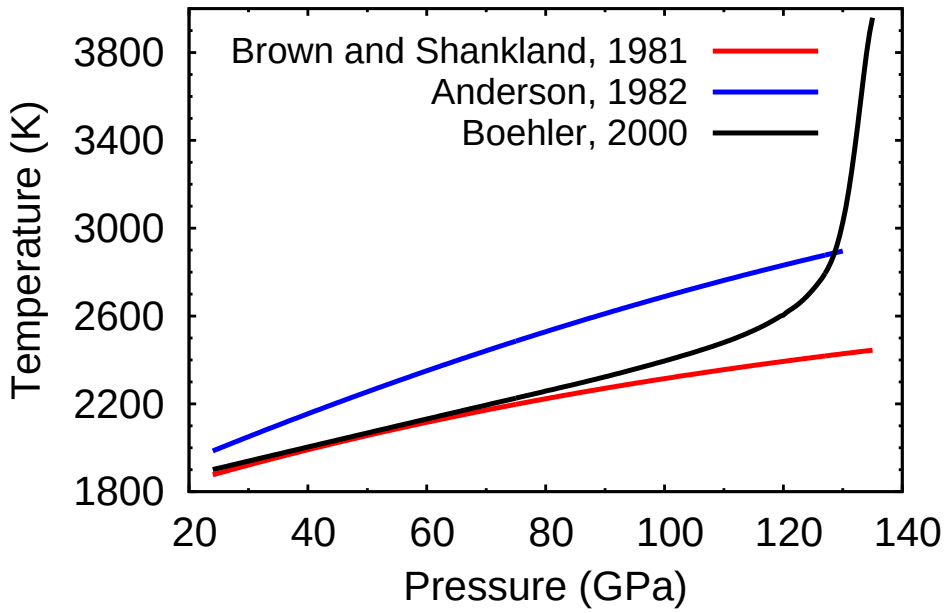

Figure A.1: Earth's lower mantle model geotherms by *Brown and Shankland, 1981*[4] (red), *Anderson, 1982*[5] (blue), and *Boehler, 2000*[6] (black).